Modelling Cell Orientation In Artificial Tissues

Thesis

Modelling cell orientation in artificial tissues

Submitted for the degree of Master of Philosophy in Biophysics

Piotr W. Mieczkowski MSc

supervised by

Dr Jim P. Hague, Dr Jane Loughlin,

Dr James Phillips, Dr Calum MacCormick

The Open University, Milton Keynes

September, 2017

Abstract

Engineered tissues have many potential applications both as experimental systems and in therapeutic devices and treatments. Specially, there is potential to repair damaged spinal cord, however work is still needed to predict the process of tissue growth. Computational physics has potential to significantly accelerate the progress of development and to improve the properties of engineered neural tissue (ENT).

Research has found that correlation exists between physical forces and the arrangement of cells in engineered tissue. In this thesis, emphasis is put on the interaction between astrocytes within engineered neural tissue (ENT). The main aim of this work is to create a computational model which will be able to predict the arrangement of these cells in ENT.

Computational techniques of soft matter physics are used to describe the final growth state of cells in ENT. In this thesis, we treat tissue as a two dimensional mesh. Interactions are described by both a simple Hamiltonian related to cell orientation and the dipole force model (DFM) and a more advanced Hamiltonian, which takes into account the influence of the extracellular matrix and cells. To find the minimum energy state of the system a simulated annealing algorithm was used.

The first set of results presents a two-dimensional map of real artificial engineered neural tissue and shows the statistical distribution of the average angles and positions of groups of cells within the tissue. Next, we present results generated by a simple Hamiltonian and more advanced model to investigate information about orientation, arrangement and shape of the whole tissue

It is found that an extended DFM where cells can move and change orientation is able to reproduce several features of the experimental data including an approximation to the delta regions and the aligned behaviour in the centre of the sample.

Contents

List of Figures

1 Introduction to the biological problem

1.1 Introduction

All organisms are made of a large number of different cells, with a variety of unique functions and characteristics. It is estimated that in the human body there are about 4×10^{13} cells [1]. Cells use sophisticated arrangements to create more complicated structures - tissues and organs. In the human body, we can distinguish four main tissues: epithelial, connective, muscular and nervous tissues [2], which between them constitute the organs required to supply all the necessary functions for life. Specific proteins are important for maintaining arrangement of cells, which can be modified during the life of the cell [2].

So far medicine is able to replace simple tissues for example to replace damaged skin with artificial skin such as Apligraf ® [3]. Unfortunately this cannot be done with more complicated tissues, especially where precise arrangement of cells is essential to provide proper functionality to the tissue. In damaged central nervous tissue, formation of glial cell scars is thought to impede the repair of damaged neurons [4]. The imprecise alignment of glial cells does not allow neuronal regrowth. An artificial tissue with an aligned arrangement of cells to conduct the neuronal growth may be the key to solving this problem. In recent years, scientists have made significant progress in engineered neural tissue, which may in the future help repair damaged spinal cord[4]. Moreover, in the far future it may be possible to create whole artificial organs which will be able to replace damaged organs [5]. Artificial tissue can be made with desired properties that can decrease the probability of rejection [6].

The main aim of this project is to develop a model to predict the orientation of cells in artificial tissues. We cooperate with a bio-engineering group lead by James Phillips at UCL as we try to advance understanding in this area.

This chapter presents an introduction to cell biology, which will help us to describe and understand the interactions of cells in the engineered neural tissue investigated in this project. During recent years, tissue engineering has become a multidisciplinary branch of science which requires an understanding of different cell types, their physical parameters and interactions between cells [4]. Groups of scientists from different disciplines have established techniques to influence cell growth and final shape, orientation and assembly of cellular structures [7]. To develop these techniques, a description of physical interactions is essential in order to allow us to understand the mechanics involved in the arrangement of cells.

The introductory part of the thesis is divided into three sections as follows: biology, physics and optimisation methods: Chapter 1 - **Introduction to the biological** problem presents the relevant cell biology background and discusses the main mechanisms affecting cell motility, such as the cytoskeleton, myosin motors and focal adhesion complex. Chapter 2 - **Introduction to theories of cell organisation** is concerned with soft condensed matter physics, which is used to describe interactions between cells. In the **Methodology and Models** (chapter 3), a new Hamiltonian is introduced and there are briefly described the most common algorithms which allow us to obtain the global minimum of the Hamiltonian. Moreover the simulation algorithm, as it was applied in the project is described in detail. Two results chapters **Experimental data and its features** and **Results from theoretical models** present and describe original results. The first results chapter focuses on quantitative description of the cell arrangement in the artificial neural tissue. Whereas the next results chapter is concerned with results from the models as obtained by the simulated annealing algorithm. The results show correlation between behaviour of cells in the artificial tissue and the model. The last chapter is connected with discussion and further work. The main advantages and disadvantages of the model are presented. Furthermore, correlation

between the artificial tissue and the model is discussed.

1.2 Tissue engineering

Throughout the lifespan of an organism, the regeneration of most cells and tissues is continuous. Cells adopt different morphologies, positions and orientations.Moreover loss of well-defined organisation leads to degeneration of tissue. Knowledge about tissues and cell organization is especially important in many aspects of medicine such as surgery, organ transplants and in aesthetic medicine. With progress in medicine and engineering, a branch of science known as tissue engineering emerged. Tissue engineering is the study of the interaction between cells, combining engineering techniques and biological knowledge to develop artificial tissues.

Tissue engineering is a promising field of science for improving treatment of scars after burn injuries, replacement of heart valves, blood vessels, ligaments and tendons, healing of fractured bones and repair of spinal cord injury. In the future, there are likely many more possible, advanced applications like the transplantation of whole engineered organs [4].

The earliest skin grafts were carried out about 5000 years ago in ancient India[8]. Since then surgeons have made significant progress. Nowadays methods of skin grafting are common, but some patients with wound healing problems require an artificial skin immediately. Often, the first few hours following an accident are pivotal to rescuing the patient, therefore fast application of skin substitute is essential. There are already some products available for commercial use, like Apligraf® [3], which is a bi-layered skin replacement for patients with venous leg and diabetic foot ulcers [3]. As artificial tissues become commonly available it will be possible to create banks of engineered skin for use when needed [6].

Another tissue with a well established regeneration process is bone tissue, which

can regenerate at sites of injury. Bone is the only human tissue that does not form scars because the regeneration process is able to form part of the new bone rather than repair the old tissue [9] . The main limitation of bone reconstruction is the size of the injury, as an organism is not always able to supply a sufficient amount of oxygen and nutrients for full recovery of the fractured bone. To solve this problem, surgeons can use prostheses or grafts to support regeneration of the tissue [10] . Engineers are attempting to improve these techniques and create bones with the desired properties such as durability and response to mechanical stress [10].

Nerve repair is a major challenge for tissue engineers, as the nervous system has a very limited natural regeneration process. The main problems relate to the guidance of axons, controlling the speed of axonal growth and avoiding scarring process[11]. The central nervous system (CNS) consists of the brain and the spinal cord. The remaining part of the nervous system is known as the peripheral nerve system (PNS) [12]. A detailed description of nervous tissue can be found in section 1.8. In the peripheral nerve system, when a substantial number of neurons survive after damage, it is still possible to regenerate the axons. Neurons are able to regenerate at a speed of about 1mm per day, but to support repair a scaffold is used to guide growth [11]. Tissue engineers in recent years have developed techniques for supporting growth of neurons in both PNS and CNS. For this purpose Schwann cells are a promising guide system[4].

In the wider project in the research group of James Philips at UCL, aligned engineered neural tissue (ENT) is composed of cells such as astrocytes, within an artificial scaffold, which can support axonal growth.

There are a number of different materials that can imitate natural structures, called biomimetic materials, that are used for construction of the scaffolds. In engineered tissue engineers have tried to find materials which can match the requirements of living tissues within organisms. The scaffold should readily adopt tissue properties after

transplantation and be remodelled appropriately during the repair process [4]. Furthermore it is desirable that the material is robust enough to preserve some of its mechanical properties, to keep the shape of the tissue and at the same time allow cells to grow within it [4]. The easiest way to fulfill these requirements is to use components of the extracellular matrix such as collagen, fibrin or fibronectin, thus providing a dense collagen matrix and extracellular matrix (ECM) proteins in proper proportions for any future tissue [4]. On the other hand, the host may mount an immune reaction to antigens in the ECM and eventually reject the graft [4]. An alternative promising approach uses silk as a scaffold material; this is a fibrous structural protein produced by non-mammalian animals [13]. The advantage of silk as a biomaterial is that it has a much higher tensile strength than collagen fibres, comparable with a high quality engineering steel [14]. Furthermore, in recent years, the development of genetic engineering techniques has allowed production of variations of silk for medical use. Natural silk material consists of organised fibres made of fibrin molecules and can vary depending on the animal type [13, 14]. Similar material can be produced in synthetic way, in order to allow silk to be obtained with the desired parameters for construction of a specific scaffold [13]. However, problems can occur after transplantation as a consequence of immune reactions and the influence of silk on cell adhesion and migration is still not fully known [13].

1.2.1 Scaffolds in engineered tissues

This section explains the main techniques used to create scaffolds for tissue repair. During recent years, scientists have developed a range of techniques for fabricating anisotropic engineered tissues including the use of aligned fibres channels, patterned surfaces, microcontact printing, mechanical loading and gradients of chemical cues, to create and organize tissues[7]. The main aim of most of these techniques is to create a

usable scaffold, which will permit and direct cell growth.

Biomimetic surface chemistry is a strategy used to manufacture scaffolds. There are methods which allow modification of the surface of the materials and create the substrate. The structure of the substrate help to control cells. In the literature, there are examples where proteins from the ECM are used to create two-dimensional scaffolds to stimulate and guide growing cells [15]. Because of the limitations of small contact surface interaction, more advanced techniques try to create three-dimensional scaffolds. Engineers using techniques such us the bottom up approach or self-assembly have tried to create macromolecular aggregates, nanotubes or nanoparticles [16, 17], to extend a surface of interaction within a scaffold.

The mentioned techniques can significantly influence cell differentiation and motility but there are also approaches for changing the cell orientation and the direction of the ECM, which is especially important in nerve regeneration [18, 19] . Varying the geometry of the substrate using cell patterning, allows us to control cell orientation on significant areas of engineered tissue [20]. In the literature, correlation between cell arrangements and the substrate is often called contact guidance [21]. One of the simplest ways to control growth of cells is to form a single intersection between two planes. Similarly engineers have developed more complicated systems of steps, grooves and spiral shapes for substrates. Recent development of nanotechnology and photolithography allows us to create grooves in substrates with high accuracy and with different parameters, such as the distance between grooves (as shown in figure 1) [20, 21, 22, 23, 24] .

Biomimetic scaffolds can be made of aligned collagen fibrils. There are different ways of obtaining such scaffolds; one of the main principles is application of unaxial mechanical loading or stress within the scaffold to arrange fibres [25].

The main idea behind using aligned structures is to create ‘tunnels’ or ‘tracks’,

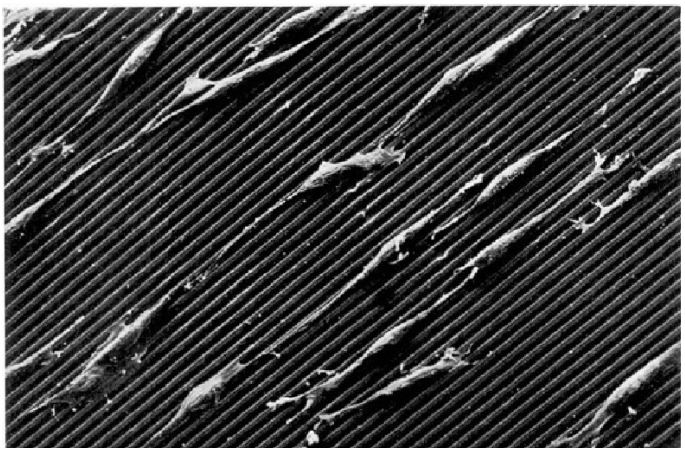

Figure 1: Scanning electron microscopy photograph (SEM) of baby hamster kidney cells aligned on repeated grooves, of period 6 μm and depth 2 μm etched into perspex [20].

which allow cells to move and grow along them. This approach is a promising method for obtaining anisotropic engineered tissues. So far, the above-mentioned methods are potential ways to obtain aligned structures but unfortunately, they are still underdeveloped for medical applications.

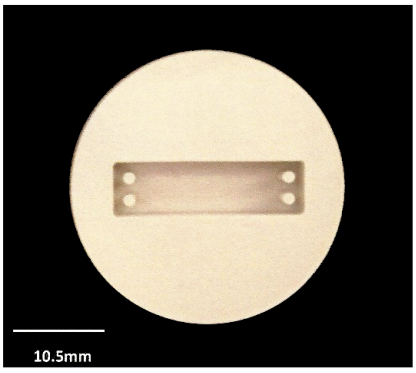

Figure 2: Three dimensional mould, prepared to seed cells within collagen matrix. The round posts serve as 'tethering points' increasing resistance of the sample to stretching forces, which occur as a results of the interaction of the cells with the matrix. Reproduced from: Ref. [7]

A group of tissue engineers at UCL and the Open University, led by James Phillips, created scaffolds, using a self - assembly technique, where distribution of tension is controlled by using tethering points in the mould (picture 2). The scaffold consists of a collagen hydrogel which is seeded with astrocytes [7]. The main purpose of this thesis is to model the interactions between cells, which are grown a mould. The model describes cell orientation and positions in engineered neural tissue.

1.3 Cell movement

In the previous section, the role of the scaffold in tissue engineering was briefly discussed. This section will cover the mechanism of cell movements within artificial tissues.

Cells have a wide range of internal cellular movements and changes in cell shape take place through the lifespan of a cell. Changes in the properties of a cell are related to its function. Many mechanisms are involved in the migration of cells from one place to another, such as remodeling of the cytoskeleton and interactions with the extracellular environment. In Nature we can observe cells that have moving parts such as flagella, which help them move through a fluid environment. Furthermore we can observe several processes by which cells move in response to a stimulus, as shown in figure 3 and described briefly below.

- Electrotaxis: electrical cues can affect cellular behaviour. In the literature we can find correlation between various regulatory mechanisms which occur under electric field stimulation and cell orientation. There are examples of electrical fields being used to direct metastatic cancer cells, neuron guidance and wound healing. [21, 26, 27]

- Gravitaxis: attractions and movement due to gravity.

- Magnetotaxis: movement of cells in response to magnetic fields [28].

- Chemotaxis: This is a process responsible for changing orientation and movement up or down a gradient of concentration of a chemical (respectively positive and negative chemotaxis). In bacteria, this process allows cells to move toward nutrients or to avoid repellents. There are other examples of chemotaxis; such as the movement of sperm towards an egg, the reorganization of cells in tissues and the reaction of immune system cells. Several mathematical models of chemotaxis have been developed [27, 29].

- Hapotaxis: Additionally in the extracellular matrix (ECM) there are often haptotacic processes. Haptotaxis is a similar process to chemotaxis, involving movement of cells along a gradient of cellular adhesion sites or a substrate-bound chemo-attractant [30].

- Durotaxis: This process is responsible for moving cells in the direction of the biggest gradient of mechanical stress. The process of durotaxis depends on the substrate or environment around the cells [27]. In other words, durotaxis can be described as the process by which cell movement is regulated by changes of substrate mechanical properties.

In Nature, the ECM has mechanical properties which include: stiffness/compliance, break-strength, elasticity/viscosity and anisotropy. These parameters influence the generation of forces between particular parts of tissue. Mechanical force can change the orientation, position and shape of cells in tissues.

According to the Newton's third law, the contraction forces, generated within the cell cytoskeleton exert an equal force on both cells and substrate. Let's consider one cell located on the substrate. When a substrate has greater stiffness and density than does a cell, it will move or deform very little compared to the cell. In other words, the more the substrate deforms, the less cells change position. Moreover the principle

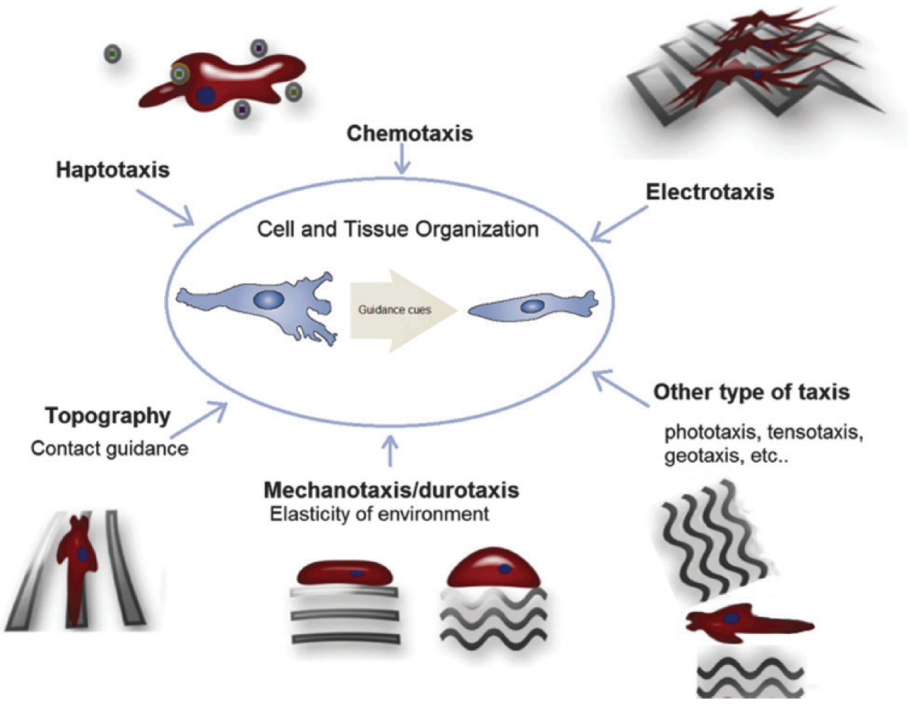

Figure 3: Directional locomotion of cells is crucial in many processes, such as immune response and wound healing. The control of cell migration can be induced by means of various taxes (movement towards away from stimulus) as schematized. Reproduced from Ref. [27].

can be applied to a whole system of cells. It follows that if cells change position to the greater extent, the substrate is very stiff and conversely if cells change position to a lesser extent, the substrate is soft. From our point of view, the most important correlation is between size of displacement of cells and the amount of strain applied to cells [31].

1.4 Structure of the cell

The biology of cells has been well-studied and the overview included in this thesis is based on 'World of the cell' by Becker et al. [2]. Cells are complex structures, which consist of nucleus, cytoplasm and cell membrane. All ingredients have their unique functions and mechanisms. The cytoplasm can be defined as the cytosol plus the components of the cytoskeleton and the organelles of the cell. The aqueous cytosol contains many different nutrients, metabolites and proteins dissolved within it. The

cytoplasm determines the position of organelles, supports transport within the cell, provides mechanical support of cells and has significant influence in the mitosis process.

Cytosol is a complex gel-like, semi-transparent liquid that surrounds the organelles. The cytoskeleton (the structure responsible for keeping or changing the shape of the cell) extends throughout the interior of the cells and is a complex structure. The cytoskeleton mainly consists of microtubules, microfilaments and intermediate filaments as shown in figure 4. To understand how the cytoskeleton is able to fulfil its functions, it is essential to describe all its components.

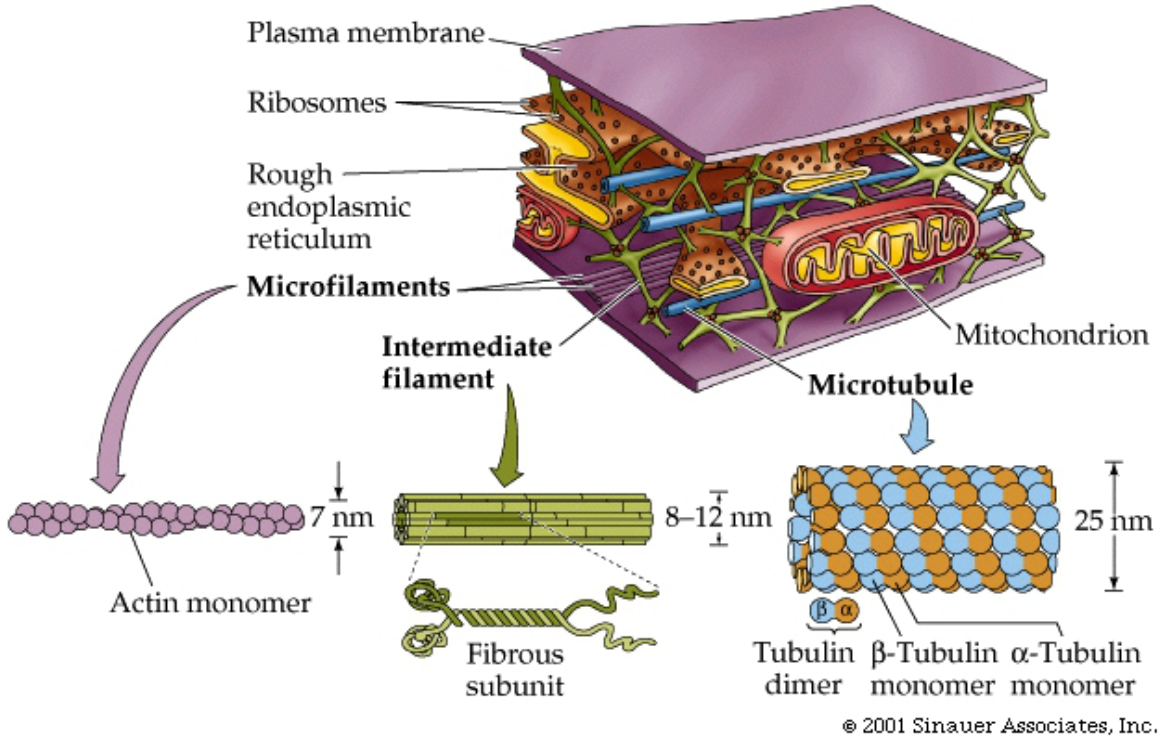

Figure 4: Schematic showing components of the cytoskeleton and organelles within a cell. The diagram shows the three characteristic components of the cytoskeleton: microfilaments, intermediate filaments and microtubules. Reproduced from: [32].

Microtubules are the component of the cytoskeleton that have the greatest diameter. These hollow tubes are responsible for the organisation and maintenance of cell shape and polarity, chromosome movements, movement of organelles, transport and cell motility. Organisation of microtubules is not random, one end is located in one of two symmetrical microtubule-organizing centers (MTOC - in most animal cells these are

called the centrosome). MTOCs are located close to the nucleus, and have a significant role during mitosis, as they initiate movement of organelles and chromosomes during the process. Basically, having one end anchored and having the capacity to grow and shrink, makes microtubules ideal for organizing and moving intracellular constituents. It is important to note that microtubules are not symmetrical and have distinct ends. Commonly one end identified as the minus (-) end, is anchored to the centrosome and the plus (+) end is connected to the cell membrane. This attribute helps navigation of the myosin motors (described in section 1.5.2). An interesting property of the MTOC is the limited number of anchoring sites for microtubules. Additionally the structure of microtubules is stabilized by microtubule associated proteins (MAPs). Each MAP anchors to microtubles at regular intervals, connecting them with other filaments and other parts of cells, such as organelles or the cell membrane.

Intracellular transport is also supported by the smallest fibril of the cytoskeleton - microfilaments, which are small linear polymers of actin that are $7nm$ in diameter. Microfilaments create the contractile fibrils of muscle cells, which are the basis of muscle contraction. In many animal cells the greatest density of microfilaments is along the plasma membrane in the cell cortex. This is the outer layer of cytoplasm, just below the cell membrane, where microfilaments create a complicated network of connected fibres. The connected fibres support and keep the membrane in the desired shape and offer resistance to external forces which can disrupt cohesion of the membrane. Whereas microfilaments in other parts of tissue form a network, they are connected by the proteins such as filamin, which is a long molecule made of two identical polypeptides with two actin 'anchors' at every site. Sometimes is is necessary to make the network soften and liquify, therefore there are proteins that have the opposite function of breaking up of the network, such as gelosin. Furthermore there are proteins which help to connect actin filaments to the cell membrane or bundle them

together to improve strength and durability of microtubles.

The third component of the cytoskeleton is the intermediate filaments which have a diameter intermediate between microtubules and microfilaments (see figure 4).

Intermediate filaments are the most stable and least soluble in water, allowing them to create durable structures. This type of structure supports the shape of the cell and has a tension bearing role during the life of the cell. In contrast to microtubules and microfilaments, intermediate filaments differ significantly between cells in terms of size and chemical properties; there is no one way to describe their structure, but most of them have one homologous central rodlike domain of a few hundred amino acids.

Examples of, stained microfilaments, intermediate filaments and microtubules are presented in Figure 5.

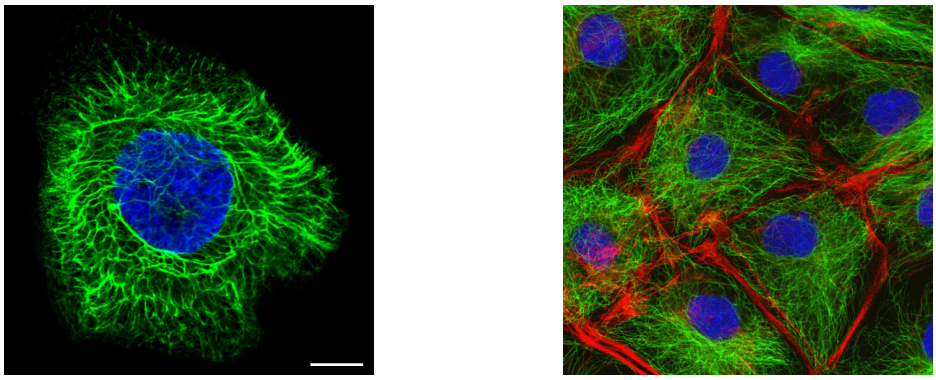

(a) Blue colour represents nucleus; green intermediate filaments. Credits : The human protein atlas Ref: [33].

(b) Blue colour presents nucleus; green micro-tubules and red actin filaments. Credits: British society for Cell Biology Ref: [34].

Figure 5: Fluorescent staining of cytoskeletal components within animal cells. Fig (5a) one cell, nucleus (blue) surrounded by intermediate filaments (green). In figure 5b, the nuclei (blue) of cells are surrounded by micro-tubules (green). Additionally, the red colour represents the cortex composed of actin between the cells.

It is worth examining how cytoskeletal components cooperate with each other and create a complex system, which delivers structure and resistance to external and internal forces. In the cytoskeleton, all components are connected by specific linker proteins, which reorganise the structure. This is a key mechanism to allow adjustment of the cell shape. The regulation process is described in more detail in the next sections.

1.5 Cytoskeleton regulation mechanism

To fully understand the regulation of actin filament fibres, it is essential to know about the mechanism responsible for movement. As we know, actin filaments create a network connected by cross-linked proteins, but living cells cannot be treated as static structures. Cross-linked connections are constantly changing during growth and reorganisation of tissues, which requires some input of energy.

1.5.1 Polymerization of the actin

This section describes changes in the length of the microfilament fibres made of actin, and is especially concerned with polymerization occurring in the cytoskeletal system. A polymer filament can extend or shorten in length through respectively polymerization and depolymerization processes. Specifically an actin protein can be added or removed to the end of the polymer chain. Actin protein is asymmetric and consist of a single polypeptide of 375 amino acids. Changing the length of filaments causes the cytoskeleton to reorganize and readjust its structure to resist external forces. Most polymerization reactions occur by self-assembly, which does not require energy sources, whereas energy input is required to extend microtubules or microfilaments. To provide energy adeonosine triphosphate (ATP) is used, which binds to monomeric actin (G actin). During the polymerization processes ATP is transformed in a chemical reaction and the energy released drives filament assembly [35].

1.5.2 Actomyosin as a source of contractility

The previous sections described the possibility of changing the cytoskeleton structure by changing the length of microfilaments. This section puts emphasis on a more dynamic mechanism which regulates motility and contractility. The most visible effects of contractility are the beating of the heart, or bending of limbs. There are also less

obvious contractile processes at the micro scale, which are more important for the purpose of this project. These complex mechanisms are also responsible for regulating the whole structure of subcellular, cellular, multicellular and tissue levels, but in this section we will mainly focus on the subcellular level. The basic components responsible for motility are motor proteins or mechanoenzymes.

In eukaryotes, one of the main motility mechanisms involves coupling between the motor proteins and microtubules and a second mechanism involves interaction between filaments and members of the myosin family of motor molecules. In the case of movement along microtubules, we can distinguish two different families of motor proteins: kinesins and dyneins. Proteins move along the cytoskeleton, but this requires constant intake of energy, which in this case is delivered by ATP. During a hydrolysis reaction energy from ATP is changed to mechanical movement of mechanoenzymes[36]. Examples of microtubule-based movement are fast axonal transport where mitochondria, lipids, synaptic vesicles, proteins and other cell components are transported within the cell. Microtubules act as 'roads' for associated motor proteins, which attach to both their 'cargo' and to the microtubule.

Another motor protein is myosin, which moves along actin filaments (picture 6). Such movement along them can change connections between micro filaments and reorganise the structure of them and generate internal forces which change the shape of cells. Furthermore myosin is responsible for muscle contraction, cell movement and vesicle transport.

Myosins, kinesins and dyneins are polypeptide chains, with one globular head group, that connects to the actin filaments or microtubules, and a tail which anchors to the organelles or other cell components ('the cargo'). As already mentioned, microtubules and microfilaments have distinct ends that are polarised, which helps motor proteins to navigate and move in the right direction. Generation of contractile forces requires

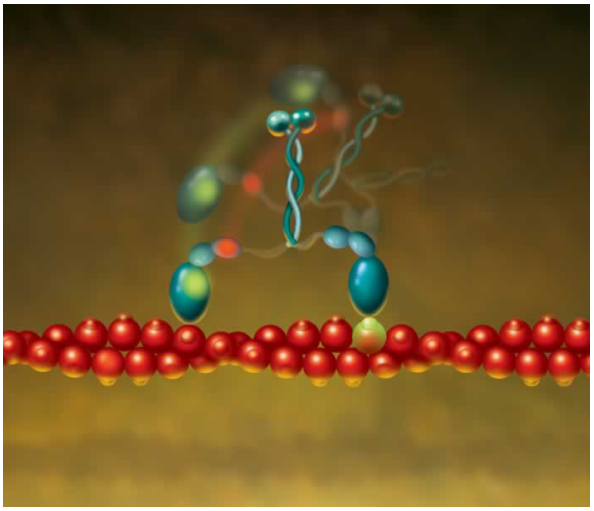

Figure 6: Representation of a myosin VI motor protein, associated with an actin filament. The heads (blue) connect to microtubules or microfilaments (as in this illustration) and the tail can be connected to an organelle or another cytoskeleton filament. The motor protein can 'walk' along the cytoskeleton and transport an organelle to a different part of the cell. Myosin can also regulate stress in the cell by connecting different microtubules and microfilaments. Credits: Paul Selvin Ref. [37].

a significant amount of energy. To achieve this, myosin often creates array structures to improve the strength of the connections. Motor proteins have a high capacity for changing the structure of the cell, allowing tension to be transferred out of the cell to the environment using focal adhesion contacts [38] which is explained in more detail in the next section.

1.6 Focal adhesion connections

So far this thesis has been mainly concerned with the mechanism of stress dissipation within a cell. However cells interact with each other, so force applied to the tissues is spread between cells. Therefore the mechanism by which cells interact with the substrate, other cells and the extracellular matrix is especially important in tissue engineering. Cells have mechanisms by which they recognise and interact with their environment and depending on the situation there are a variety of connections within tissue, eg. junctions or focal adhesions. Connections with the extracellular matrix are described in section 1.7, but here it is important to highlight the parts of cells

responsible for maintaining contact with the surrounding environment.

In the cell's plasma membrane there are specialized adhesion receptors, called adhesion molecules (see figure 7) which connect the cytoskeleton with components outside the cell. The transmembrane complex of proteins is associated with focal adhesion (shown in figure 8) and connect the microfilaments with the matter beyond the tissue.

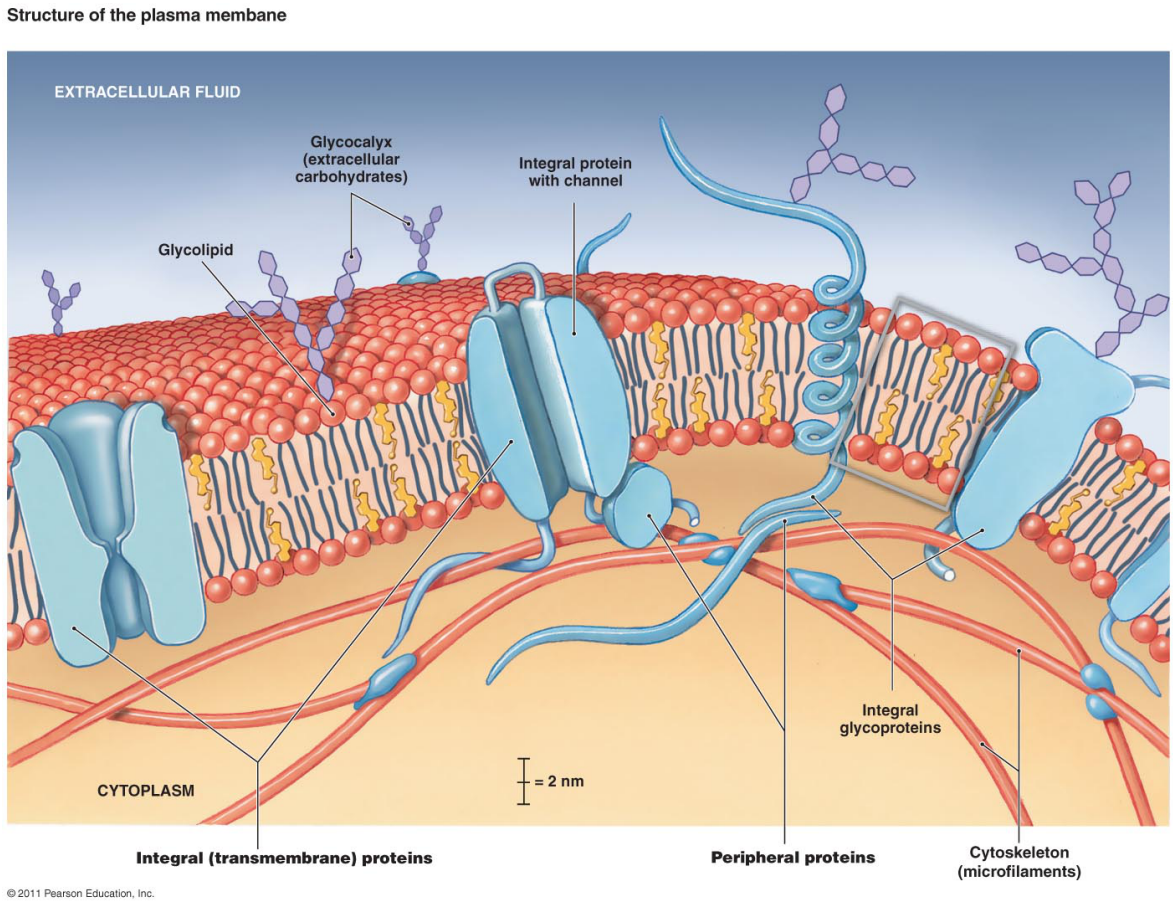

Figure 7: Integral membrane protiens and peripheral proteins connect extracellular matrix to actin filaments inside a cell. Actin filaments form a layer called the cell cortex, which helps the cell to resist external stress and contributes to the mechanical properties of the cell. Reproduced from [32].

A membrane-spanning protein crossing the plasma membrane, called integrin, creates focal adhesion connections with proteins such as talin, α-actinin, filamin, vinculin, tensin and focal adhesion kinase (figure 8). Depending on cell motility, proteins included in the focal adhesion complex can vary according to the duration of change in the structure of a tissue. An example of a focal adhesion complex is presented in figure 9, where red color indicates vinculin, part of the focal adhesion complex, and green

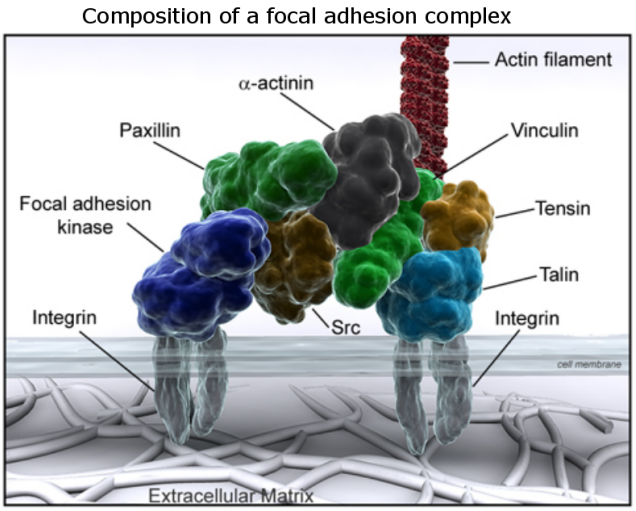

Figure 8: A number of different cellular proteins assemble to form a focal adhesion complex. Such complexes connect the cytoskeleton inside the cell to the extracellular matrix via transmembrane proteins known as integrins. The presence of fewer components allows cells to quickly detach from the ECM, this has an influence on the time taken for the cell's reorientation. Reproduced from: [39]

indicates actin fibres.

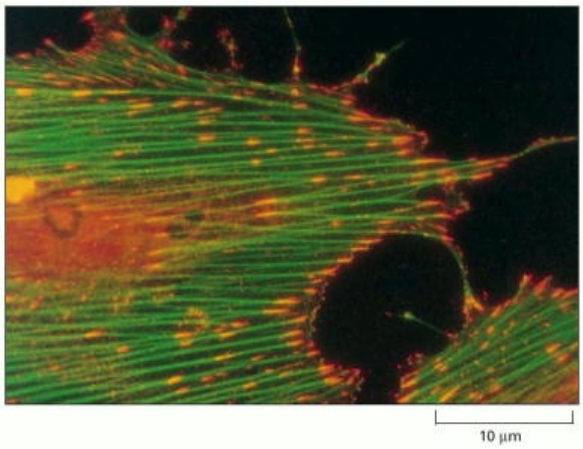

Figure 9: Red stained integrin proteins, which create focal adhesion contacts. One edge of focal adhesion contact is connected to the the actin filaments (in green) and the second to the substrate [40].

Another system of connection are junctions, used in cell-cell connections. Examples are adhesive junctions, adherens junctions, desmosomes tight junctions and gap junctions. The role of the junctions is very important in polarized epithelium, which can be described as cells connected tightly in a row. They are not described in detail, as they are beyond the scope of this thesis, which instead focuses on the structure of artificial neural tissues, where cells are loosely organized and attached to extracellular

structures and interactions between them are regulated by the collagen fibres.

1.7 Interaction of cells with the extracellular matrix

Tissue cannot be treated as a simple collection of cells; it is made of cells embedded in the extracellular matrix (ECM). ECM consists of extracellular molecules which surround cells within every type of the tissue. Depending on the tissue type, there are different volumes and contents of the extracellular matrix. For example, strength and durability of bone tissue to mechanical loading is associated with bone mineral matrix, which is made of calcium structures distributed among the collagen fibrils. On the other hand in connective tissue, where elasticity is desired, cells are scattered through an ECM that contains large numbers of collagen fibres. We can distinguish three different types of ECM component: structural proteins such as collagen and elastin, proteoglycans which 'fill' the space between cells and possess other functions which are not the concern of this thesis, and components made mainly of fibronectin and laminins responsible for anchoring ECM to cells.

At this point it is appropriate to examine the main components of ECM in detail. The most abundant is a family of proteins called collagen that make up about 25 - 30% of total body protein content [41]. The basic collagen protein is made of different α peptide chains. Collagen subunits connect with each other and create a larger complex. Then molecules assemble to form collagen fibrils, with parallel chains, tightly connected with each other, finally creating collagen fibres. Fibres are relatively long structures, which provide high tensile strength and protect tissue from tears. A schematic of collagen structure and a photo are shown respectively in figures 10a and 10b.

Another important compound in the ECM is elastin, which supports collagen and provides elasticity to help tissue to resume its original shape after tensile or contractile stress is applied. Elastin proteins form long stretchable elastic fibres, which connect to

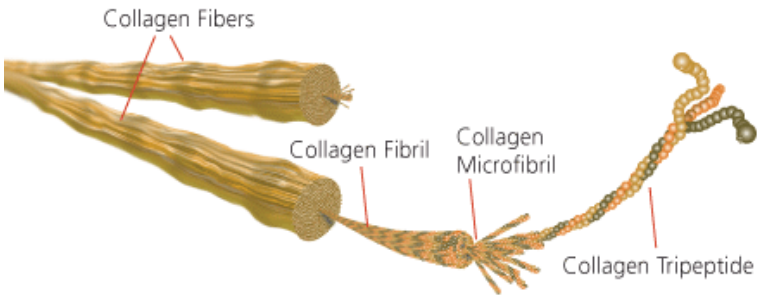

(a) Structure of collagen fibres. Reproduced from: Ref. [42]

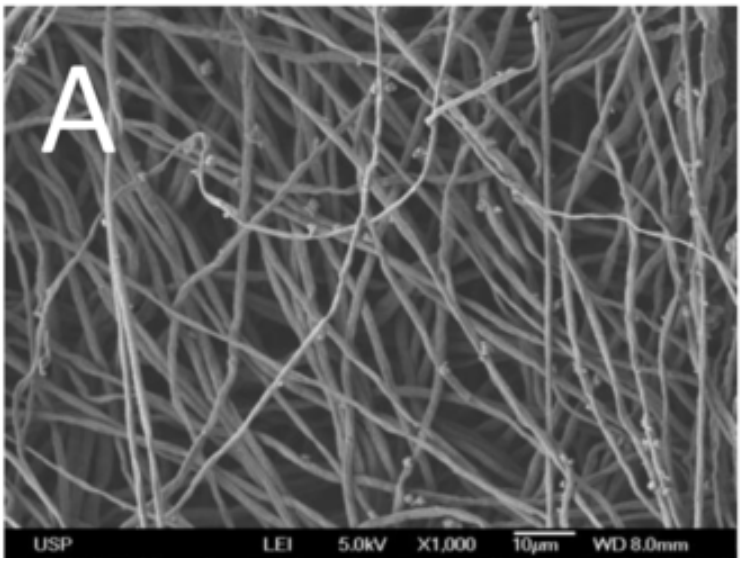

(b) Artificial tissue made of collagen fibres; fibres create a loose mesh. Reproduced from: [43].

Figure 10: Animal collagen fibres. Panel (a) presents a schematic of one collagen fibre. Progressive increase of diameter helps to make the fibres strong. Small alpha peptide chains form a collagen tripeptide. A bundle of collagen tripeptide forms a microfibril, which in a similar manner associates with other microfibril to become a bigger complex called a collagen fibril. Finally, a full-strength collagen fibre is obtained from assembly of multiple fibrils. Panel (b) shows collagen fibres, which form a loose mesh network in an artificial scaffold.

each other via covalent bonds between modified lysine residues. We can imagine fibres of elastin as a sponge or a loose net of coiled springs, which according to Hooke's Law correspond to tensile or contractile stress with an opposing force. On a macroscopic scale, these properties allow tissue to return to its previous shape, before the stress was applied. Figure 11 shows elastin fibres in the equilibrium position (top) and under stretching force (bottom). It is important to mention that the bulk of ECM consists of proteoglycans matrix, in which collagen and elastin are embedded. Proteoglycans have a protein core to which glycosaminoglycans chains are attached.

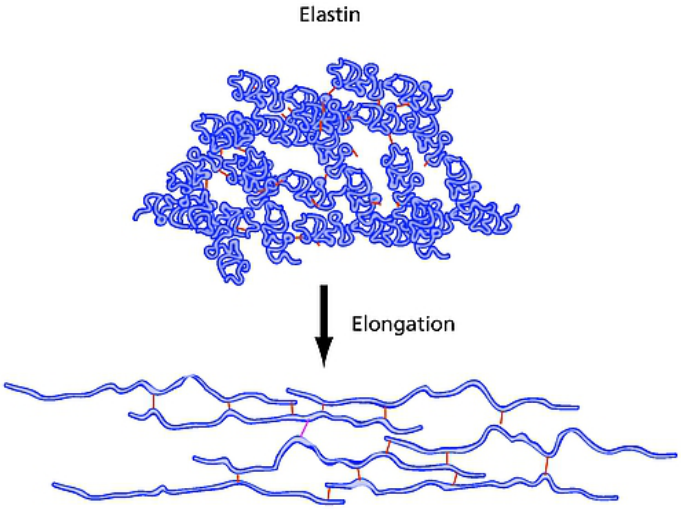

Figure 11: Elastin fibres. At the top of the picture there are contracted elastin fibres and at the bottom fibres are elongated under stretching force. The cross connections between fibres are represented in red. Credits: Sigma-aldrich [42].

The connections between the extracellular matrix and cells have to resist stresses to support and maintain the structure of tissues. The protein responsible for connecting fibres embedded in ECM and cells are integrins, which are part of the focal adhesion mechanism that were described in more detail in section 1.6. For the research described in this thesis, nervous cell to matrix connections are important and will be described in the next sections.

1.8 Nerve tissue

This section describes the ECM components of nerve tissue in both the peripheral nervous system (PNS) and the central nervous system (CNS). As mentioned in section 1.7, ECM is an important part of the scaffold within the tissue. The extracellular matrix of nerve tissue has similar components to ECM of other tissues and is mainly made from collagen, which is responsible for the physical properties and mediating of stress in all the types of tissue described below. Nerve tissue is mainly made of neurons and glial cells [12]. The components of neural tissue can vary between the CNS and

the PNS, but both include neurons. Neurons constitute an fundamental part of the systems. Their main role is to transmit electrical impulses. CNS and PNS tissues differ with respect to glial cell population types.

The CNS is made up of astrocytes, oligodendrocytes, microglia and ependymal cells [44], while in the PNS radial glia, Schwann cells and satellite cells can be distinguished. For the purpose of this research the most relevant types are astrocytes and Schwann cells which have a significant influence on nerve repair.

Astrocytes constitute an abundant and important part of nervous tissue. Basically, astrocytes have a stellate appearance with a round core and many branches surrounding them [44]. An illustration of an astrocyte and other CNS components is presented in figure 12. Their functions include helping to stabilise the position of other brain components, contributing the blood-brain barrier, helping to form a glial scar in response to any damage of nervous system and supporting the neurons [45]. Moreover astrocytes insulate unmyelinated neural processes from each other, which allow neurons to transmit electric signal in a precisely defined direction. Isolation of axons can also be achieved by the myelin sheath which is elaborated by glial cells called oligodendrocytes. In the PNS system, Schwann cells can improve regeneration of neurons following damage. These cells form the myelin sheath around the neurons as can be seen in figure 13.

Gaps called nodes of Ranvier between adjacent Schwann cells and oligodendrocytes are respectively characteristic of PNS and CNS. To highlight the importance of Schwann cells in the regeneration process, it is worth mentioning that macrophages can remove the remains of the axon and that afterwards the tunnel created by the myelin sheath helps to guide the direction of axon growth.

Furthermore, the role of Schwann cells is much more complex in the nervous tissue, as they isolate axons to conduct electrical signals along them, support modulation of

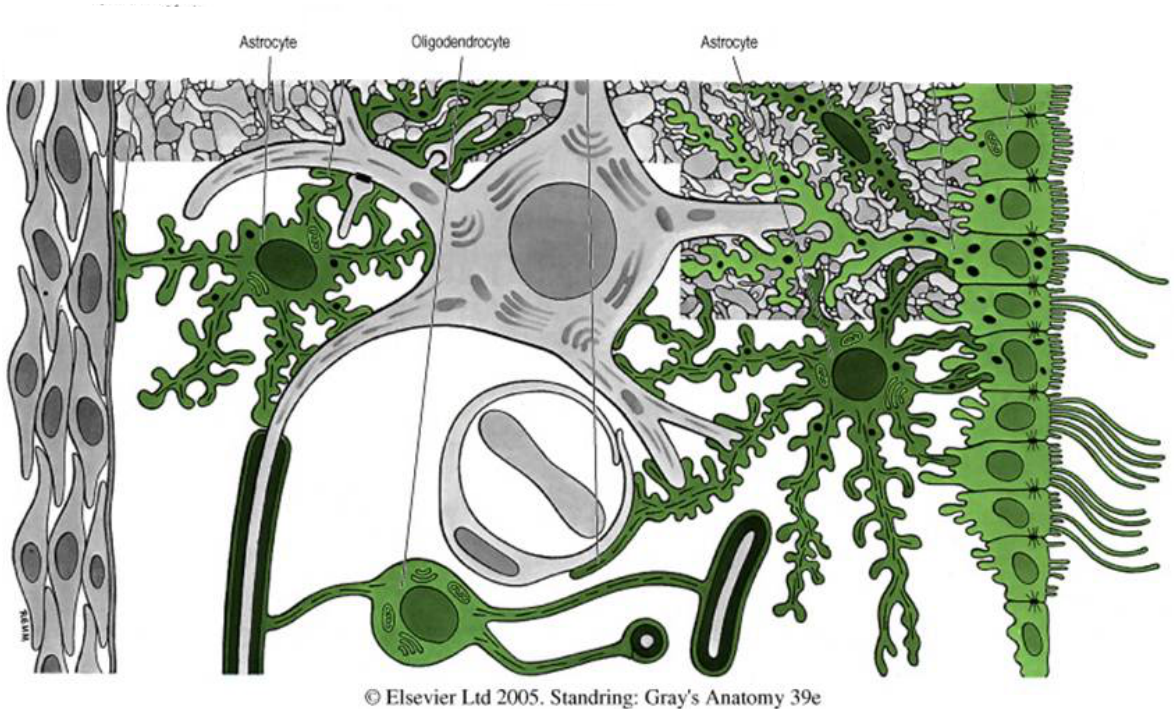

Figure 12: Structure of the nerve tissue in the central nervous system. Astrocytes connect all components of the tissue and create a strong scaffold for the neurons. Credits: ©Elsevier Ltd. 2005. Standring: Gray's Anatomy 39ed. [46].

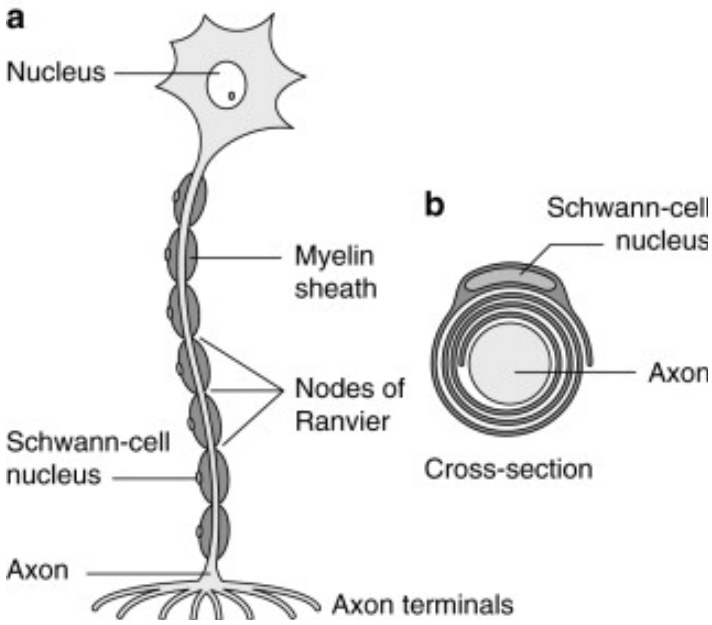

Figure 13: Insulation of Axons: Myelin Sheaths and Schwann cells a) schematic of dendrite b) cross-section of dendrite, nucleus of Schwann-cell and myelin sheath. Reproduced from : [47]

neuromuscular synaptic activity and produce the nerve extracellular matrix (ECM) [45]. ECM in neuronal tissue mainly consists of collagen in two forms as fibrils and as a non fibrillar component of the basal lamina, produced respectively by fibroblasts and Schwann cells. Collagen has a crucial role in the stabilisation of the nerve tissue,

by surrounding the processes of axons. Moreover following nerve damage, increased production of collagen was observed [4]. Collagen supports Schwann cells and increases the tensile strength of damaged axons, but in some cases, where scars exist, collagen can slow down or even block the regeneration process [45].

For the purpose of the tissue engineering technique described in Ref. [7], it is important to obtain self-alignment of astrocytes, the framework of which can be a potential guide for the neuron growth. The previous section (1.6) introduced integrins. Data show that these proteins have a crucial role in a cell's self-alignment. In particular, blockade of connections between some integrins and ECM affects orientation of collagen fibres in the tissue. This property is significant for producing tissue engineering scaffolds [48].

The approach described by Phillips at al. [7] uses embedded collagen fibres to regulate tension between the astrocytes (as a reminder, astrocytes and Schwann cells are both types of glial cells). As we know, integrins connect cells with collagen fibres, and this property allows then to regulate collagen contractions in hydro-gels. Hydro-gels are a state of matter between gel and liquid, in which suspension of cells is possible. Furthermore, collagen regulation and tension allows cells to form long anisotropic structures which create a potential scaffold for further regeneration of the damaged axons [48].

1.9 Summary

To summarise, key aspects of biology and tissue engineering have been outlined, such as movement of cells, their behaviour, type of scaffold and significant parts of the cytoskeleton and ECM. Appreciation of these mechanisms and tissue components is essential to understand the models described in the next section. Furthermore the biological context of tissue engineering is essential to understand the aim of this project,

which is to understand engineering tissue using techniques of soft condensed matter physics.

The next chapter describes aspects of soft matter physics, that are useful to understand the behaviours of cells in the presented models. We show how to transform a complex biological system into simplified systems of objects which represent cells and allow us to understand some of the complexity of tissue engineering.

2 Introduction to theories of cell organisation

In recent years more and more scientists are part of interdisciplinary teams, connecting biology with other branches of science. The challenge for physics is to extend familiar techniques and knowledge and apply them to complex biological systems. In this chapter we will describe approaches for connecting cell and tissue biology with physics. As such, a literature review which describes physical models of tissues is presented.

2.1 Limiting arrangements of cells in ECM

The study of cell systems has revealed a pattern in the relationship between components within the tissue. Between cells there is an extracellular matrix, and human biology has different tissue types for example: epithelial, connective, muscular, and nervous tissue [49]. Depending on tissue type and density, the distances between the cells and the extracellular matrix can vary. These fundamental differences in structure require different physical theories to properly describe the processes leading to cell organisation. The following correspond to the most common and characteristic arrangements of cells in tissues.

1. In the first scenario, cells can be treated as relatively big objects compared to the extracellular matrix. Distances between cells can be neglected, for example in epithelial tissue, where the volume of the ECM is minimal and interaction with the extracellular matrix can be neglected. A schematic of this kind of structure is presented in figure 14a. In this case the strength of focal adhesion connections and the time associated with cytoskeleton reorganization is sufficiently long to treat the structure as constant. These properties allow treatment of the system as a continuous medium and to apply elasticity theory. The theory described above allows us to predict the displacement and energy of that system.

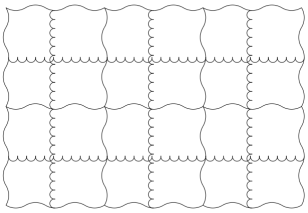

(a) Segment of tissue, made of tightly connected cells. Every spring has the same elastic constant. Models simulate the biomechanical limit and treat tissue as a continuous medium.

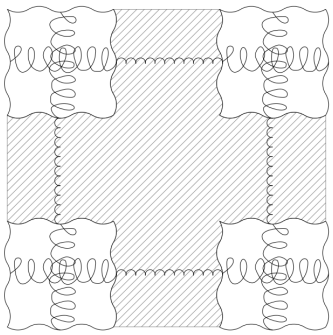

(b) Segment of the tissue, where square cells are separated by a similar thickness of the extracellular matrix. The elastic properties of the collagen fibres have a significant role in cell movement. This model assigns different elastic constants to the matrix and the cells.

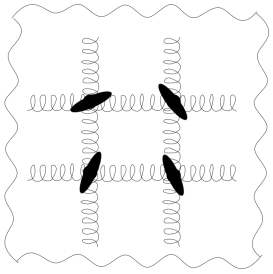

(c) Loose arrangement of cells embedded in the extracellular matrix. Cell interactions are mainly via ECM. Rotation of the cells and the change of matrix length between cells are described by expression with one elastic constant and one spring length.

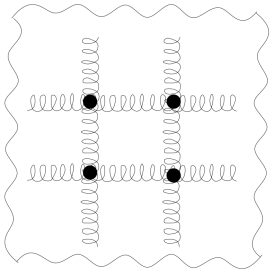

(d) A loose mesh of nonelastic cells embedded in the extracellular matrix. The position and orientation of cells are set by the interactions of the matrix.

Figure 14: Different possibilities for cells embedded in the ECM. Every picture is described by particular physical assumptions and can be used for different types of tissues.

2. In the second regime cells have a similar size to the distances between them. If the time needed for reorganisation of focal adhesion connections (see section 1.6) is enough long, the system can be approximated by elasticity theory. In this case the extracellular matrix can be treated as a continuous medium with a different elastic constant to the cells.

3. In this project, we assume a regime where cells have significant distances between them which cannot be neglected, in other words the system is treated as a loose mesh of the objects embedded in the ECM. The cells can only interact with other cells via reorganization of the focal adhesion connections (between them and the ECM), which must be fast enough to allow cells change orientation but slow enough to prohibit cells from swapping places. These assumptions, underline the fact that cross-links and focal adhesion connections are not permanent[50], especially in artificial tissues. A loose mesh of cells is shown in figure 14c, cells are represented by elongated, black ellipses, that approximate the elongated shape of the cells included in the modelled tissue (section 4). The cells are dimensionless and embedded in an elastic ECM.

4. The last regime treats tissue as an extracellular matrix with tiny cells embedded within. The influence of the interaction between cells is neglected and only linear behaviour of the extra cellular matrix is included. A loose mesh of nonelastic cells embedded in elastic ECM is shown in figure 14d.

2.2 Elasticity theory

2.2.1 Continuum elasticity theory

Soft matter physics is broad branch of science and describes a variety of physical states like liquids, polymers, gels, granular materials and liquid crystals. Many systems are

treated as continuous media and can be described by elasticity theory. Below we start by reviewing continuum elasticity theory.

Hooke's Law states that the deformation is proportional to the applied force. In the simplest case of a one dimensional spring we can write $F = -kx$, where F is force, k is spring constant and x is displacement. For continuous media, we have to consider a bulk which is subject to external force. The position of a region in the bulk is denoted by $r_i\left(\vec{r}\right)$ and u_{ik} is a strain tensor.

$$u_{ik} = \frac{1}{2}\left(\frac{\partial u_i(\vec{r})}{\partial r_k} + \frac{\partial u_k(\vec{r})}{\partial r_i} + \sum_l \frac{\partial u_l(\vec{r})}{\partial r_i}\frac{\partial u_l(\vec{r})}{\partial r_k}\right),$$

The internal forces (called internal stresses) due to intermolecular interactions try to restore atoms to their previous positions. We shall assume that the process of plastic deformation is adiabatically slow in order to maintain equilibrium thermodynamic assumptions and that molecular forces have very short range. In this case, tissue can be considered as a continuous medium. Then, as in the general case of solid bodies, the free energy is equal to

$$F = \sum_{i,k=1}^{n=3} \frac{1}{2}\sigma_{ik}u_{ik},$$

where σ_{ik} is the stress tensor and u_{ik} is the strain tensor. It is therefore possible to write the stress tensor as

$$\sigma_{ik} = \frac{\partial F}{\partial u_{ik}},$$

Alternatively we can relate the stress to the strain via

$$\sigma_{ik} = \sum_{jl} C_{ikjl}u_{lj},$$

where C_{ikjl} is the elastic constant tensor. [21, 51]

Let us consider the situation when an arbitrary external stress is applied to a solid body at constant temperature. Then we can write that when displacement tends to 0, $u_{ik} \Rightarrow 0$ and similarly internal stresses according to Newton's law are also, $\sigma_{ik} \Rightarrow 0$. In

this case all linear components are equal to zero and expansion of the free energy F in power of strain tensor has only terms of second orders respectively u_{ii}^2 and u_{ij}^2,

$$F = F_0 + \frac{1}{2}\lambda \sum_i u_{ii}^2 + \mu \sum_{ik} u_{ik}^2, \tag{1}$$

where λ and μ are Lamé coefficients.

In elasticity theory we can distinguish different possibilities of deformation of the body. First type is called *pure shear* when $\sum u_{ii} = 0$ is equal to zero but at least two terms of u_{ii} are different from zero i.e. the volume of the body does not change and shape alters. The second is hydro-static compression when volume can change and shape is maintained.

The sum of pure shear and hydro-static compression can be described by equation 2, where the specified deformation types are respectively represented by terms with brackets and without.

$$u_{ik} = \left(u_{ik} - \frac{1}{3}\sigma_{ik} \sum_l u_{ll} \right) + \frac{1}{3}\sigma_{ik} \sum_l u_{ll}, \tag{2}$$

Substituting equation 2 in equation 1, we can write a formula for the free energy

$$F = \mu \left(u_{ik} - \frac{1}{3}\delta_{ik} \sum_l u_{ll} \right)^2 + \frac{1}{2} K_b \sum_l u_{ll}^2$$

The constant K represents *bulk modulus* and can be written as a $K_b = \lambda + \frac{2}{3}\mu$. The bulk modulus is interpreted as a property of body's susceptibility stress, in other words it describes the change of infinitesimal volume according to applied infinitesimal stress and μ in the continuum elasticity theory is *the modulus of hydrostatic compression* (term definied in L. Landau and M. Lifshitz, standard in continuum mechanics [51]). The above definition after transformation can allow us to obtain the energy of the system [11].

2.2.2 Link between spring network and continuum elasticity theory.

In this thesis we will use a spring network to form part of a model. This section describes coefficients used in continuum mechanics in terms used in macroscopic systems, the derivation is based on Boal's article [52].

The potential energy of a single spring is equal to $\Delta V_{sp} = \frac{k_{sp}(s-s_0)^2}{2}$, so multiplying by the number of springs connected to a vertex (equal to 4) and dividing by 2 to avoid double counting, the potential energy represented by equation 3.

$$\Delta U_{ver} = k_{sp}(s - s_0)^2 \tag{3}$$

The area per vertex occupied by the springs under tension in a square lattice is $A_{ver} = {s_\tau}^2$. Enthalpy of the system of springs per vertex is equal to $H_{ver} = k_{sp}(s - s_0)^2 - \tau s^2$, where τ is isotropic, two dimensional tension, s_0 is length of relaxed spring, s is new length of spring. At zero temperature and under tension, the length of the spring (s_τ) is obtained by minimizing enthalpy $\frac{\partial H_{ver}}{\partial s} = 0$, the result is presented in 4.

$$s_\tau = \frac{s_0}{1 - \frac{\tau}{k_{sp}}} \tag{4}$$

In equation 4, when τ_{crit} reaches k_{sp}, this area per vertex grows without bound and network blows up. On the other hand if tension is negative then the network collapses. The free energy can also be calculated and has the form

$$\Delta F_{ver} = \frac{H_{ver}}{A_{ver}} = \frac{k_{sp}(s - s_0)^2 - \tau s^2}{A_{ver}}. \tag{5}$$

The goal now is to compare the free energy to the general expression for the free energy density for a continuum systems $\Delta F_{ver} = (K_b/2)(u_{xx}+u_{yy})^2+\mu\left[(u_{xx} - u_{yy})/2 + 2u_{xy}^2\right]$. Because of the symmetry of the rectangular system, the free energy density for a spring network on a rectangular lattice square is described by equation 6 [49].

$$\Delta F_{ver} = (K_b/2)(u_{xx} + u_{yy})^2 + (\mu_p/2)(u_{xx} - u_{yy})^2 + 2\mu_s u_{xy}^2 \tag{6}$$

In continuum mechanics there are a bulk modulus K_b, pure shear μ_p and simple shear μ_s, whereas the corresponding constant in the spring network is the elastic spring constant k_{sp}. Using equation 6 it is possible to find a relation between the elastic constant of the network and elastic moduli in the macroscopic system.

When $u_{xx} = u_{yy} = s - s_0 \neq 0$ and $u_{xy} = 0$, only the bulk modulus has impact on bulk deformation and equation 6 becomes eq. 7. Inserting $A_{ver} = s_\tau^2$ to equation 5, equation 8 is obtained (these are shown side by side for comparison).

$$\Delta F_{ver} = 2K_b \left(\frac{s - s_0}{s_\tau} \right)^2 \qquad (7) \qquad\qquad \Delta F_{ver} = (k_{sp} - \tau) \left(\frac{s - s_0}{s_\tau} \right)^2 \qquad (8)$$

Equating 7 and 8, K_b is obtained.

$$K_b = (k_{sp} - \tau)/2 \qquad (9)$$

When $u_{xx} = -u_{yy} = s - s_0 \neq 0$ and $u_{xy} = 0$, only the pure shear modulus has impact on bulk deformation.

$$\Delta F_{ver} = 2\mu_p \left(\frac{s - s_0}{s_\tau} \right)^2 \qquad (10) \qquad\qquad \Delta F_{ver} = (k_{sp} + \tau) \left(\frac{s - s_0}{s_\tau} \right)^2 \qquad (11)$$

Pure shear modulus μ_p is obtained by equating 10 and 11 It is a coefficient which describes the concurrent expansion and contraction of the bulk in orthogonal direction.

$$\mu_p = (k_{sp} + \tau)/2 \qquad (12)$$

When $u_{xx} = u_{yy} = 0$ and $u_{xy} = 0$, only the simple shear modulus has impact on bulk deformation.

$$\Delta F_{ver} = \frac{\mu_s}{2} \frac{(s - s_0)^2}{s_0} \qquad (13) \qquad\qquad \Delta F_{ver} = \left(\frac{\tau}{2} \right) \frac{(s - s_0)^2}{s_0} \qquad (14)$$

Equating 13 and 14.

$$\mu_s = \tau \qquad (15)$$

Simple shear modulus (μ_s) in a bulk element corresponds to change in an angle between the horizontal and vertical elements. Equations 9, 12 and 15 describe individual properties of the relaxed bulk, by setting $\tau = 0$ [49].

2.3 Models of tethering and cytoskeleton

Scientists are interested in modelling the different components that cells consist of. Here we will focus only on a few properties such as the shape of the membrane and reorganisation of the cytoskeleton.

The contour model is a useful approach, that tries to model a cell's surface shape depending on the tethering points where cells are anchored to the substrate. Bar-Ziv at al. use the approach to model the shape of cells adherent on the substrate[53]. Another approach is a cable model, which is described by Torres [54] , who treats the cytoskleton as a cable without resistance to contraction forces. Using a finite element method Torres [54] shows the differences between displacement of nodes in links represented by hookean springs (HSN) and a passive cable network (PCN). The restoring force of HSN and PCN respectively can be described by equation 16 (HSN) for any distance between cells L_{ij} and (PCN) by equations 16 and 17 for L_{ij} described below.

$$\vec{F}_{ij} = EAu_{ij}\vec{e}_{ij} \quad L_0 < L_{ij} \tag{16}$$

$$\vec{F}_{ij} = 0, \quad L_{ij} \leq L_0 \tag{17}$$

where i and j denote nodes in the network of cables or springs where force is applied, A is the area of the link cross section, u_{ij} is the strain tensor equal to $u_{ij} = (L_{ij} - L_0)/L_0$, $\vec{e}_{ij}$ is a dimensionless unit vector equal to $\vec{e}_{ij} = (R_i - R_j)/L_{ij}$, R_i and R_j specify the node positions. L_0 is a resting length. In Ref. [54], equilibrium shapes are presented

and compared with models that have both triangular and rectangular grids of tethering points.

2.4 Theories of cells embedded in continuous elastic media.

A complementary model to ours created by De, Zemel and Safran [55], describes the response of biological cells to mechanical forces generated by the contractile activity of cells or by external stresses. Their model includes forces due to both mechanosensitivity of cells and the elasticity of the matrix, additionally predicting the dynamics of cell orientation in both the absence and presence of applied stresses. In common with the work by Bischof and Schwarz [56], De et al. treat cells as elastic force dipoles that can change their contractile activity and orientation, through re organisational processes such as focal adhesion responses of stress fibres to external strains. Stress fibres are highly regulated structures made of actin bundles and myosin motor proteins. Each cell is modelled by an anisotropic force dipole tensor $P_{ij} = l_i f_j$where f_j are two opposite forces exerted by the stress fibres and l_i denotes the distance between the force vectors (the vector connecting the opposite focal adhesion connections), i and j are Cartesian coordinates. The force in the cell is determined from the interactions between the force dipole tensor P_{ij} and strain tensor.

Continuum mechanics provides a way to obtain the energy of an infinite medium. The influence of contractile cells can be neglected, because of the much bigger elastic constant of the ECM compared to cells. In literature, it is noted much more complicated analytical theory describing elastic inclusions in a homogeneous and isotropic medium can be found, such a theory can potentially describe elongated cells, with a size much smaller than the medium [57, 58].

2.5 Cells in the presence of external stress

As we have seen in section 1, the influence of external stimulus has serious consequences for cell movement (see section 1.3) and reorganization of the cytoskeleton (described in section 1.4). In this section we would like to focus specifically on the results of changes generated by stress. Tissues are under tension relatively often in nature, for example: blood vessels, heart, lungs and bones. Some of them are not under constant pressure but rather the direction and value of the force can vary over time. An extensive body of literature describes experiments where investigations of cells under pressure were made. Results show that active reorganisation of the cytoskeleton tries to counteract stimulus in order to support the shape and mechanical properties of the tissue. The time of reaction is closely connected with the rigidity of the substrate. It is interesting that experimental results vary: many experiments find a correlation between the orientation of the cells and the direction of applied force [59, 60] on the other hand [61] stem cells under pressure can orient nearly randomly. The situation is further complicated when cyclic stress is loaded; then the angle of cells is approximately perpendicular to the stress [61, 62] , studies also show that there is correlation between the frequency of applied stress and the angle of cells [63].

The experiments became a reason to create models of reorientation due to applied stress. There are many models of tissue type. For example the authors of Ref. [64], modelled the behaviour of stress fibres (fibres within cell, that take part during the remodelling process) within cells according to cyclic stress. Furthermore comparisons with experimental cytoskeletal stress fibers were presented in the forms of cyclic histograms, similar to those used in this thesis.

A similar theory is presented in Ref. [65] , where cells adherent on elastic substrates are modelled. The authors assumed that stress fibers reorient according to the principle of least effort, in this case aligning parallel to the direction of the applied force.

Moreover nonlinear elasticity theory was used to describe the interaction between the substrate and cells.

Finally the above consideration leads us to a description of the whole tissue system, where we are interested in cell-cell interaction. First, let us talk about models with a mean-field approximation (in the sense that cells are coupling with an external effective force field). As we mentioned in section 2.4, De, Zemel and Safran [55] described cells as force dipoles $P_{ij} = l_i f_j$. Those authors created a complex model to describe the reaction of cells in the case of applied external stress.

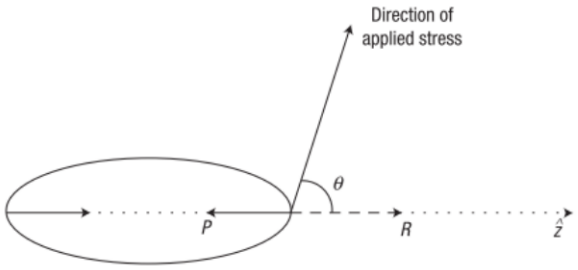

Figure 15: A needle like cell is represented by an ellipse. The force P is the response of the cell to the external applied stress in the instantaneous direction of the cell. Force R is the total response of the matrix. Reproduced from [55].

For simplicity De et al. assume that vectors f and l are both in the direction of the cell z axis, so that the stress tensor has a single diagonal component $P_{ij} = P\delta_{iz}\delta_{jz}$. The force in the matrix along the z axis is proportional to $\sigma cos^2\theta$, where σ is the magnitude of applied stress and θ is the orientation angle between externally applied stress and the instantaneous cell $\vec{z}$ axis. The $\cos^2\theta$ term treats cells as symmetric as it does not distinguish the difference between the top and the bottom of the cells (Eq. 15). To obtain the dimension of energy they defined the parameter $P_a = \sigma\pi a^3$, where a is cell size. The energy of interactions between the cell and the local environment is described by Eq. 18,

$$F_{cell} = \frac{1}{2}\xi(P_a \cos^2\theta - P - P^*)^2 \tag{18}$$

Cells regulate their contractile activities to maintain the optimal total local stress P^*. The equilibrium condition between contractile forces of cell and reaction force of the matrix is obtained when $P^* = (P_a \cos^2\theta - P)$. Moreover, there are forces not only generated by the cell, but forces generated by the matrix described by equation 19.

$$F_{matrix} = \frac{1}{2}\frac{P^2}{E'} + \frac{P_a P \cos^2\theta}{E'}, \tag{19}$$

where $E' = E\pi a^3$, E is the Young modulus of the matrix and a is cell size. The equation describes the deformation energy of one cell dipole in an infinite matrix. The matrix forces are the result of the long-range interactions between matrix and force dipoles and the direct interactions between external force and the matrix. The precise derivation can be found in Ref. [55], but for the project the key message is that the energy of the system is minimal when cells are parallel to the strain. Parallel cells contract the matrix and reduce the total strain in the tissue. Moreover the authors of Ref. [55] assume that the matrix expands when tension is not applied. The total energy for a needle like cell, interacting with an extra cellular matrix under tension, can be written as the variation of an effective free energy,

$$F_{total} = \frac{1}{2}\xi(P_a \cos^2\theta - P - P^*)^2 + \frac{1}{2}\frac{P^2}{E'} + \frac{P_a P \cos^2\theta}{E'}. \tag{20}$$

Moreover, De et al. described the time needed to reorganise the structure of the focal adhesion and stress fibers in equation (21) and to reach again the lowest energy state. Terms τ_p and τ_θ are the reorganisation times of dipole force magnitude and orientation, respectively.

$$\frac{dp}{dt} = -\frac{1}{\tau_p}\left(\frac{\partial F}{\partial p}\right) \tag{21}$$

$$\frac{d\theta}{dt} = -\frac{1}{\tau_\theta}\left(\frac{\partial F}{\partial \theta}\right) \tag{22}$$

Additionally De at al. presented a comparison with experiments investigating the changing orientation of cells due to: (a) absence of external stress, (b) the presence of constant static stress and (c) the presence of time-dependent applied stress. In the absence of the external stress, cells adjust so as to maintain optimal local force along stress fibers (leading to a mainly random orientation) [61, 66], while in the presence of quasi static external stress, cells adjust their contractile activity to maintain optimal local stress in the matrix. In other words, when force is sufficient, cells try to obtain a parallel orientation to the direction of external stress [59, 67]. In the third case, the orientation of cells was described as a function of the applied stress frequency and the relaxation time of the cells. Results showed that with increase of frequency, cells orientate nearly perpendicular to external stress [68]. This occurs beacause there is insufficient time available for reorganisation of cytoskeleton. Rumie at al. [68] investigated the interesting and unusual dependence of cell orienatation due to both optimal stress and strain of the matrix, describing correlation as a function of increasing Poisson ratio of the ECM. A more advanced approach was made by Safran and De in Ref. [69], where nonlinear elasticity theory was applied. Safran and De obtained the characteristic time of cells needed to reach equilibrium angle between cells. In addition, the experiment was extended to deal with the presence of noise. For simplicity it was be assumed that energy depends on the variation and effective temperature of angles as approximated by the Boltzman distribution.

2.6 Modeling elastic interactions between cells

The models described above focused on cell membranes or the changing of cell orientation under external force fields. In this section we want to focus on cell-cell interaction. The study of cell arrangements in tissues has led to the construction of algorithms which try to predict the behaviour of cells. In the literature we can find several examples of dipole force models which attempt to predict cell organization, in this thesis a two dimensional model is outlined.

Recent models of artificial tissue investigate the structure of tissue very precisely [21, 70] and present the interaction between cells as a dipole force, where we are not able to distinguish the top and bottom of cells [11, 21]. Schwarz and Safran [71] focused on the elastic mediated interactions between cells, treated forces as static and investigated cell reorientation on an elastic substrate under tension. The authors examined the most energetically favourable orientation of cells in two- and three-dimensional systems and additionally examined attractive and repulsive corrections to the interaction for free and clamped surfaces of tissue [71]. Further studies allowed them to find a principle where cells choose their orientation to obtain maximal effective stiffness. Schwarz and Safran [24, 71] modelled single cells and the local elastic environment as springs and explained the most favourable arrangements and shapes of cell, as shown in Fig. 16. Moreover they investigated the influence of free and clamped boundary conditions as a function of angle and distance of the cells from the edge of the specimen. The situation is similar for both regions of an elastic substrate. Cells orient parallel and perpendicular to the longest axis of tissue respectively for free and clamped boundary conditions and also for stiff and soft parts of the substrate. Bischofs and Schwartz considered a simple model for a system of many cells and used Monte Carlo simulation for the 3D case to obtain the most favourable arrangements of cells [72]. An approximation for a regular arrangements of cells in tissue is to treat them as a long chain of cells, which

can interact with other cells. Bishofs and Schwartz investigated chains of cells where orientation was fixed in one direction (with the exception of an additional single cell, that was either parallel or perpendicular to the length of the chain) [56]. This model found correlations between externally applied strain fields and average cell orientation, moreover the effective elastic constant of the system was considered. The constant describes active, long-time, effective Hookean response, which is the reaction of the cell polarisation to the applied stress. The internal force, which is the response to external stress, changes properties of the material like rigidity due to increase of Lame's coefficients[73].

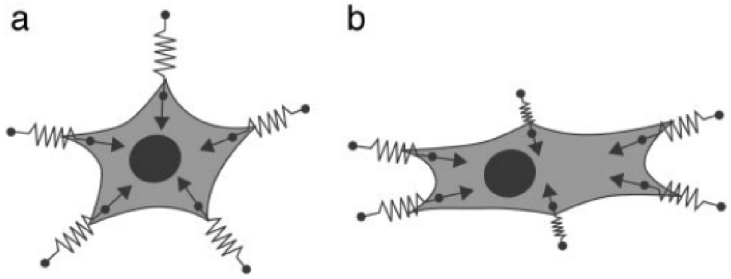

Figure 16: The local elastic environment is represented by linear springs a) cell has round shape due to isotropic tension (the same value of spring constant K) b) cell is elongate. The local elastic environment is represented by linear springs in one direction due to anisotropic tension (different value of spring constant K). Reproduced from [21].

The most relevant previous work was carried out by Bischofs and Schwarz [70]. In the Monte Carlo study done by Bischofs and Schwarz, stochastic effects on cells in an external potential field representing strain were investigated. In that study the model does not cover situations when cells can overlap and more importantly does not allow cells to change their positions. In other words all cells positions are fixed during simulations. Their simulations included about 1000 cells with periodic boundary conditions. Three state variables were identified, which determine structure formation

in a system of elastically interacting dipoles on an elastic substrate, the reduced density $\rho^* = \frac{N\pi^2}{L^2}$, the Poisson ratio ν and noise parameter T^* (reduced temperature). To control the degree of stochasticity, a noise parameter $T^* = \frac{k_b T \pi E \bar{b}}{P^2}$ was used, where T is temperature, b is the average distance between two particles in the simulation box, P - specifies the dipole strength and typically has $P = Fd \approx 10^{-11} J$, corresponding to two opposing forces of $F = 200nN$, separated by a distance $d = 60\mu m$. The noise parameter (T^*) varies between 0.1 to 3.0.

For the whole system of cells, Bischofs and Schwarz used the cost function written below to obtain the orientation of cells,

$$W = \frac{1}{2N} \sum_{\gamma=1}^{N} \sum_{\delta \neq \gamma}^{N} W_{\gamma\delta}, \tag{23}$$

where N is the total number of cells and $W_{\gamma\delta}$ specifies interaction between two cells indexed γ and δ which is given by equation 24. By minimising W, the authors try to obtain the optimal orientation of cells, when position in the tissue is fixed.

$$W = \frac{a_1 P^2}{r^3} f(\theta, \theta', \alpha), \tag{24}$$

In equation 24, $\vec{r}$ denotes the distance between cells and the cellular orientation angles, θ, θ' and α, are defined via scalar products $\cos\theta = \vec{l} \cdot \vec{r}$, $\cos\theta' = \vec{l'} \cdot \vec{r}$, $\cos\alpha = \vec{l} \cdot \vec{l'}$, where $\vec{l}$ and $\vec{l'}$ represent cell orientation, and:

$$\begin{aligned} f(\theta, \theta', \alpha) = 3(\cos^2\theta + \cos^2\theta' - 5\cos^2\theta\cos^2\theta' - \frac{1}{3}) + \\ -(1 - a_2)\cos^2\alpha - 3(a_2 - 3)\cos\alpha\cos\theta\cos\theta', \end{aligned} \tag{25}$$

where $a_1 = \nu(1+\nu)/(\pi E)$ and $a_2 = (1-\nu)/\nu$. It is important to underline that this is even function corresponding to symmetry under 180° rotation of l and l'.

Bischofs et al. [70] obtained various configurations of their 2D cell system as a function of different parameters. The first of them relates to the influence of noise on cells arranged in a lattice. To perform the simulations, different Poisson ratios and reduced

temperatures were applied. Results of the simulations show that cells form much more string-like structures with increasing ν and decreasing T^*. Additionally temperature changes led to phase transitions between string-like structures and ring-like structures.

Weak positional disorder was also investigated. To apply this perturbation, the locations of cells were randomly moved away from position on the ideal square lattice, within a circle with radius r. A new disorder parameter f was introduced, defined as $f = r/b$ where b is lattice constant. Bischofs at al. found that the long range orientation changed in a similar way as with increase of T^* parameter [70].

Further analysis concerned changes of elastic moduli, cell density(reduced density ρ^*), noise(T^*) and cell position geometry. Cells were randomly arranged as the in previous case. Results showed that at low densities cells totally lost any string-like or ring-like arrangements. With increasing ρ^* it is possible to find a close relation between ordering and the Poisson ratio. Additionally the authors identified a number of cell orientation phases: nematic, disordered (isotropic), ring-like and ordered (anisotropic) orientation. 3D simulation of a small 100 cell system was also made, showing the orientation of cells according to poison ration and clamped boundary conditions.

2.7 Summary

In the literature, we can find several different models, which try to describe arrangements of cells. All models are based on linear or non linear elasticity theory. There are still only a few comparisons between the results of real experiments in engineered tissues and physical models. Models of tissue still need more research to fully describe the interaction between cells. In the next chapter, the model used in this thesis is

described along with methodology to solve it. Our aim is to simulate behaviour of cells in real engineered neural tissue.

3 Methodology and Models

The purpose of this chapter is to introduce a numerical algorithm to simulate the organisation of cells in tethered artificial tissue. The algorithm has to simulate real artificial tissue, where mean field approximations are not valid and other simple existing methods do not work properly. Most of the existing approaches described in the previous chapter try to find general laws of cell organization in tissues in external fields and with periodic boundary conditions. Furthermore most models deal with a static substrate. A key aim of our work is to extend these models to situations where the substrate can move, such that we can predict the patterns of cell formation in tethered artificial tissue. The algorithm presented here aims to simulate real tissue made in vitro.

We will start by suggesting a Hamiltonian to describe artificial tissue. When the Hamiltonian describing the model is obtained, it is essential to apply appropriate computing methods. The system contains an enormous number of cells, so a full solution requires very fast and powerful computers. Fortunately to understand behaviour of cells it is satisfactory to compute interactions within a smaller system. We complete this chapter by presenting the most common techniques that can be used to solve optimisation problems.

3.1 Models

Our algorithm attempts to describe the structure of cells found in experiments results. To create the cost function, we used the assumption presented by De [55] and treat cells as sticks with no distinction between top and bottom, which is an idealized description of the shape of cells in the tissue. The cost functions are phenomenological and aim to represent the minimal interaction consistent with symmetry, while taking guidance

from the structures found in the experimental samples discussed in the next chapter. Let us consider two cost functions presented below.

The first is

$$W = \sum_{i,j\neq i}^{N} \cos^2 \theta_{ij}, \tag{26}$$

which is a simplified version of the force dipole model and is the simplest interaction, consistent with the symmetry of the problem. θ_{ij} is the difference between orientations of cell i and its neighbour j and it represents exchange interaction between cells. If cells are parallel to each other, the Hamiltonian has the lowest possible value. The square of the cosine function does not distinguish between the top and bottom of the cells, as it has period π. In this model cells do not move positions.

The second cost function describing our system of cells is equal to:

$$W \equiv \sum_{i,j\neq i}^{N} W_{ij} = \sum \frac{k}{2}(|r_{i,j}| - l_{i,j} + \Delta l(2 - \cos^2 \alpha_1 - \cos^2 \alpha_2))^2, \tag{27}$$

where to describe interaction energy between cells we used spring network, W_{ij} is the potential energy of the spring and describe energy between cells denoted by i and j, $l_{i,j}$ is the equilibrium lattice distance for an untethered, infinite structure as presented in fig 17, Δl parametrises the change of contractile stress as a result of the cell's orientation and N is the total number of cells, finally $|r_{i,j}|$, describes the current distance between cells. The equation has dimension of energy because we multiply expression in the brackets by a constant $k/2$, which has to be selected experimentally. In practice, all terms are multiplied by k, so it does not contribute to the form of the optimal structure. If we assume that $\vec{l_1}$ and $\vec{l_2}$ represent orientation of cells, then the angles α_1 and α_2 are defined from the scalar products $\vec{l_1} \cdot \vec{r}_{1,2}$ and $\vec{l_2} \cdot \vec{r}_{2,1}$, respectively. These angles are shown schematically in figures 18a and 18b.

Figure 17: Schematic showing needle-like cells, placed regularly on a square lattice at the top of the picture and lattice points at the bottom. The lattice constant is d in both y and x direction.

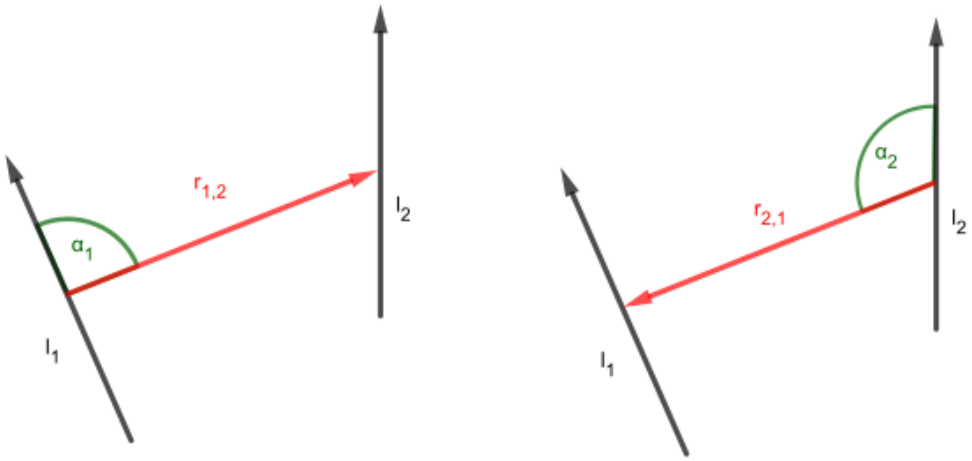

(a) System of two cells with denoted angle α_1 computed from $\vec{l_1} \cdot \vec{r}_{1,2}$.

(b) System of two cells with denoted angle α_2 computed from $\vec{l_2} \cdot \vec{r}_{2,1}$.

Figure 18: Schematic of two cells with distance $\vec{r}_{1,2}$ between them showing angles α_1 and α_2, respectively.

The main role of the Hamiltonian is the description of interaction between cells mediated by the extracellular matrix. In this thesis we assume that focal adhesion contacts and collagen fibres are responsible for both contractile and stretching forces. More detailed examination of the Hamiltonian indicates that the minimum of energy for an infinite lattice with lattice constant d occurs when angles between lines connecting the centres of two cells and their orientation (respectively α_1 and α_2) are equal to zero. Moreover when both cosine functions are minimal, then the Δl term is maximal and the Hamiltonian has a reduced bond length. Another important term in the Hamiltonian is the constant $l_{i,j}$, which can change the equilibrium distance between cells to match experimental tissue. The described function can be fully adjusted to match experimental values by varying three constants $l_{i,j}$, k and Δl.

In our work, we try to find a model of engineered neural tissue which is anchored to the tether along the shorter edge, in a similar way to samples presented in Ref [7]. The model has potential to be suitable for other artificial tissues, because the constants $l_{i,j}$, k and Δl, can be changed to simulate different size of the mould or type of cells. In both cost functions, the interactions are neglected for distances greater than a characteristic cutoff range.

3.2 Simulated annealing

Taking into account the large number of variables, (i.e. the different position and orientations of each cell), obtaining the global minimum is a very time consuming task. The global minimum can be estimated using a simulated annealing algorithm. The simulated annealing algorithm was originally suggested by Kirkpatric, Gelett and Vecchi and when properly applied guarantees the reaching of a global minimum [74]. Simulated annealing is based around a Metropolis algorithm [75], where temperature is slowly lowered. In this sense it acts analogously to the slow annealing of metals and

glasses that is used to improve their properties. Here we present briefly the algorithm that is used in this thesis.

1. Read initial positions and orientations of cells from a file
2. Set initial temperature, T_0
3. Loop until ($T_i < T_f$) condition is true.
   (a) Randomly choose cell.
   (b) Change position if not tethered
   (c) Calculate the energy of the new configuration
   (d) Accept new position and orientation according to the probability P_i^f, described below (equation 28)
   (e) Decrease the temperature - new temperature is proportional to the previous one, $T_{i+1} = (1 - a)T_i$

The algorithm uses random generator ran2, which generates a floating point number between 0 and 1 [76]. In a "loop" Ran2 is quick enough to be called a few times per iteration, without significant delay to the whole program. Moreover, the random generator has a long period, which avoids situations where generated numbers are repeated. In more detail, the algorithm uses the random generator to choose one of the cells and if the cell is not tethered, changes its position and orientation. The closest cells to the tether points cannot change their position, thus their energy depends only on cell orientation. On every step the algorithm changes position by a value between -3 and 3 μm and the orientation by between 0 and 2π radians. The position has to be changed by a small amount to prevent cells from jumping over each other.

On every iteration the algorithm computes only the difference between previous and

current energies. Next, the new configuration is accepted or rejected according to the condition shown in Eq. 28.

$$P_i^f = \begin{cases} e^{-(W(j)-W(i))/T(t)} & \text{for } W(j) > W(i) \\ 1 & \text{for } W(j) \leq W(i) \end{cases} \tag{28}$$

As mentioned before, the $l_{i,j}$ constant describes the minimum equilibrium distance between cells when tissue is untethered. In this work we used a constant equal to 20.00 μm. As we mentioned Δl describes change of contractile stress and has to be big enough to change significantly the value of the whole Hamiltonian for every change of the the angles.

P_i^j describes the probability of accepting the new state j. $W(j)$ and $W(i)$ are the energy of the current (j) and previous (i) iteration. T depends on iteration and is reduced from very high values. The constant a is responsible for a small decrease of the temperature in every iteration. If $T(t)$ is reduced sufficiently slowly, the global minimum of W is guaranteed [74, 75, 77].

Depending on simulation, the coefficient a varies from 5×10^{-10} to 1×10^{-6}. After many iterations the value of the temperature becomes very small and when it reaches a value equal to $T_f = 10^{-10}$, the annealing process is ended. The slowly decreasing temperature lets the algorithm leave all possible local minima which are found during the simulation. Moreover the initial temperature T_0 is proportional to the number of cells, so the program can work properly for all sizes of cell system.

Another modification of the method is the fast simulated annealing algorithm described in ref. [78]. The technique is possible to apply to our system, as the basic idea is similar to the simulated annealing (SA), algorithm described here. In practice fast annealing did not give such good results.

3.3 Other optimisation methods

In the previous section of this chapter, we described a powerful and straight forward technique to obtain the global minimum, now let us present other methods with their disadvantages and advantages. A full review of the described methods is available in Ref [79]. There are several different methods that could be used to obtain the minimum of the function [76]. The important factors are speed, difficulty of application and degree of certainty that the obtained minimum is global.

3.3.1 Conjugate gradient method

Conjugate gradient method is a simple and fast way to obtain a local optimum. The algorithm can quickly find the direction of changes, but the main disadvantage is in ability to escape from a local minimum. If a complicated function is considered, the algorithm is not guaranteed to find global extrema.

At this point, the execution scheme is briefly explained. First we choose some point in the space x_i. In the next step the algorithm needs to estimate the direction of the minimum and therefore computes the gradient at the point. Then it finds a new point in the following way $x_{i+1} = x_i + h\nabla f(x_i)$, where the distance from the previous point depends on h. The last step requires us to obtain h, which is the value that minimises the function for the new point. The scheme proceeds until the gradient is equal to 0 [76].

Below we present an algorithm which could be applied to the problem studied here, as a first step to speed up the annealing process [76].

1. Read initial positions and orientations of cells

2. Select a position x_i in the space of cell positions and orientations

3. Define a cost function $f(x_i)$

4. Loop with $h = 0$

   (a) Obtain gradient of the function $\nabla f(x_i)$

   (b) Compute $x_{i+1} = x + h\nabla f(x_i)$, repeat for every variable

   (c) Obtain h, equal to $min\,(x_{i+1}\,(h))$.

   (d) Get a new point x_{i+1}

3.3.2 Threshold acceptance

Recent studies demonstrate a powerful heuristic method, as noted in the work of Dueck and Scheuer [80] and independently published by Moscato and Fontanari [81]. The method is easy to implement and typically has faster execution time compared to simulated annealing, although it can be difficult to find a proper threshold scheme. A few versions of the algorithm have been presented [80, 82]. Here we present an algorithm which is applicable to our project.

1. Define a threshold temperature, T_r

2. Loop over the threshold reducing it until $T_r < T_{r_0}$

   (a) Randomly choose cell.

   (b) Change position and orientation of cells

   (c) Compute interaction between cells

   (d) If energy(new system)<energy(old system) + T_r, then accept change

The threshold (T_r) represent temperature, has a similar role to temperature in the SA algorithm and can be reduced in the same way as SA. The algorithm stops when it reaches the lowest value of threshold T_{r_0} which must be much smaller than the depth of the global minimum. Unfortunately, there is no universal method, which allows us

to find a global minima with a fast execution time. In spite of this it can be shown that it is always possible to find a threshold that allows us to find the global solution [76], [83].

3.3.3 Genetic algorithm

The last method described in the introduction is also the most complex and sophisticated. Genetic algorithms have their origin the biological sciences, as they try to emulate the evolution processes of the DNA code. In biological processes, natural selection leads to progressively filter individuals, whereas in a genetic algorithm more optimal configurations are selected on each step. Let us present a genetic algorithm adjusted to solve our problem. The first a pool of tissues-systems is generated, each with different positions and orientations of cells. In the second part a new generation of populations is generated by crossover and mutation operations, which make changes in the system. The next part of the algorithm requires us to check the relative fitness of the population, in other words whether energy is higher or lower. Similarly to nature, selection allows only the best part of the population to survive. Mutation operations act similarly to annealing updates to change the attributes of single cells. In the particular problem studied in this thesis, crossover could change position and orientations of a large group of cells in one step. Unfortunately, the technique does not guarantee that global minimum is reached and it is much more complicated than SA[84].

3.4 Summary

We described a function to describe the energy of a particular configuration of cells and how it can be optimised using simulated annealing. For completeness, we described the most common optimisation methods, which are applicable to systems similar to that presented in this thesis. To sum up there is no single best method. The optimization

methods described here are the last section of the introductory part of this thesis. The next chapter describes the statistical analysis of the experimental systems that will be explained in the thesis.

4 Experimental data and its features

A key part of the project is comparison between the theoretical model and experimental data. We have access to microscope images taken from artificial tissue grown at the OU and UCL by the group of James Phillips. To make the comparison possible we have determined the histogram of cell orientations in the tissue. This was a major task and the main issue was analysing confocal micrographs (presented in figures 19, 20). To solve this problem, image analysis was conducted using Volocity software (Perkin Elmer, Waltham, MA) which allowed us to map the position of every single cell in the tissue samples. Moreover, we developed software to obtain histograms of cells orientation in the tissue from this raw data. For our purpose, a set of two dimensional histograms of cells was sufficient, therefore the three-dimensional map of the engineered neural tissue was flattened into the xy plane. Next, the program divided the tissue into the smaller parts, which each included a set of cells. Specifically, cells with specified position coordinates were assigned to a rectangular region to examine the histogram of cell orientations. In this way, many histograms of angles, each describing small regions of the tissue were obtained. Finally, a map of the angles of cells in the tissue was created. Every histogram gives the relative frequence of the number of cells orientated in a certain direction, in other words every bin of histograms has information about the number of cells, oriented within a defined range of the angles.

This analysis allows us to characterise the most significant parts of the tissue. In Fig. 24 a schematic is presented, where main regions are denoted by numbers 1, 2 and 3, which respectively indicate regions along the edges, middle of the tissue and delta regions. In the delta regions cells are mainly perpendicular to the longest axis of the tissue, in the middle region average orientation of cells is parallel and along the edges

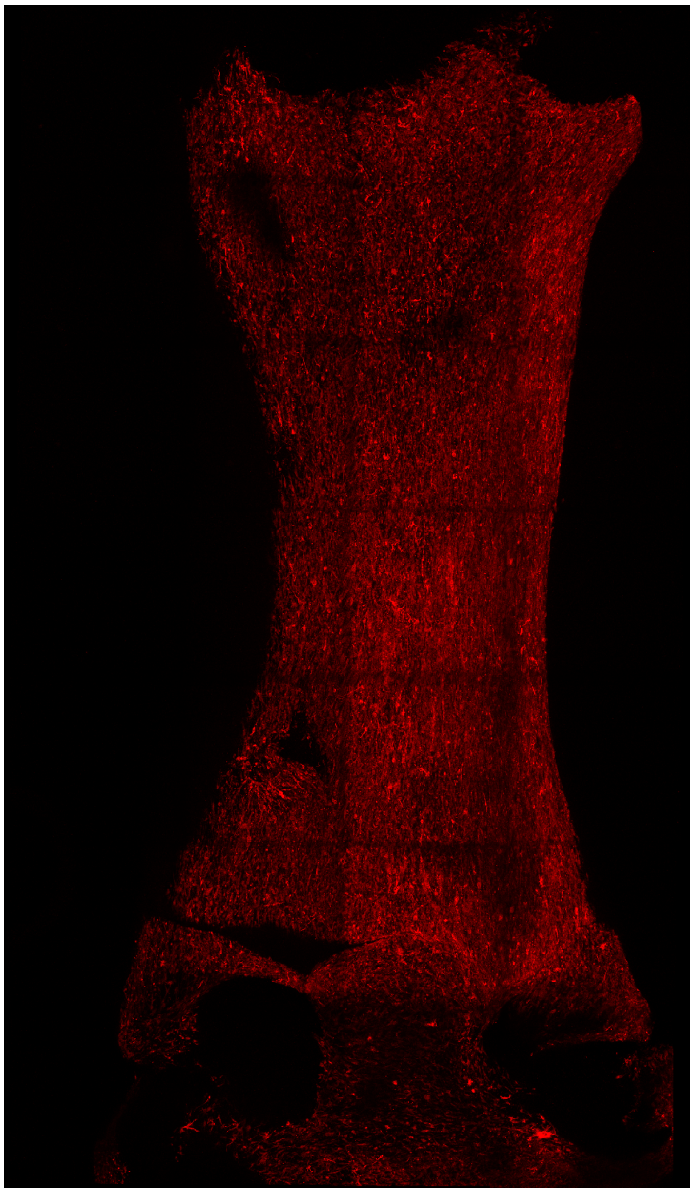

Figure 19: Artificial neural tissue, consisting of glial cells. Image size is 3100×5425 μm in extended focus. Glial cells are stained by βIII tubulin. The picture shows a three dimensional sample, which has been flattened into a two dimensional maximum intensity projection. Credit to Caitriona O'rourke and James Phillips.

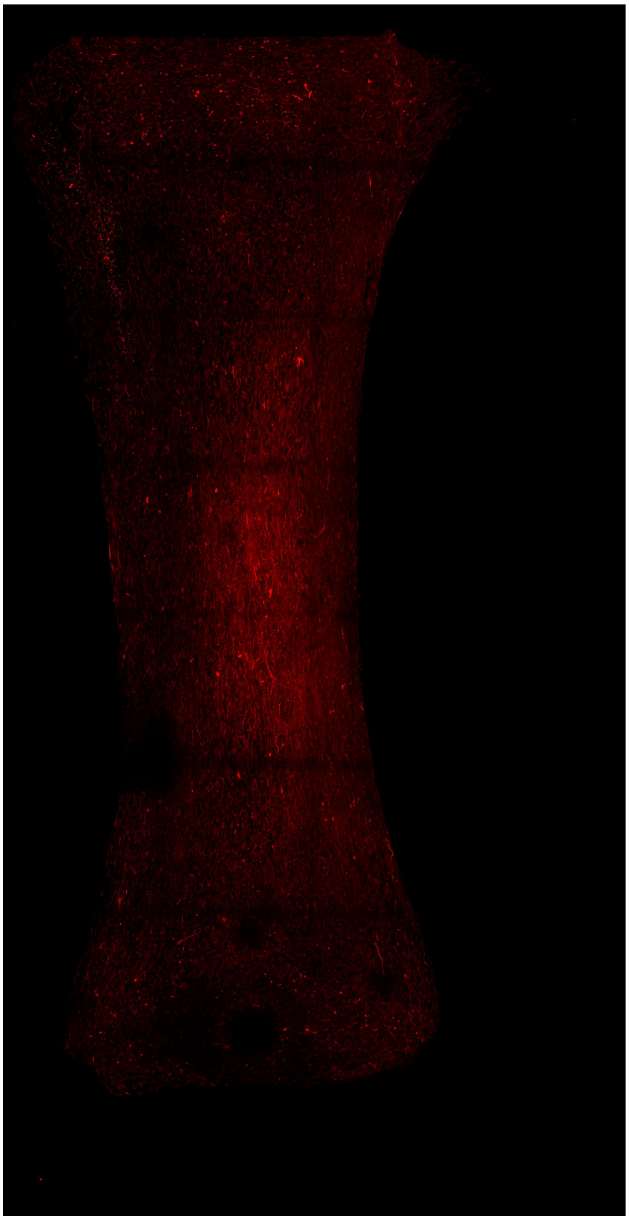

Figure 20: As figure 19, alternative sample. Credit to Caitriona O'rourke and James Phillips.

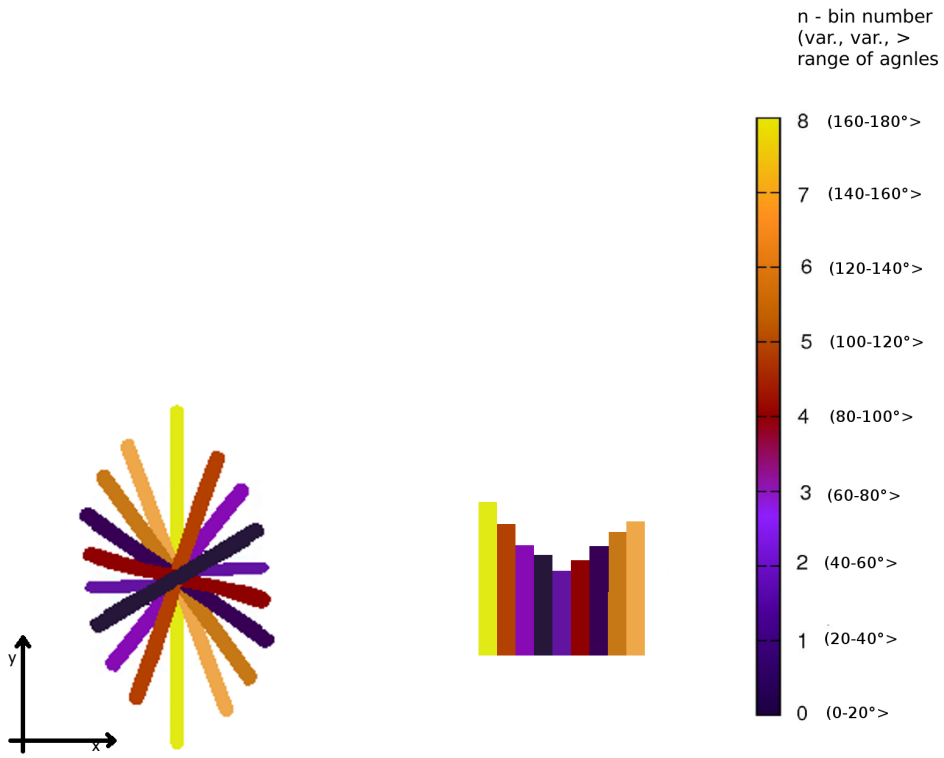

(a) (b)

Figure 21: Two different charts representing the same histogram. a) A single "flower" presenting a histogram of cell orientation within a volume of $200 \times 200 \times 90$ μm^3. The direction of lines corresponds to the angle $0-20°$,...,$160-180°$ relative to the longest axis of tissue. Every color of line shows us the relative number of cells within a particular range of directions. The probability of finding this orientation in the region of tissue, ranges from the lowest probability represented by purple to the highest probability which is yellow. b) Identical histogram to graph to panel a), but presented as a bar chart. The colours, length and arrangement of the bars have the same meaning. The alternative 'flower' representation of the histogram, makes it easy to find the most probable orientations of cells in the tissue.

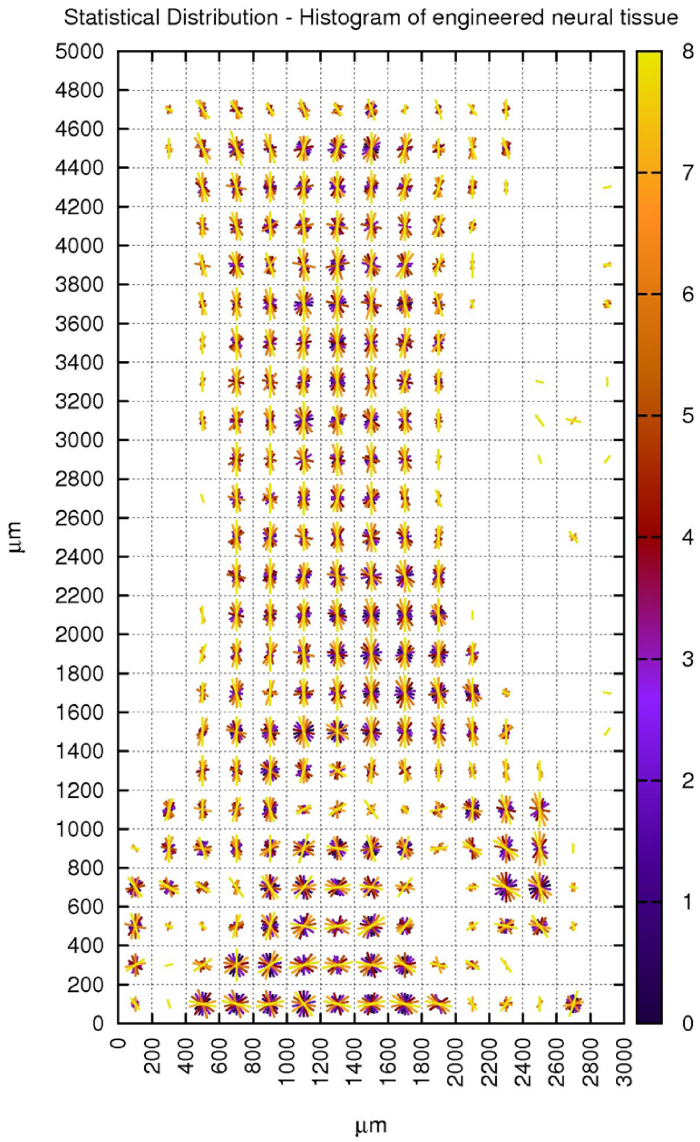

Figure 22: Histogram chart of cell orientation in artificial neural tissue. The histogram represents cells included within the tissue sample presented in figure 19. The yellow bars represent the most probable orientation of cells. Towards the centre of the sample cells are aligned vertically. Whereas cells are aligned horizontally near tethering points, where the variation of the cell orientation is largest. At the edges of the tissue, the density of cells is much smaller than in the central regions. In particular, there is a visible lack of cells near tethering points.

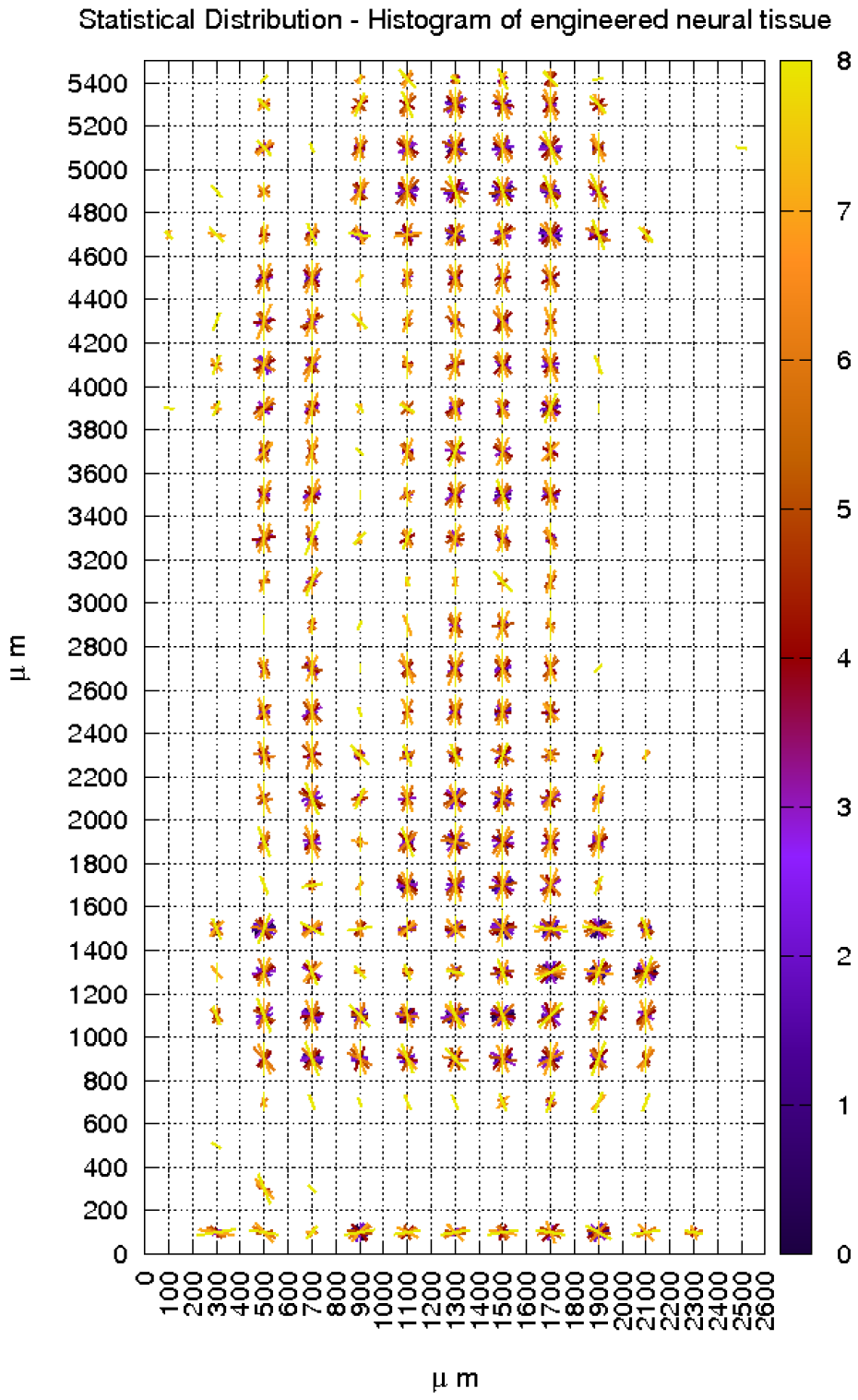

Figure 23: As figure 22, but based on the sample shown in figure 20, orientations are broadly similar to the first sample.

(region 1) cells should be aligned to the outer shape of the tissue. In this case the shape of the tissue is simplified to two dimensions. Our aim is to understand this structure.

Photographs in figures 19 and 20 present the end stage of the growth of artificial neural tissue. At the beginning, cells are seeded throughout the volume of the sample. During the growth process, cells which are far from tethering points have a tendency to move inwards toward the middle of the photographed region due to tension. The tension is caused by the interaction between cells and cell-tethering points. The growth process of cells causes squeezing of the tissue, on the other hand cell-tethering points do not allow cells to move. It seems that interaction between tethering points in the sample and the cells are significant enough to create tension perpendicular to the axis of the tissue. Using our software we were able to obtain the histograms presented in figures 22 and 23. The histogram chart represents a four dimensional space contained in a two dimensional graph. Every flower represents information about the cells included in a corresponding rectangle of the tissue. The following information are presented: the average position of the rectangular region, typical angles of cells and the difference between the number of cells in every bin of the histogram. While the presentation is unusual, simple averages cannot be used due to the periodic nature of angles. There is an explanation of a single histogram "flower" in figure 21. The important point is that we are able to systematically create more two dimensional graphs of different tissue samples to obtain a broader comparison base. Unfortunately the density of cells in the tissue samples is too low to let us to create reasonable three-dimensional histogram charts.

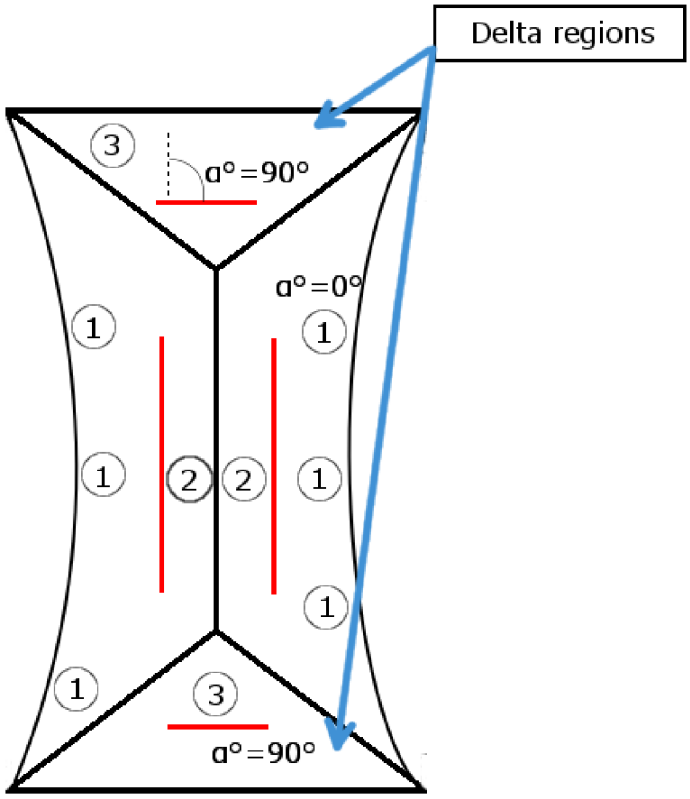

Figure 24: Schematic showing the distinct regions of orientation of cells in the tissue.

5 Results from theoretical models

This chapter describes results from our simulations of cell models in the two dimensional plane. The discussion is concerned with the results generated with the two Hamiltonians, that are described in chapter 3.1. The simulations presented here were made using the simulated annealing algorithm (section 3.2), which in most of the simulations reached the global minimum. Each Hamiltonian aims to understand different aspects of tissue engineering. The charts show the arrangement of cells obtained from simulations of the engineered neural tissue that was described in section 4.

5.1 Simple model

In this thesis the phrase 'chain of cells', denotes a vertical line of cells and both the y axis and vertical are defined as the longest axis of the tissue. As we mentioned in chapter 3, T_0 is used to denote initial temperatures of the system, the temperature is multiplied by the coefficient $(1 - a)$ on every iteration, Δl is called contraction length and l describes the equilibrium distance between cells.

Figures 26, 27 and 28, 29 present results obtained for the cost function $-kcos^2\alpha$ (Eq. 26) where the k constant is expressed in $[N/\mu m]$. The graphs represent to the engineered neural tissue described in chapter 4. The density of engineered neural tissue is 7.52×10^{-6} *cells per* μm^3, whereas the histogram of cell orientations (figure 22) represents 2D projected tissue with density equal to 7.52×10^{-4} *cells per* μm^2. In the results generated with simple model the density of sticks representing cells is equal to 6.25×10^{-4} *sticks per* μm^2. One stick represents 0.83 of cells group. In the thesis 'cell' and 'stick' denote group of cells marked on the graph as coloured segments.

To generate the graphs, the algorithm is initiated with a regular grid of cells, spaced by $40[\mu m]$. The following parameters were used: The system used in simple model

consists of 5825 cells, $l = 20$ $[\mu m]$, $\Delta L = 20$ $[\mu m]$.

The common feature in figures 26 and 27 are fixed boundary conditions, more precisely the outer most cells have fixed orientation along the long edge (outline in Fig. 25a). The first set of figures present data obtained after 30×10^6 iterations and during the simulation parameter T_f is equal to 10^{-9} $[pJ]$. Figures 26a, 26b and 26c show results from the model computed with 90, 60 and 45 μm cutoff range. This corresponds to the energy computed by including 12, 8 and 4 adjacent cells, respectively.

In figure 26a most cells are orientated parallel to the longest axis of the tissue. There is one distinct arrangement perpendicular to the y axis in the lower-right corner, close to the fixed cells. With decreasing cut off range, it can be noted that more and more cells orient perpendicular to the longest axis of the tissue. In graph 26b cells in the central region are oriented perpendicular to the longest axis of the tissue and at the top and bottom cells form delta regions. In the last graph most cells have a different orientation than y direction, moreover many sticks have very different orientation on the right-bottom side.

The next set of graphs (Fig. 27) show results of simulations obtained after 30×10^7 iterations. Parameter T_f equal to 10^{-10} pJ was used to generate results. The graphs presented in figures 27a and 27b show cell mainly oriented parallel to the y axis, there is a small group of cells with different orientation on the right bottom side. In the second graph regions close to cells with fixed position and orientation perpendicular to the y axis show perpendicular orientation to the long axis. Similar regions are seen in graph 27c, where result are generated with the shortest cutoff range equal to $45\mu m$. Moreover results presented in the graph show a significant delta region at the bottom of the tissue. The delta region shows strong perpendicular orientation. Rest of the tissue shows distinct parallel orientation to the long axis of the tissue. When the cutoff range increases then number of cells oriented in the same direction increases too.

The comparison between figures 26 and figure 27 shows that the number of cells with parallel orientation to the y axis increases according with the longer annealing time.

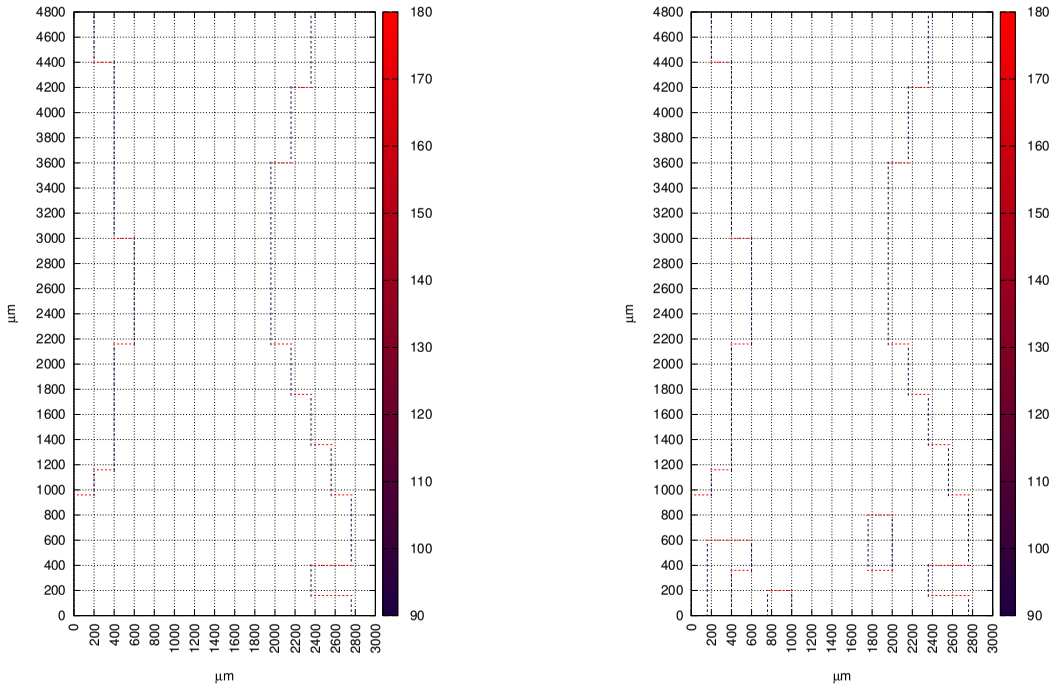

(a) (b)

Figure 25: Boundary conditions (fixed orientation cells), which were used in the simulation of the simplified model. Fig. 25a shows positions and orientations of cells fixed around the long edge and in Fig. 25b cells are fixed along the long edge and around tether points (holes). The fixed cell orientation arrangement presented in Fig. 25a was used to generate results in Fig. 26 and 27, while the arrangement presented in Fig. 25b was used to generate results in Figs. 28 and 29.

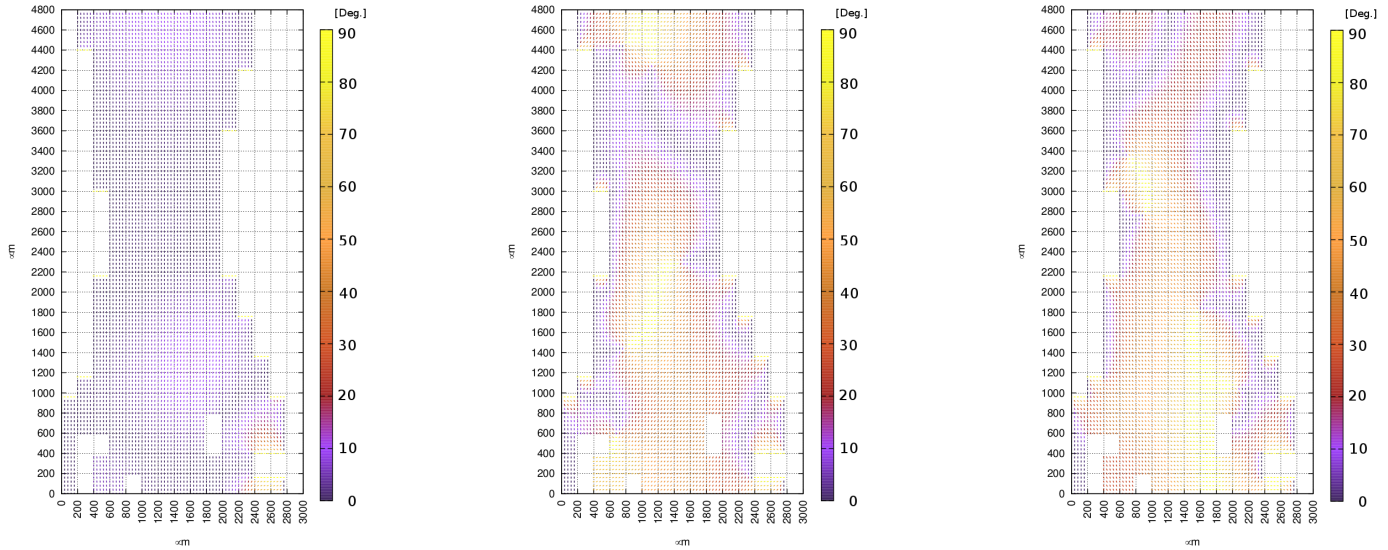

(a) Cutoff range = $90\mu m$ (b) Cutoff range = $60\mu m$ (c) Cutoff range = $45\mu m$

Figure 26: Result of simulation with fixed orientation of cells along the longest edge (y axis). Results were obtained after about 30×10^6 iteration. The dark blue colour denotes cells parallel to the longest axis of the tissue (0°), while yellow denotes cells perpendicular to the longest axis of the tissue (90°).

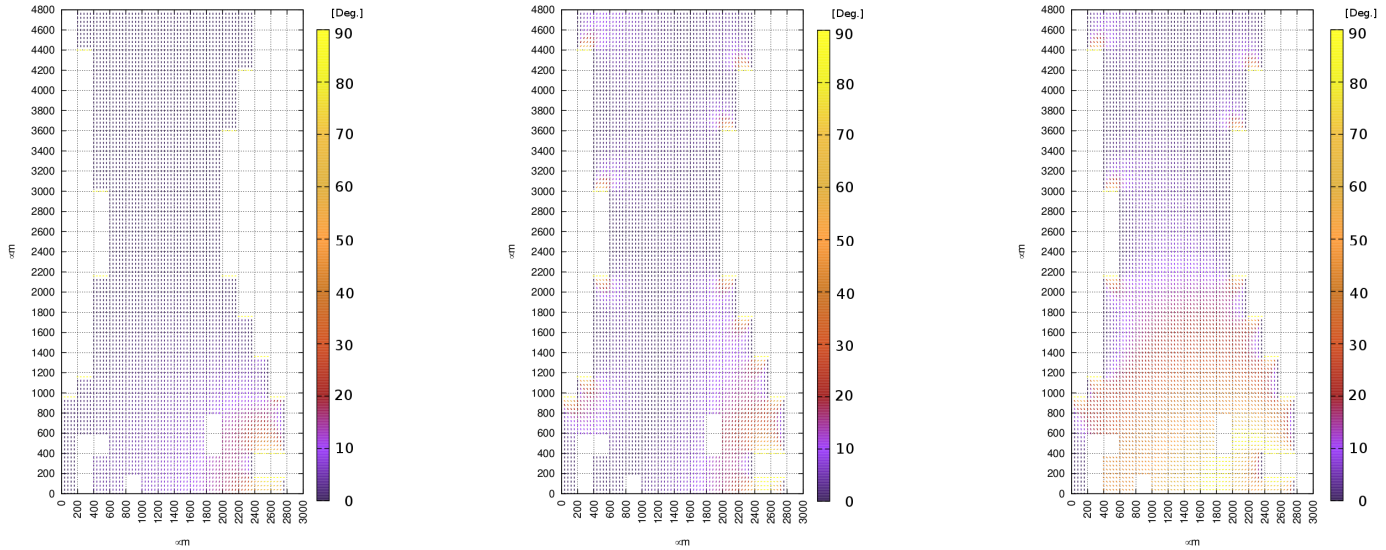

(a) Cutoff range = $90\mu m$ (b) Cutoff range = $60\mu m$ (c) Cutoff range = $45\mu m$

Figure 27: As figure 26, but with results obtained after about 30×10^7 iteration.

The difference between figures 26, 27 and 28, 29 is connected with the boundary conditions. In figures 28 and 29 the outer most cells have fixed position and orientation along the edges and around tethering points (visible at the bottom of the tissue, fixed cells arrangement is presented in figure 25b), whereas in figures 26 and 27 cells have fixed position and orientation along the edges (fixed cells arrangement is presented in figure 25a).

Similarly to figures presented before, graphs in figures 28 and 29 are presented respectively with decreasing cutoff range 90, 60, 45 μm. Figures 28 and 29 present data obtained respectively after 30×10^6 and 30×10^7 iterations. In figure 28a there are two regions at the bottom of the tissue, where cells orient perpendicular to the longest axis of the tissue. Figure 28b presents cells oriented parallel to the y axis at the bottom and top of the tissue, whereas in figure 28a cells orient at the middle and bottom part of the tissue. In both figures there are regions similar to the delta regions. Comparison of figures 28 and 29 shows that including additional fixed cells around tether points strongly changes the arrangement of cells in the tissue.

In figure 29, all the graphs show explicit delta regions at the bottom of the tissue. The most regular orientation of cells in delta regions is visible in figure 29a. With decrease of the cutoff range the delta region are less regular and symmetrical.

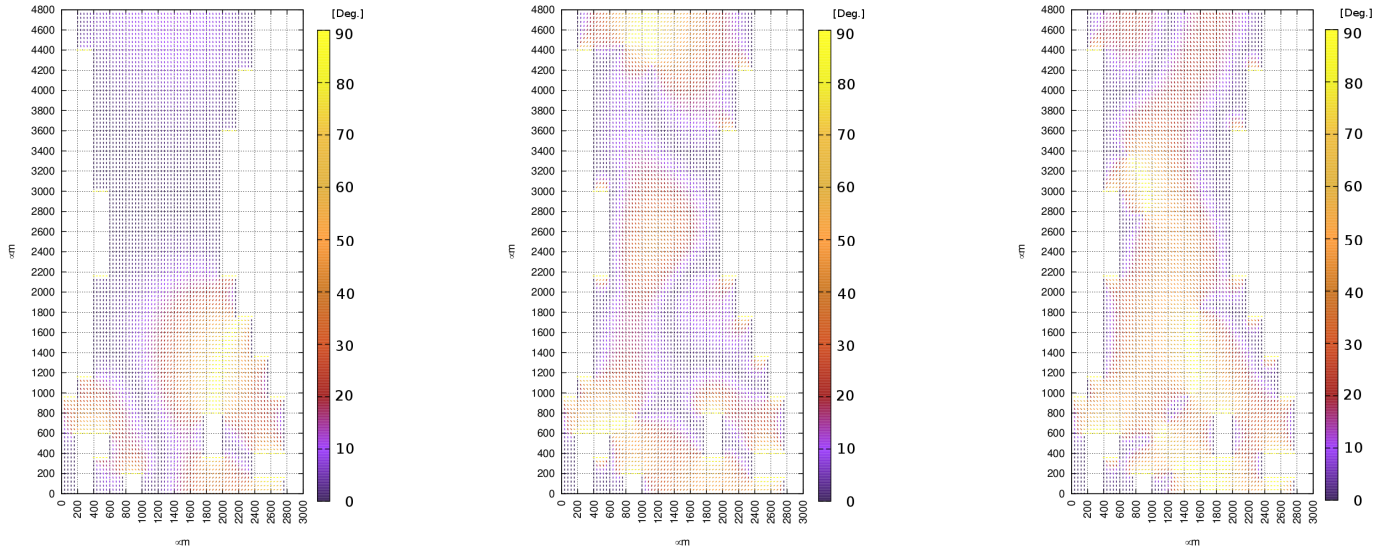

(a) Cutoff range = $90\mu m$ (b) Cutoff range = $60\mu m$ (c) Cutoff range = $45\mu m$

Figure 28: Results of simulations with fixed orientation of cells along the longest edge (y axis) and around the tethering points. Results were obtained after about 30×10^6 iteration. The dark blue colour denotes cells parallel to the longest axis of the tissue (0°), while yellow denotes cells perpendicular to the longest axis of the tissue (90°).

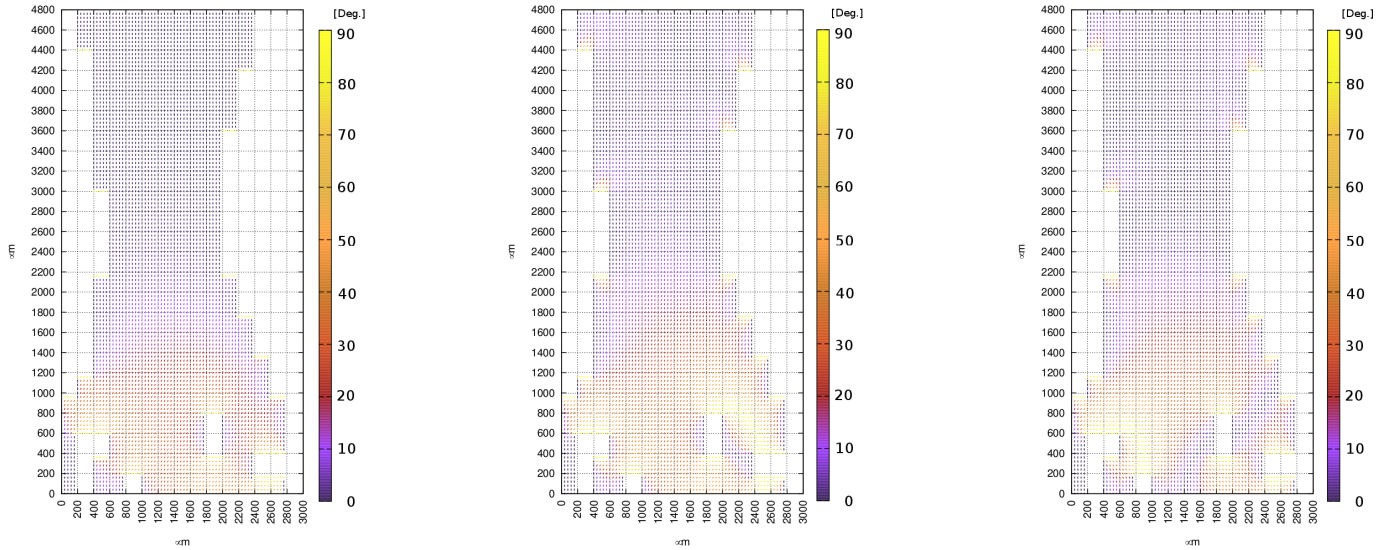

(a) Cutoff range = $90\mu m$ (b) Cutoff range = $60\mu m$ (c) Cutoff range = $45\mu m$

Figure 29: As figure 26, but with results obtained after about 30×10^7 iteration.

5.2 Advanced model - results

In this section we present results from the more advanced Hamiltonian (Eq. 27). The section starts by examining the convergence properties of the annealing algorithm, before discussing the effects of changing the parameters of the model and the introduction of noise. In all results presented in this chapter, simulations start from a regular, rectangular square matrix of cells, where sticks have density 2.5×10^{-3} *cells per* μm^2. In the Hamiltonian (Eq. 27) the k constant is always equal to 1 and expressed $[N/\mu m]$.

5.2.1 Convergence of the annealing algorithm

The main purpose of the chapter is to examine the convergence properties of the annealing algorithm. Figure 30 presents different stages of annealing process. To generate the results, the following parameters were used: T_0 equal to 527 pJ, T_f equal to 10^{-10} pJ, $l = 20$ μm, $\Delta L = 15$ μm. The simulations presented in Fig. 30 and 31 consists of respectively 527 and 1830 cells.

The shortest anneal time is denoted as t_0 in Fig. 30a and corresponds to about 30×10^6 iterations. Convergence is reached with increase of the annealing time, moreover the modelled tissue is wider at the edges and thinner in the central region similar to the experiment. The ratio of thicknesses between these regions depends on the constant Δl in the Hamiltonian. Fig. 30a does not show aligned orientation in the whole tissue, in particular, there are random orientation of cells in the centre and at the edges of the delta regions.

Even with increasing annealing time, as shown in figure 30b, lack of alignment still occurs between the vertical cell chains. On the other hand there is lack of explicit disorder between cells, moreover tissue in the narrowest part is 18.03% thinner than in Fig. 30a

Figure 30c presents results of the annealing time $100t_0$, where cells form a mostly

aligned structure, but the positions of whole chains of cells have not reached the optimal structure. Figure 30d shows a fully annealed, symmetrical system with axis of symmetry almost parallel to the longest axis of the graph. In comparison to the previously presented stages of annealing, chains are ordered and the tissue is 11.48% thinner than in the shortest anneal time presented in Figure 30a.

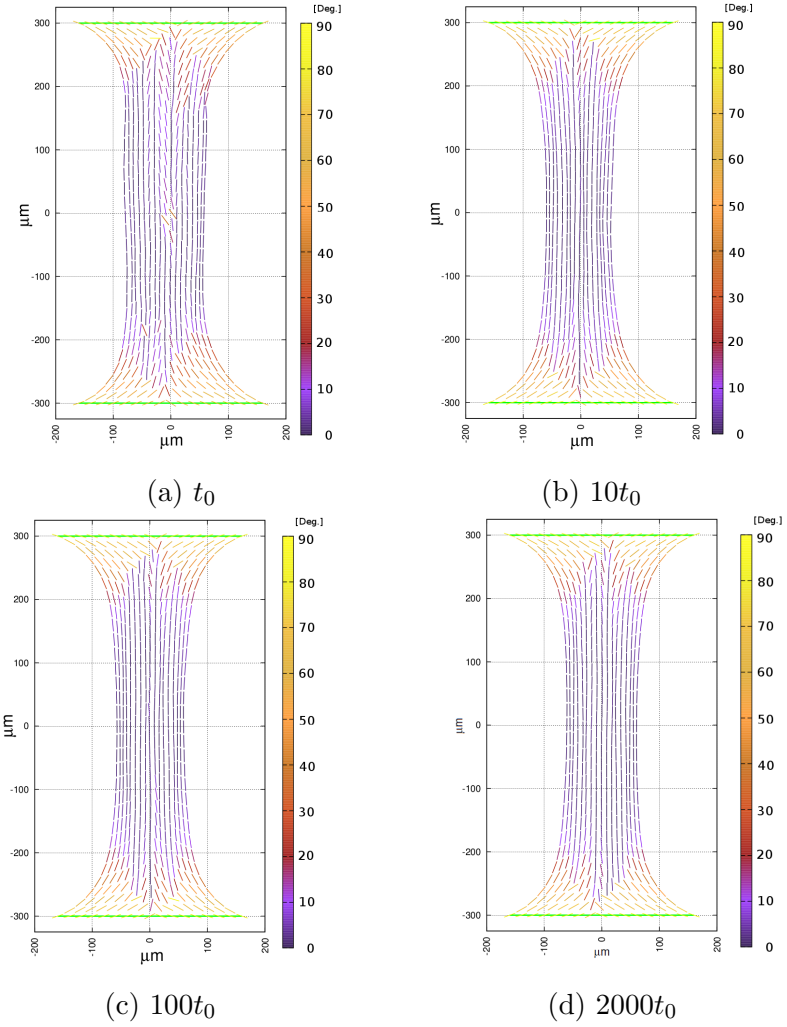

(a) t_0 (b) $10t_0$

(c) $100t_0$ (d) $2000t_0$

Figure 30: The lowest energy solution identified of a system consisting of 527 cells. Interactions are described by the Hamiltonian in Equation 27. The panels present four stages of the annealing process, t_0 denotes the shortest anneal time used here, equal to about 30×10^6 iterations. Initial grid has size $600 \times 300[\mu m]$. The *cell contraction length*, Δl is equal to 15.0 μm. The position of cells along the green line is fixed. The dark blue colour denotes cells parallel to the longest axis of the tissue (0°), while yellow denotes cells perpendicular to the longest axis of the tissue (90°).

A similar analysis of convergence is presented in figure 31, panels are ordered according to increasing anneal time. The main difference is connected to the initial grid size $1200 \times 600[\mu m]$. As with results obtained for a smaller grid, time t_0 denotes the same number of iterations (about 30×10^6) as used in figure 30a. We can observe that the shortest annealing time (figure 31a) is not sufficient to obtain convergence of computation. In figure 31a chains of cells show lack of alignment across the whole area of the tissue. Moreover the simulated tissue is not regularly narrowed and there is no axis of symmetry.

Panel 31b presents results for annealing time $10t_0$. The main visible difference is the mostly aligned chains of cells. On the other hand, chains of cells are unnaturally squeezed in the central part of the tissue, and the ratio of the thinner region to the initial grid width is equal to 62.56%. A significant lack of alignment occurs in the delta regions, where many cells show a strong perpendicular arrangement to the longest axis. In a similar manner to results obtained for a smaller grid, figures 31a and 31b show a lack of alignment between chains of cells. This is especially visible in the distances between outermost chains of cells and their arrangement along the y axis of the tissue. In figure 31c, cells in the delta regions have a more organized arrangement and chains of cells are aligned. Similar to the previous graph, chains of cells at the edges of the tissue are squeezed towards the centre of the sample. The width ratio is equal to 76.0%. Figure (31d) represents the fully annealed system, where the ratio between the narrowest part of the tissue and cells along the green line is equal to 74.61%. In figure 31d the asymmetry in the orientations is probably natural effect generated by the algorithm, as it finds the most aligned structure. It is possible that the most alignment structure has no symmetry about the midplane. On the other hand the modelled tissue may be not fully annealed.

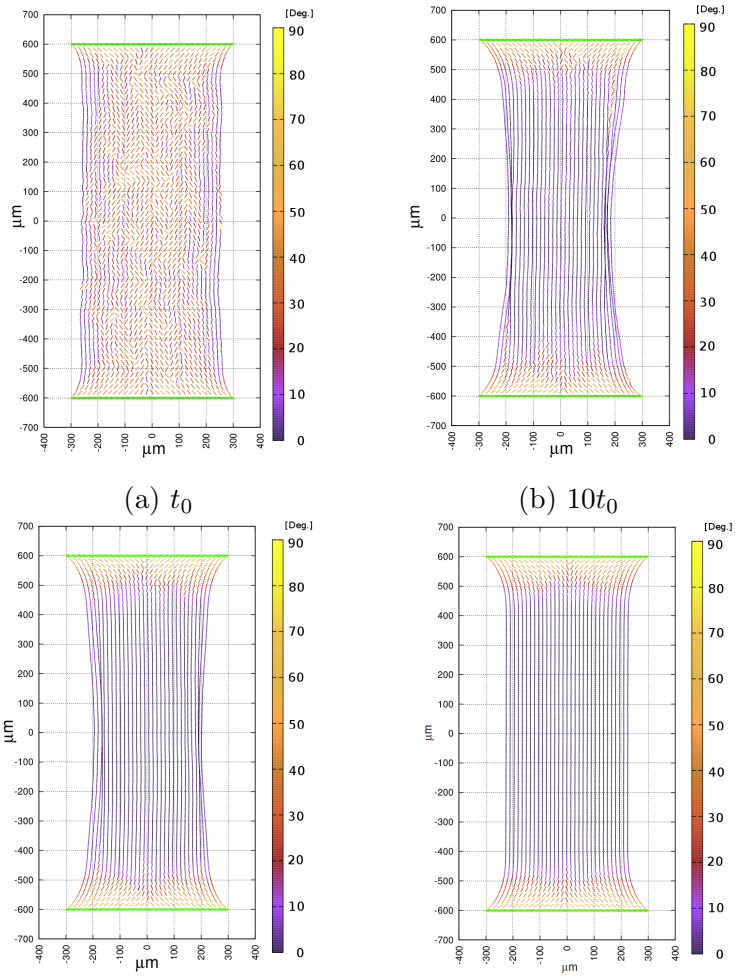

(a) t_0 (b) $10t_0$

(c) $100t_0$ (d) $2000t_0$

Figure 31: The lowest energy solution identified of the system during annealing process. The system consists of 1830 cells and interactions are described in equation 27. t_0 denotes the shortest anneal time presented here, equal to about 30×10^6 iterations. Initial grid has $1200x600[\mu m]$. *Cell contraction length* (Δl) is equal to $5.0[\mu m]$. Position of cells along the green line is fixed. The dark blue colour denotes cells parallel to the longest axis of the tissue (0°), while yellow denotes cells perpendicular to the longest axis of the tissue (90°).

5.3 Straight tether

Figures 32, 33 present simulations with 527 cells and grid size $600 \times 300[\mu m]$. To generate the results presented in the Figs. 32, 33, 34 and 35 the following parameters were used: T_f equal to 10^{-10} pJ, l equal to 20 μm, Δl is varied. To obtain the fully annealed a configuration 60×10^9 iterations were executed.

Charts included in the first figure (32a and 32b) have different *cell contraction length* constant respectively: 0.5 and 1.0 $[\mu m]$. We can see that the simulated tissues have different shapes. With increasing *cell contraction length* the shape is narrower towards the middle of the sample. Only the first row of the cells have orientation which is not parallel to the long axis of the tissue. The rest of the chains are ordered almost parallel to each other. More detailed examination of figures 32a and 32b shows a disruption of symmetry in the cell orientation which is especially visible near the green lines representing the tethers: a few cells at one edge of the sample do not have the same angles as cells on the other edge. The first rows of cells do not turn smoothly into aligned chains of cells.

In figure 33 simulated tissue samples for *cell contraction length* parameters equal to 5 and 15 μm respectively are shown in panels 33a and 33b. It is possible to see small delta regions when *cell contraction length* is equal to 5.0 μm. The first three, unfixed rows of cells have significantly different orientation to the rest of the tissue, moreover chains of cells in the centre of the sample have an aligned arrangement. With increase in the *cell contraction length*, tissue becomes more squeezed and delta like regions can be seen in figure 33b, where Δl is equal to 15 μm. The figure shows a characteristic double delta region, where two main groups of cells with different orientation are distinguished. The first group of cells is in the middle, where cells are parallel to the longest axis. Whereas the second group is around the edges and cells have a more perpendicular orientation to the long axis. Between the edges of the

simulated sample and the middle of the tissue there is a transition region, where cells smoothly change orientation from perpendicular to parallel to the y axis.

In figures 33a and 33b close to the tether a narrowing can be seen in the middle regions of the tissue, which have a width in the narrowest part of about 77.5% and 64.0% of the initial grid width, respectively.

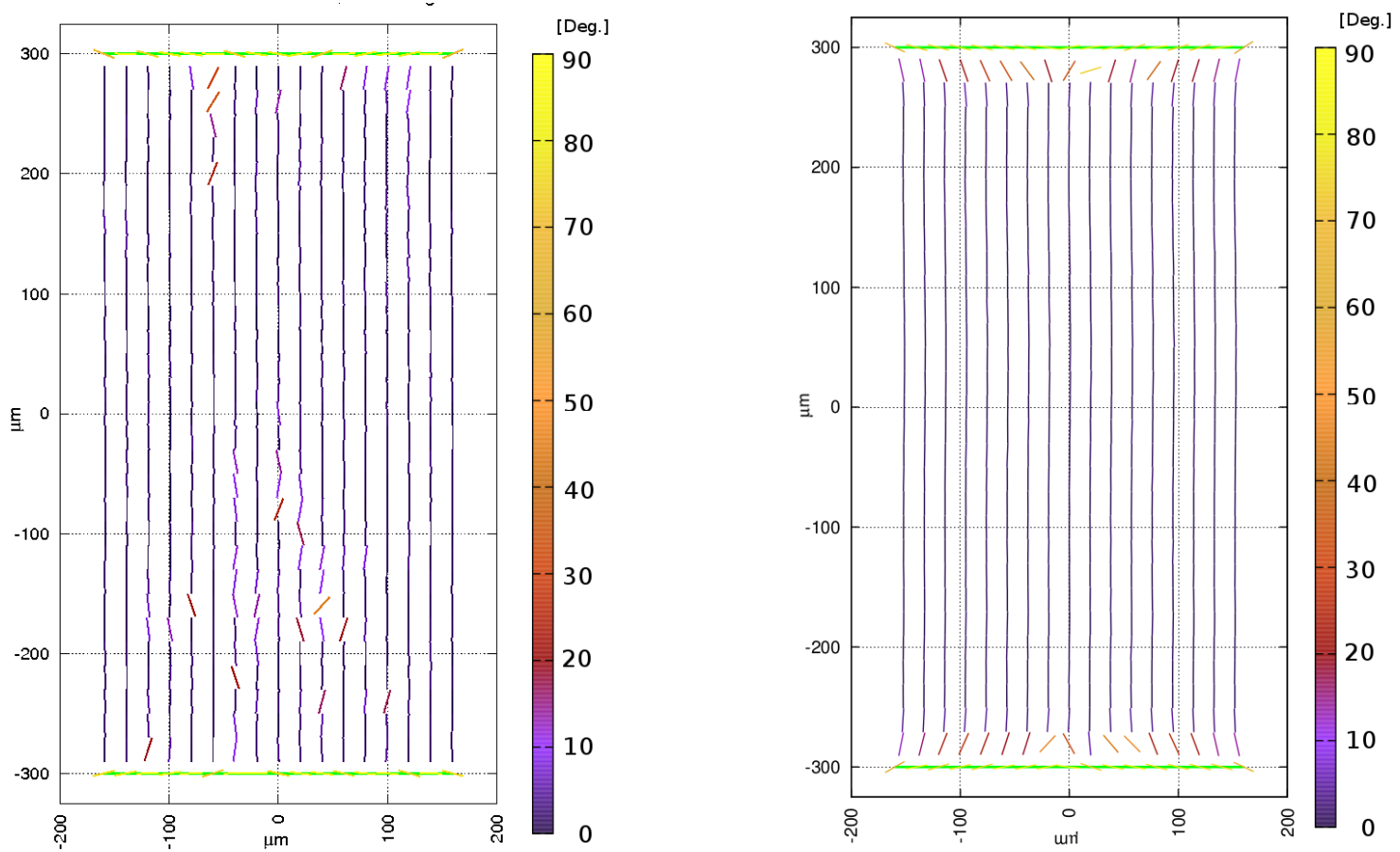

(a) $\Delta l = 0.1\ \mu m$

(b) $\Delta l = 1.0\ \mu m$

Figure 32: The lowest energy solution identified of a system, consisting of 527 cells. Interactions are described in Eq. 27. The initial grid is $600 \times 300[\mu m]$. Data were obtained for different values of the *cell contraction length*. The position of cells along the green line is fixed. The dark blue colour denotes cells parallel to the longest axis of the tissue (0°), while yellow denotes cells perpendicular to the longest axis of the tissue (90°).

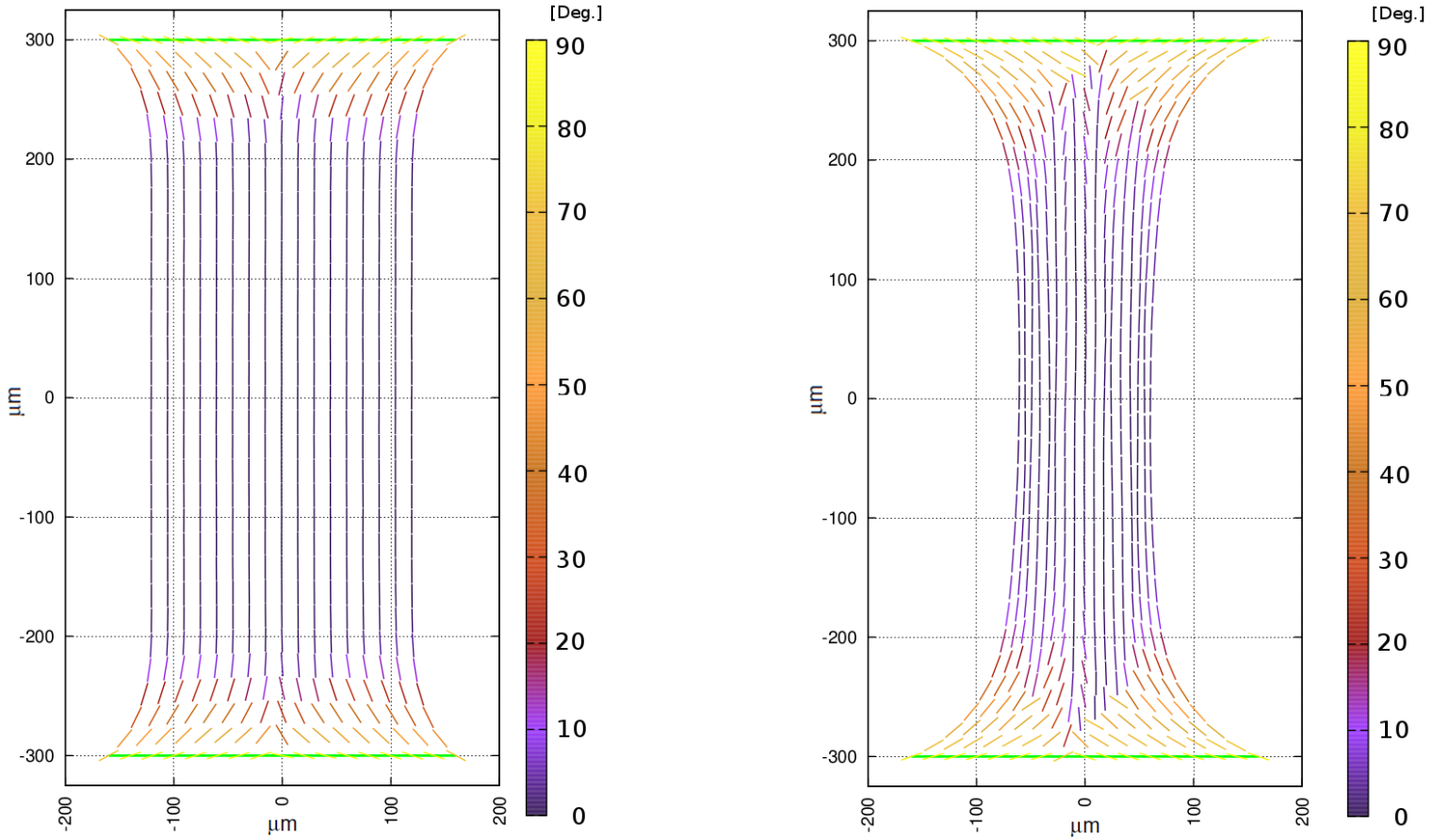

(a) $\Delta l = 5.0\ \mu m$

(b) $\Delta l = 15.0\ \mu m$

Figure 33: As Figure 32, but with *cell contraction length* equal to 5.0 and 15.0 [μm].

Figures 34 and 35 present results of similar simulation to those presented before (figures 32, 33). To generate the results presented in Figs. 34 and 35 the following parameters were used: T_0 respectively equal to 1830 $[pJ]$, T_f equal to 10^{-10} $[pJ]$, $l = 20$ $[\mu m]$, ΔL is varied. In this case results are presented for a larger grid of $1200 \times 600 [\mu m]$, which includes 1830 sticks. To obtain results 60×10^9 iterations were executed.

Figure 34a shows results from simulated annealing of the Hamiltonian for the smallest *cell contraction length* constant presented here equal to 0.1 $[\mu m]$. As we can see the structure does not have good alignment. Many cells have random orientation and the simulated tissue has not got an axis of symmetry at all. On the other hand chains of cells are roughly parallel to each other both in the middle of the sample and close to the clamped regions, where characteristic delta regions would occur. Some similarities are visible between results for small and medium grid size when *cell contraction length* 0.1 $[\mu m]$ (figures 32a and 34a), as cells are insignificantly squeezed together in the middle the tissue and chains of cells do not form an aligned structure.

In figure 34b, *cell contraction length* is equal to 1.0 $[\mu m]$. The cells are aligned, chains show a parallel arrangement and in the narrowest part the maximum change of cells position is about 10 $[\mu m]$ compared to their position at the start of the simulation. Moreover the two first rows of cells close to the green lines (representing tethering points) have an orientation which is not parallel to the longest axis of the tissue. Comparing graphs 32b and 34b, we can see a similar almost unsqueezed structure of the simulated tissue and a lack of characteristic delta regions, when small *cell contraction length* is applied.

Figures 35a and 35b have the same initial spacing of the grid, as previously, whereas cells have different *cell contraction lengths* respectively 5.0 and 15.0 $[\mu m]$. On increase of Δl, cells become more and more contracted towards the centre of the tissue. In figure 35a the cells in the first row are slightly offset from the y axis. More explicit delta

regions are visible in figure 35b, especially cells in the first row away from the tethering points. On the other hand the orientation of cells in the middle chain is parallel to the longest axis of the tissue. When *cell contraction length* is equal to 15.0[μm] then some of cells have moved about 150 [μm] in the narrowest part of the sample relative to their original positions.

Comparison between simulations with the same *cell contraction length* constants and different sizes of the grids shows relatively larger and more explicit delta regions in the simulation with the bigger grid. The size of the regions in the graph changes according to the ratio of the grid. Moreover tissues seems to be symmetric in both cases. A similar trend in delta regions can be seen on comparison between graphs 33b and 35b, when *cell contraction length* is equal to 15, although we note that tissues do not have a perfect axis of symmetry, as chains of cells in the middle of the tissue have slightly different cell arrangements at the top and the bottom of the model.

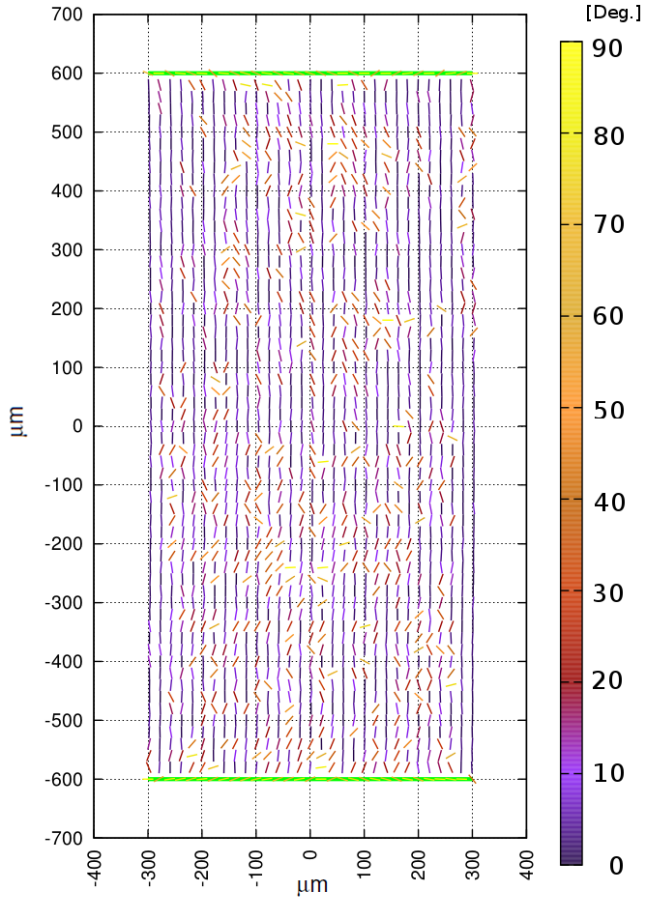

(a) $\Delta l = 0.1\ \mu m$

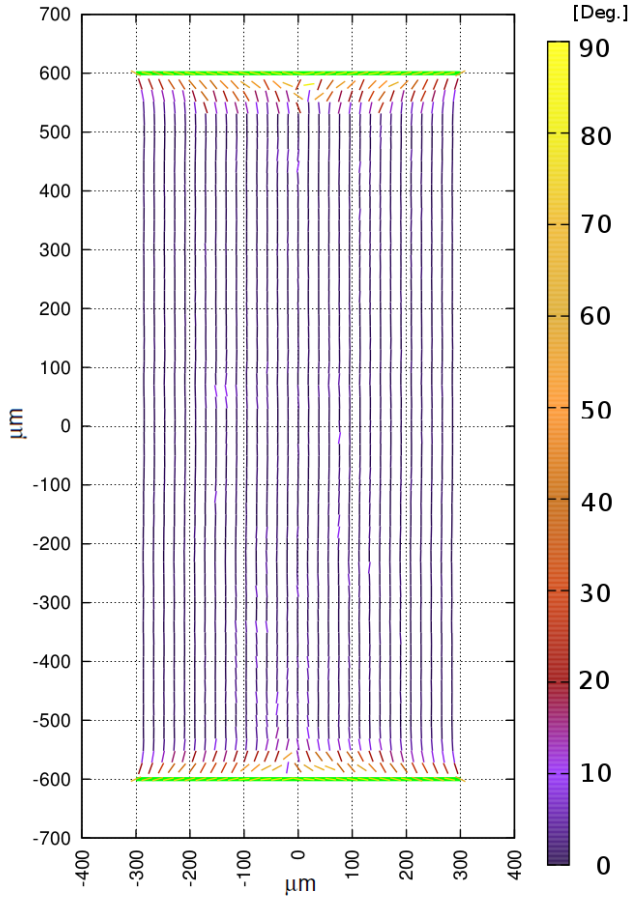

(b) $\Delta l = 1.0\ \mu m$

Figure 34: Results for a system which consists of 1830 cells. Interactions are described by the Hamiltonian in Eq. 27. The initial grid has dimension of $1200 \times 600[\mu m]$. Data were obtained for different *cell contraction lengths*. Position of cells along the green line is fixed, representing the tether. The dark blue colour denotes cells parallel to the longest axis of the tissue (0°), while yellow denotes cells perpendicular to the longest axis of the tissue (90°).

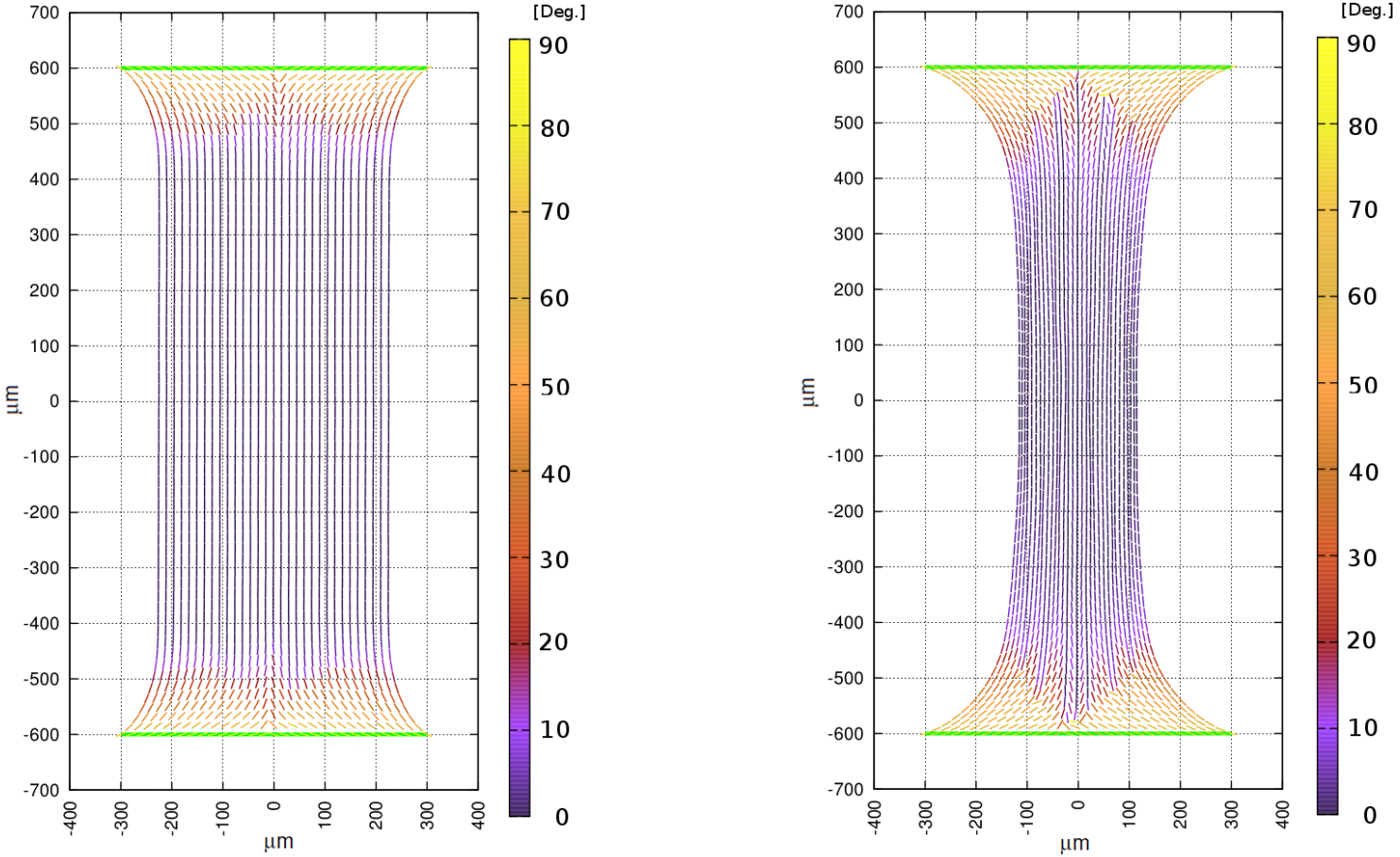

(a) $\Delta l = 5.0\ \mu m$

(b) $\Delta l = 15.0\ \mu m$

Figure 35: As Fig. 34, but with *cell contraction length* equal to 5.0 and 15 respectively.

5.3.1 Four point tether

So far all results were concerned with computation of two dimensional planes with cells tethered along the whole shorter edge. In contrast the results described below have different boundary conditions. Cell positions were fixed only at the four points in the corners denoted with green dots in Figures 36 and 37. To generate the results presented in Figs. 36 and 37 the following parameters were used: T_0 equal to 527 $[pJ]$, T_f equal to 10^{-10} $[pJ]$, $l = 20$ $[\mu m]$, Δl equal to 5 $[\mu m]$. To fully anneal the model about 60×10^9 of iterations were executed.

In the first set of results panels are ordered according increasing annealing time. Figure 36a, with the shortest annealing time t_0, shows a totally disordered structure of the cells in the middle of the simulated tissue and some alignment in the outer rows of cells. The second annealing time $10t_0$ in figure 36b also shows totally disordered structure in the centre of the graph. On the other hand, the two outmost rows of the cells are in alignment. When annealing time increases (Fig. 36c) more rows of tissues show ordered structure. In the final image there is almost total alignment in the center (Fig. 36d).

It is worth noting that figures 30d and 36d have the same annealing time and size of the initial grid equal to $600 \times 300[\mu m]$, but when the cells are tethered only at four points then the structure is not fully annealed for the largest anneal time presented here. This is surprising because the comparison between figures 31d and 36d shows that simulation with a longer annealing time is sufficient when cells are tethered along the whole edge, even when the grid is four times bigger than in the figure 36d. The time required to obtain the global minimum is too long for our computing cluster.

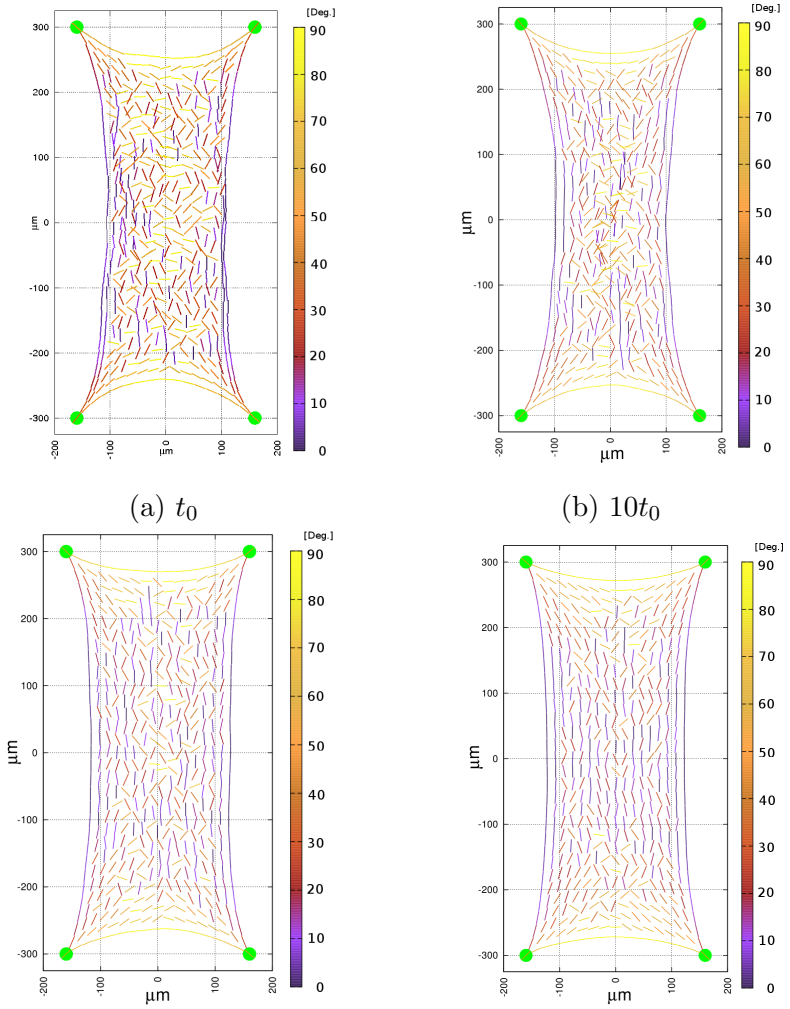

(a) t_0 (b) $10t_0$

(c) $10^2 t_0$ (d) $2 \times 10^3 t_0$

Figure 36: Simulated annealing results for a system, which consists of 527 cells, obtained after about 60×10^9 iterations for equation 27. Every panel presents simulations with different annealing time, where t_0 denotes the shortest time presented here. Initial grid has dimension of $600 \times 300[\mu m]$ and the *cell contraction length* constant is equal to 5.0. Position of cells at the green points is fixed. The dark blue colour denotes cells parallel to the longest axis of the tissue (0°), while yellow denotes cells perpendicular to the longest axis of the tissue (90°).

Figures 37a and 37b present systems of cells tethered in the corners, with different values of *cell contraction length*. Figure 37a where $\Delta l = 1$ $[\mu m]$ shows strong disorder in the centre, and weak alignment in the external chains. The whole simulated tissue is squeezed to the centre, specifically cells contract both along x and y axes. Tissue in the narrowest part has dimensions of about 85% in x and 76% y direction of the initial length of tissue.

In figure 37b corresponding to the larger *cell contraction length* constant, a more orderly arrangement is observed. Chains of cells are aligned in the outer parts of the tissue but in the middle of the sample a few cells still have random orientation. In figure 37b an explicit change can be seen in the middle region of the tissue, which has a width in the narrowest part of about 73.0% in x and 90.14% in x direction as compared to the initial configuration.

As can be noted in Fig. 37a and 37b the increase of Δl, squeezes the tissues more significantly. In both figures, the annealing time was insufficient for convergence, although in figure 37b the tissue is better annealed.

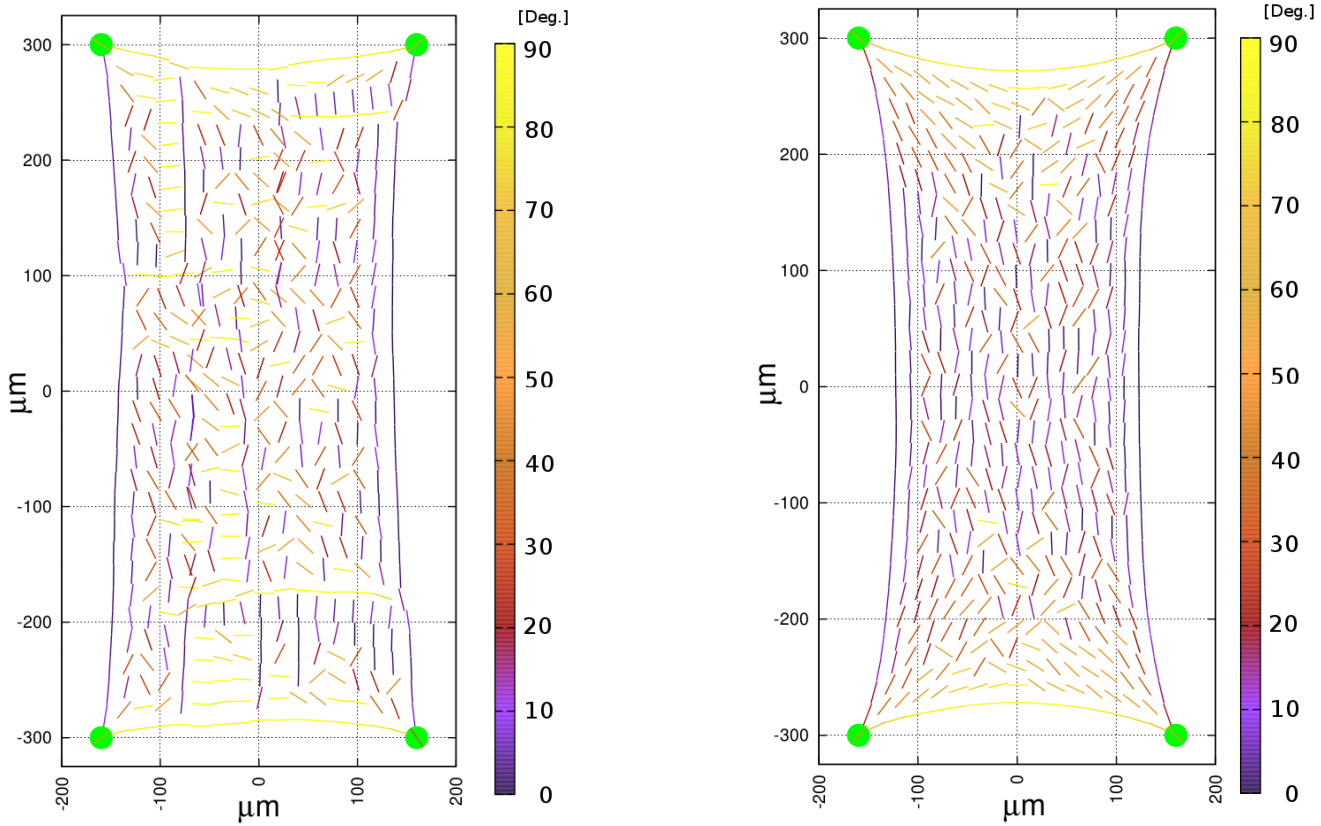

(a) $\Delta l = 1.0\ \mu m$

(b) $\Delta l = 5.0\ \mu m$

Figure 37: Results for a system of 527 cells, with interactions described by Eq. 27. Initial grid has size $600x300[\mu m]$. In the cost function the *cell contraction length* constant is equal 1.0 and 5.0 $[\mu m]$ in panels (a) and (b) respectively. Position of cells marked by the green dots are fixed. The dark blue colour denotes cells parallel to the longest axis of the tissue (0°), while yellow denotes cells perpendicular to the longest axis of the tissue (90°).

5.4 Introduction of noise

Models of the tissue with an additional noise parameter are presented for both types of tethering. Specifically, the constant l described in the Hamiltonian is equal to $20 + n$ $[\mu m]$ and n is a random number in the range $[-n, n]$ $[\mu m]$ which represents noise parameter. It is worth repeating that during updates the algorithm only needs l between the chosen cell and nearest neighbours.

Figure 38 shows results for the *cell contraction length* Δl constant equal to $5[\mu m]$ and boundary conditions fixed along the shorter edge of the tissue. Figure 38a has n is equal to 1 $[\mu m]$. Just like in the figure without noise the delta regions are visible and chains of cells are mostly parallel to each other.

Comparison with Fig. 34 shows that there is a small increase of deflection distance for n is equal to 5 $[\mu m]$ shown in figure 38b. Moreover delta regions have increasing numbers of cells almost perpendicular to the longest axis of the tissue.

Figure 38c shows a locally disordered structure with a visibly different arrangement of cell sticks in the delta regions. The parameter n is equal to 10 $[\mu m]$. The initial number of chains of cells diminishes. Moreover, many cells show disorder in the central region of the tissue.

In figures 38a, 38b and 38c in the narrowest region, the ratio of width to initial length is about 74.44%, 68.42% and 67.67%, respectively. It is important to note that the ratio in the same configuration of modelled tissue without noise parameter (figure 33a) is equal to 80.45% of initial length. Thus with increasing noise parameter the ratio is smaller.

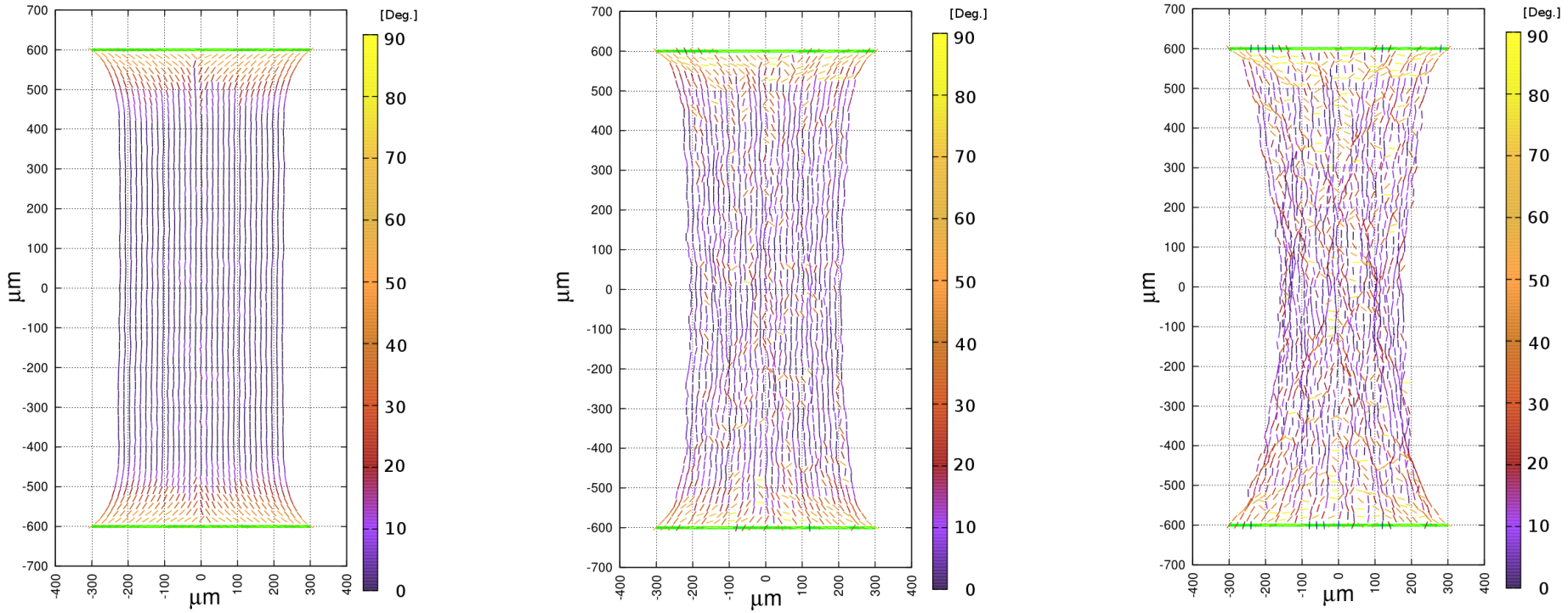

(a) $n \in [-1.0; 1.0]$ μm (b) $n \in [-5.0; 5.0]$ μm (c) $n \in [-10.0; 10.0]$ μm

Figure 38: Results from simulations consisting of 1830 cells, obtained after about 60×10^9 iterations for the Hamiltonian in Eq. 27. Every result was obtained for the same l constant equal to 20.0 $[\mu m]$ with different noise parameter. The initial grid was $1200 \times 600[\mu m]$. In the cost function *cell contraction length* constant is equal to 5.0 $[\mu m]$. Position of cells along the green line is fixed. The dark blue colour denotes cells parallel to the longest axis of the tissue (0°), while yellow denotes cells perpendicular to the longest axis of the tissue (90°).

We also consider the effects of noise for a 4 point tethering. Figure 39 presents results for noise n increasing: (n varies by 1.0, 5.0 and 10.0 μm respectively in figures 39a, 39b and 39c). These should be compared to Fig. 37a, where noise is not applied.

In figure 39a, where n varies by 1.0 μm, cells are slightly deflected from their position in figure 36d. In figure 37b, cells have a distinct perpendicular arrangement in the delta regions.

Corresponding to the increase of the noise constant, more significant deflection is shown in figure 39b. Similarly to figure 38c, the most visible change occurs when parameter n has the highest value. Cells create new chains and significantly change positions and have new nearest neighbours.

Vertical orientation in delta by regions occurs frequently in figures 39b and 39c, where a several cells change orientation about 90 degrees.

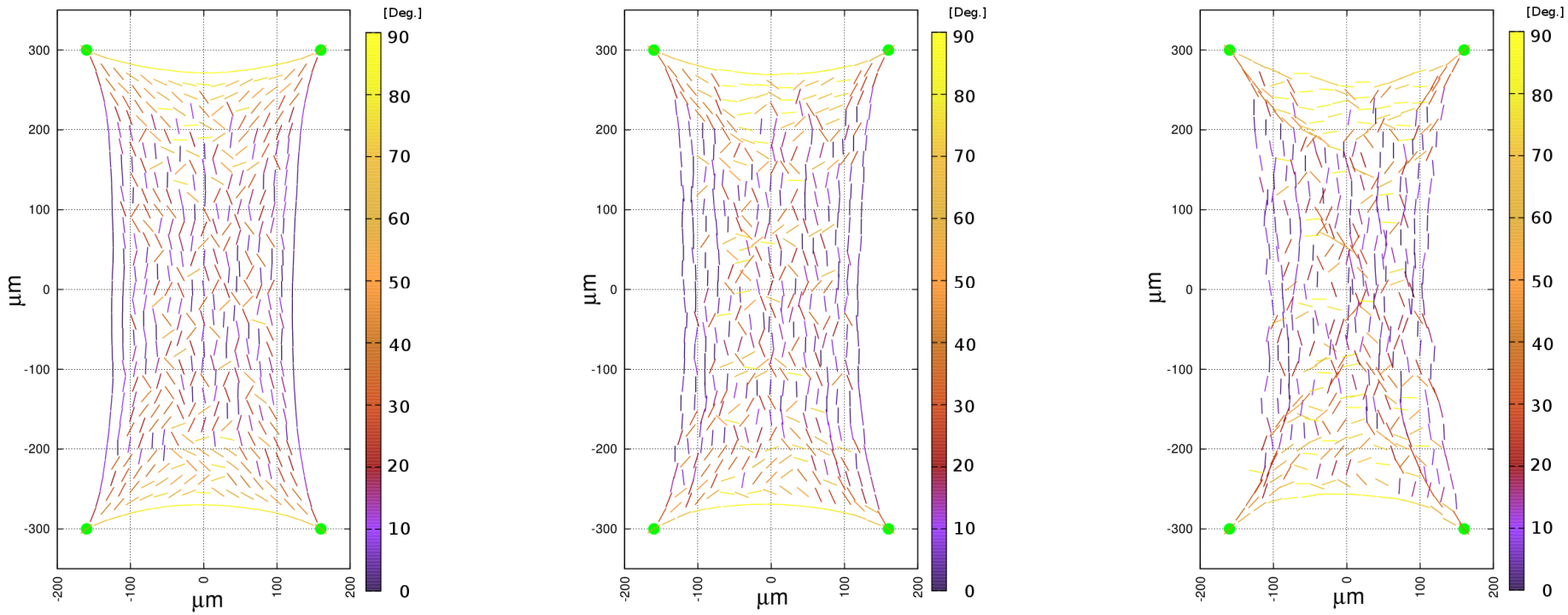

(a) $n \in [-1.0; 1.0]$ μm (b) $n \in [-5.0; 5.0]$ μm (c) $n \in [-10.0; 10.0]$ μm

Figure 39: Results from simulations consisting of 527 cells, arrangement obtained after about 60×10^9 iterations. Every panel has constant $l = 20.0$ μm with different noise parameters. Initial grid has size $1200x600[\mu m]$. In the cost function *cell contraction length* constant is equal 5.0 μm. Position of cells marked by the green dots is fixed. The dark blue colour denotes cells parallel to the longest axis of the tissue (0°), while yellow denotes cells perpendicular to the longest axis of the tissue (90°).

5.5 Model of engineered neural tissue

Finally, models of tissue are presented with the same type of tether points as in the engineered neural tissue (section 4). The tethers points have circular shape with radius equal to 40 μm. The initial grid has a rectangle shape with dimensions 620×800 [μm]. There are four, circular tethers at the edges of the mould. The ratio of tissue length in x and y directions and tether points position is the same as in the engineered neural tissue. To generate the results presented in 40 the following parameters were used: T_0 equal to 3000 pJ, T_f equal to 10^{-10} pJ. To anneal about 60×10^9 iterations were executed. The constant l is equal to 20 μm and *cell contraction length* constant is equal to 1.0, 10.0 and 15.0 μm, respectively in figures 40a, 40b and 40c.

In Figs. 40a, 40b and 40c convergence is not fully reached and outer chains of cells show strong disorder and lack of alignment. Moreover in the outmost region the volume collapses between cells. In all figures, there are significant delta regions at the edges, but in figure 40a only a few rows of cells near tether points, toward the lower centre of the tissue have a perpendicular direction to the y axis and form single delta regions. Whereas in figures 40b and 40c cells, which form delta regions, smoothly change orientation toward the centre of the tissue.

In figure 40a, there are a few cells in the centre of the graph which are not aligned. The middle region of the tissue is slightly thinner than around tethering points at the edges.

Similarly to sets of figures 32-35, showing increased *cell contraction length* constant, the cells squeeze towards the centre of the tissue. The process is visible in the panels 40b and 40c, the thickness of the tissue in the narrowest part of tissue to the length around tether points is equal respectively to 60% and 47%. Moreover in both graphs cells squeeze towards the centre of the tissue between tether points.

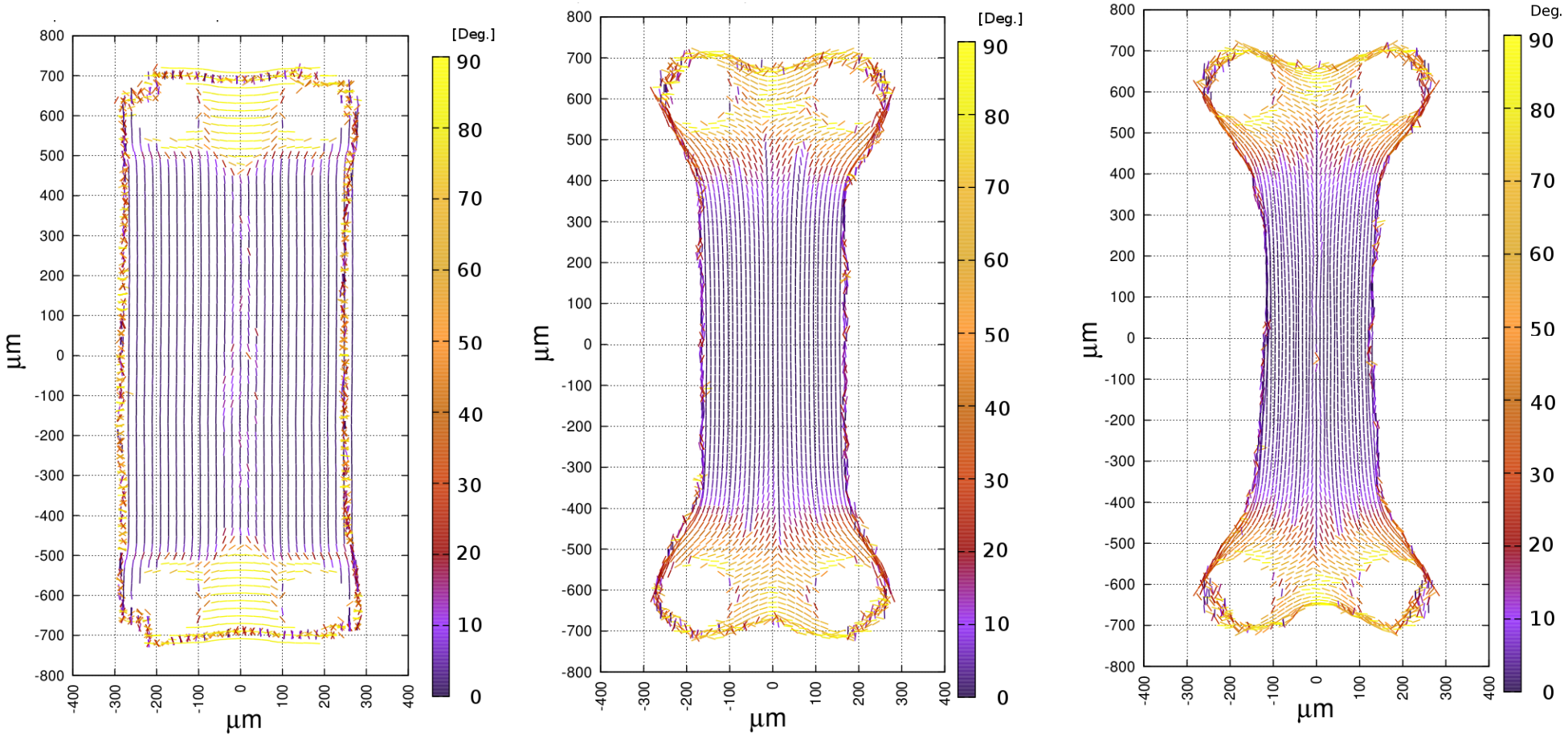

(a) $\Delta l = 1.0\ \mu m$ (b) $\Delta l = 10.0\ \mu m$ (c) $\Delta l = 15.0\ \mu m$

Figure 40: Results from simulations, after about 60×10^9 iterations. The system consists of 3000 cells. Initial grid has size $1600x800[\mu m]$. *Cell contraction length* constant is equal 5.0 μm. The dark blue colour denotes cells parallel to the longest axis of the tissue (0°), while yellow denotes cells perpendicular to the longest axis of the tissue (90°).

5.5.1 Comparison of model with experiment

Figures 41 and 42 shows comparison of models of engineered neural tissue with the experimental cells orientations (from figure 22).

The process of comparison between tissues is complex and can be divided into a few parts. Sizes of the model and engineered neural tissue are different. Firstly, the program scales the size of engineered neural tissue to the size of the model. Next, histograms of cells orientations of the model and ENT are created. Histogram of cell orientations of modelled tissue and ENT (with size scaled to the modelled tissue) are presented in Fig. 41. Every square presented in Fig. 41 has the same size, but the number of cells is different in experimental and modelled histograms. In order to compare histograms, it is essential to normalize them. Every bin of the histogram includes the number of cells within a defined range of angles, which is included in the area (in Fig. 41 the area is equal to 100×100 $[\mu m]$). Every square in Fig. 42 represents the value of a residual, which is obtained using in Eq. 29.

$$R = \sum_{i=0}^{n_b} \left| \frac{(N'_{\alpha_e,i} - N'_{\alpha_m,i})}{(N'_{\alpha_e,i})} \right|, \tag{29}$$

where R is the residual, n_b denotes number of bins in the histogram, $N'_{\alpha_e,i}$ and $N'_{\alpha_m,i}$ are standardized numbers of cells included within each bin in experimental and modelled tissue, respectively and they are defined below.

$$N'_{\alpha_{e,i}} = \frac{N_{\alpha_{e,i}}}{\sum_{j=0}^{N} N_{\alpha_{e,j}}}$$

$$N'_{\alpha_{m,i}} = \frac{N_{\alpha_{m,i}}}{\sum_{j=0}^{N} N_{\alpha_{m,j}}}$$

N is the total number of bins and $N_{\alpha_{e,i}}$ and $N_{\alpha_{m,i}}$ are the numbers of cells included within each bin in experimental and modelled tissue, respectively.

The minimum possible value obtained in presented way is equal to 0, whereas maximum value can vary. When the value is smaller it means that the degree of matching is higher. Unfortunately, our comparison does not show precise information about the degree of matching between corresponding bins of the histograms. The method obtains only rough information about the comparison of whole histograms.

Figure 42 presents comparison between the model shown in 40c and ENT. The fields in the delta regions are denoted by blue colours and white colours. This means that the degree of matching is highest, as the corresponding number is close to 0. There are a few yellow squares at the edges of the top region and at the middle of bottom region, near places with the tethers. On the right hand site of the tissue there are orange and red colours corresponding to number 4, denoting the lowest degree of matching. Moreover, regions without cells are denoted by grey fields. There are many grey fields on the left and right edges of the tissue.

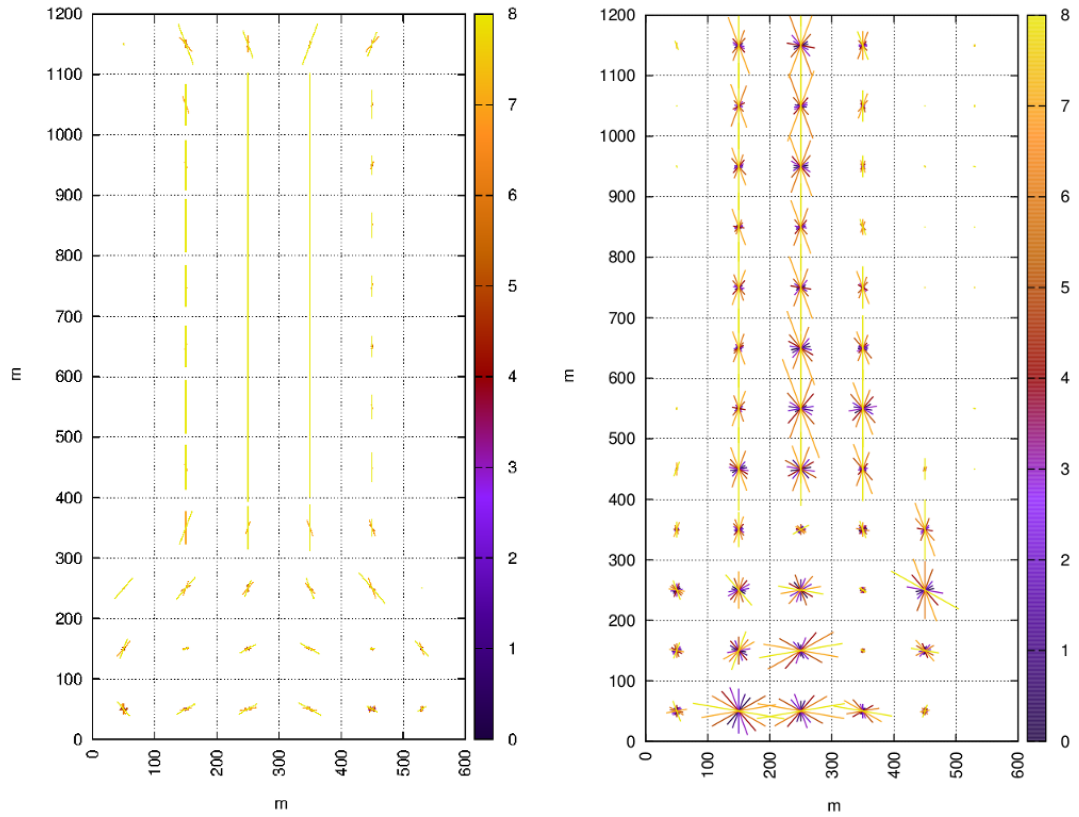

(a) HCO of modelled tissue

(b) HCO of ENT

Figure 41: Histograms of cells orientations (HCO) of: 41a modelled and 41b engineered neural tissue. The tissue was modelled with $\Delta l = 15\ \mu m$ (Unscaled model presented in Fig. 40c). ENT is presented in Fig 19.

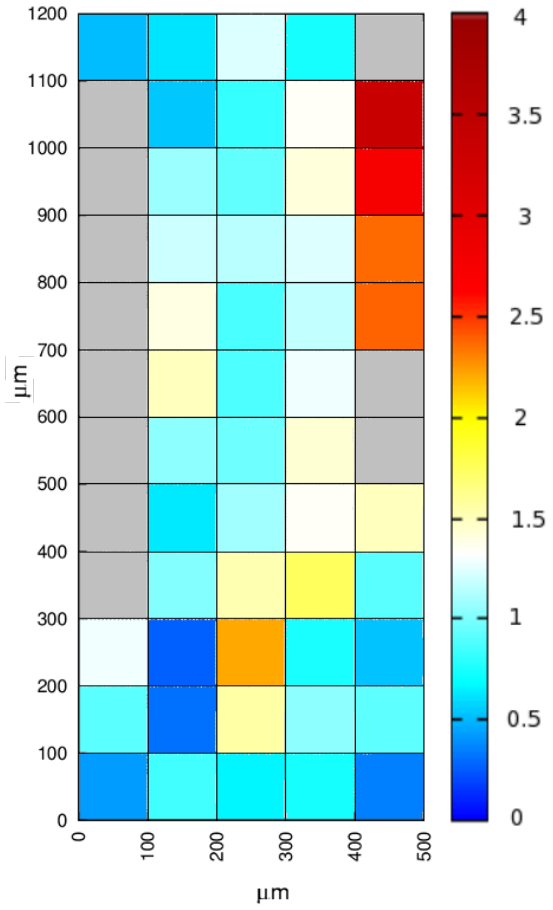

Figure 42: Comparison of the modelled tissues (presented in figure 40c with $\Delta l = 15$ $[\mu m]$) and histogram of cells presented in figure 22. The legend describes the degree of matching between corresponding histograms. The red colour denoted by number 4.0 represents the biggest differences between histograms, whereas dark blue colour denoted by number 0 denotes the highest degree of matching. The scale is relative and gives only rough idea about the degree of matching. The grey colour denotes a lack of cells in the square.

6 Conclusions and further work

This thesis aims to describe the behaviour and interaction of cells in engineered neural tissue. Understanding the behaviour of cells within tissue is important for further investigation of engineered neural tissue. For the physicist, it is important to improve the Hamiltonian, so that it can more precisely predict the shape and orientation of experimental neural tissue.

6.1 Simple model

The simplified Hamiltonian in Eq. 26 was developed to give us an initial idea about behaviour of cells orientation in engineered neural tissue. In Eq. 26 interactions between cells are described by a $cos^2\alpha$ function. The position of cells is fixed, so the main aim is to show the relation between the orientation of cells around fixed regions and the number of near neighbours.

The results give us an idea about the number of neighbours that are necessary to obtain desired cell orientations. Moreover, the influence of tether points is visible at the top and at the bottom of the graphs.

Unfortunately, since cell locations are fixed, results generated using Eq. 26 cannot be applied directly the more advanced model, but can give us an idea of how a system made of many cells behaves when a simulated annealing algorithm is used.

Data presented in the experimental statistical distribution show that the cells should be oriented parallel to the long axis in the middle regions of the tissue. In the simulation it is visible that with increasing cut off range, more cells in the middle and delta regions start to orient parallel to the longest axis of the tissue. The cutoff range parameter is an important coefficient and allows us to cut the time of the annealing process. The fixed cells around tether points have a strong influence on the orientation of cells in

the delta regions. This indicates that tether points have a crucial role in determining the form of delta regions.

It is hard to assess the influence of neighbours in real tissue. During growth, real cells can change positions and interact with a different number of cells during the time needed to reach equilibrium.

In conclusion, range parameter is an important coefficient and allows us to cut time of the annealing process. While results cannot be applied directly to the more advanced model, the shape of tethers and numbers of neighbours are clearly important.

6.2 Convergence of the simulated annealing method

For the purpose of tissue engineering, the advanced model (Hamiltonian in Eq. 27) seems to be more accurate and helpful for understanding cell behaviour. When the more complex Hamiltonian is applied, the time needed to obtain results is much longer. To efficiently use computer power it is essential to find the shortest annealing time to achieve reasonable results.

When the longest annealing time is applied, chains seem to be fully ordered. It is worth noting that every panel presents the anneal time increased by a factor 10. We conclude that the configuration is close to the global minimum for $10^2 t_0$ anneal steps. A similar situation takes place when the system of cells is four times bigger and Δl is equal to $5.0 \mu m$. The algorithm needs more time to find the proper distance between the chains. Change of *cell contraction length* and increasing number of tethered cells can also change the required annealing time. Overall, it seems reasonable to conclude that the number of annealing steps needed to fully anneal the system presented here is around $10^3 t_0$.

6.3 Effect of parameters in the Hamiltonian

6.3.1 Squeezing parameter

When the term describing cell-cell interaction ($\Delta l(2 - cos^2\alpha_1 - cos^2\alpha_2)^2$) is multiplied by a constant Δl close to zero, then every change of cell orientation has insignificant effect on the whole energy. In this case, the first term of the Hamiltonian ($|\Delta r_{i,j}| - l$) essentially dominates the whole energy, so the orientation of cells can be random.

This suggests a minimum limit on Δl to show squeezing. It is concluded that a reasonable minimal Δl value to describe glial cells is between 1.0 and 5.0.

6.3.2 Tethering

One of the mains aim of the project is to find correlation between tethering points in the mould and cells positions and orientations. At this point, it is important to mention that the influence of the boundary conditions on the cell orientation is key factor to obtain a suitable arrangement of the cells.

When flat boundary conditions were applied, there is a correlation between squeezing and *cell contraction length*. It may be possible to find a function, which can describe the ratio between the narrowest part of the tissue and the widest edge.

On the other hand, there is a difference between the delta regions in experiments and those calculated with flat tethering points. The region of cells close to the ends of the sample can be described as 'double delta regions'. The shape of double delta regions is different than in ENT. The main difference is visible in the central part of the tissue along the y axis, where the cell angle is almost parallel to the longest axis of the tissue. The most visible effect of 'double delta regions' is in the simulations with high Δl constant. The artificial tissue in the experimental data described in the thesis was tethered at four points, but tether along shorter edge are also available [7]

and explicit delta regions are visible. In the model, cells orient parallel to the tension. It seems reasonable to conclude that tension in the x direction generated by the flat boundary conditions is not enough to create a triangular, single delta region.

In contrast, when four tether points were used during the simulation, then the orientations of cell in the delta regions was parallel to the shorter axis of the tissue. The cells moved towards the tissue centre and oriented perpendicularly to the y axis. We conclude that there is a greater tension along the shorter axis than in the y direction in the delta regions, so cells orient along the shorter axis and create explicit delta regions.

Further examination of the results describing tissue tethered at four points has potential to enable a good understanding of the ordering mechanism of the cells within a tissue sample. Cells squeeze to the centre of the tissue in x and y directions and cells align along the tension. Some similarities between tissue tethered by the circular tethering points and the simulation are visible.

To form delta regions cells change position along x and y direction and orient along the biggest tension. It is found that the algorithm has difficulties around the circular tethered regions, showing a volume collapse. In conclusion, agreement is quite good, the model on a square lattice does not include shear modulus, which could prevent outer cells from volume collapse.

6.3.3 The noise regulating factor

The noise factor changes the orientation and position of the cells in the whole surface. Visual comparison between the experimental statistical distribution and the theoretical results show significant increase of the perpendicular orientation to the longest axis of the tissue in the delta regions as noise is increased.

Central regions are comparable with the experimental data, specifically for most cells the orientation is near parallel to the y axis. Moreover, the disordered orientation

and position of cells leads to a more realistic arrangement of the cells in the central part of the tissue. One of the main aims of introducing noise was to gain better agreement with the experimental data by breaking up the double delta regions. The smallest value of noise does not lead to any improvement as there is insufficient influence to change orientation of the other cells but higher values such as 5.0 μm or 10.0 μm orient cells in similar manner as in the ENT.

We conclude that the most reasonable value of n is between 5.0 μm and 10.0 μm, where orientation perpendicular to the long axis occurs in the delta regions. Visual comparison shows a strong agreement between the orientation of cells in central region in the model and the experimental orientations.

6.4 Comparison of histograms

Comparison of histograms is a very difficult task. We can observe regions of space without cells, and places where histograms do not match at all. In conclusion, our comparisons do not show precise information about the degree of matching between model and experiment. On the other hand, scaled histograms allow us to compare them visually.

6.5 Origin of cell orientation

All the experimental tissue samples presented here have delta regions, where cells are perpendicular to the long axis. On the other hand cells in the central region should be parallel to the longest axis of the tissue. Visual comparison between the experimental distribution of cell orientations and simulated systems shows that the simulated cells also have a strongly perpendicular orientation in the delta region.

The part of the Hamiltonian responsible for the description of orientation ($\Delta l(2 - cos^2\alpha_1 - cos^2\alpha_2)$) depends on both cells' angles relative to - α_1 and α_2. When the

angles are close to 90° then this term of the Hamiltonian has a minimum and the value of energy is more likely to be accepted. This feature, shows that cells orient along tension - which is parallel in the middle region of the tissue, but changes orientation near the boundary. When flat, four points or round boundary conditions are applied cells also orient parallel to x axis which is along the tension in the delta regions.

We conclude, that both the fixed positions of cells around the tethers points and the tendency of cells to squeeze generate tension. Moreover, the Hamiltonian has a minimum value when cells orients parallel to the strain.

6.6 Summary

In summary, we would like to conclude that results from our models are similar to the arrangement of cells in real tissue. The arrangement of cells in theoretical models corresponds to the three main regions in the experimental tissue. Therefore, the main goal of the project was achieved, as engineered tissue was simulated and the main interactions can be explained phenomenologically.

On the other hand, both the crossover between regions and the orientation of cells in the delta regions still need some improvement. Therefore conclusions reached in the thesis provide a basis for further investigations. At this stage, the model could help engineers to design new moulds with different tethers. New tether points can potentially decrease the size of the delta regions.

6.7 Further work

The purpose of this section is to draft a plan of the further work essential to continue the research. So far, we developed promising models and obtained knowledge about interactions between cells.

6.7.1 Data comparison

The first step is connected with a comparison of histograms which allows researchers to precisely judge the degree of matching between modelled tissue and ENT for every bin of the histogram. In other words, researchers needs to be able to judge compatibility with the experimental results, in order to check correctness of parameters chosen in the Hamiltonian. The required software has to quickly compare the obtained model with the engineered neural tissue. The program should compare a corresponding range of angles included in the chosen surface in both the modelled tissue and ENT. Then it should map the results to the corresponding area. As a final result we should obtain information which allows us to find the degree of matching for every bin of the histogram.

6.7.2 Annealing schedule

In the project, metropolis algorithm was used to compute the minimum of the energy described by the Hamiltonian. Unfortunately the time needed to fully anneal some of the models was too long. Theoretically, an efficient way to speed up the computation process is to change the annealing schedule. The system of cells at the beginning of the simulation requires significant changes of cell position, yet only slight changes of position and orientation at the end. In the literature a helpful method to speed up the computing process is the fast annealing algorithm (FSA), which is described by Szu and Hartley ref. [78]. The method is a more advanced and faster version of simulated annealing. Attempts to implement FSA were already made, but so far converged results were not obtained.

The basic idea of fast simulated annealing is similar to the traditional simulated annealing (SA) algorithm used here. At the beginning of execution time (FSA) generates more long steps then SA. Similarly to the SA algorithm, temperature decreases during

execution time and allows the algorithm to jump out of local minima. An important difference is the probability distribution which is used to probe the next state of the system, called the Cauchy distribution. The Cauchy distribution is relatively easy and fast to obtain numerically. During the annealing process the range of steps rapidly decreases and the algorithm focuses on searching around the minimum. The method requires a different temperature schedule to control the quantity of long steps. The value of temperature is inversely proportional to the execution time [78, 85].

6.7.3 Parallelisation

Optionally, another speed up of the computation time can be done. Using the CUDA library and properties of the graphic card, it seems possible to run many processes at the same time. Unfortunately, the simulated annealing algorithm is very difficult to parallelise. On the other hand, a system made of many cells could be divided into smaller parts and energy of them computed in parallel.

6.7.4 Model

Additional improvement is connected with the initial system of cells and number of neighbours used during simulation. So far the initial grid of cells had regular distances between cells and let us understand and model basic tissue. The use of an initial system based on a regular triangular matrix extends the number of neighbours to six. The advantage of the triangular grid is an equal initial distance between cells. The analytical computations included in [49] show that Hookean springs on triangle lattice have a simple shear coefficient which may prevent cells from volume collapse.

Artificial neural tissue has three dimensions, so far our models were concerned with 2D tissues. The next step is to model 3D artificial tissue. The obtained results will allow checking of physical interactions described by the Hamiltonian. When the algorithm is

able to predict the orientation and arrangement of cells within 3D engineered tissue, it is possible to achieve the goal of the project. The model should help to design a new mould which will allow cells to create more aligned structures and decrease the size of the delta regions. Experimental groups can try to grow engineered tissue with the new mould. Hopefully the presented scheme of further work will push the boundary of knowledge regarding the engineered neural tissue and lower the cost of experiments.

References

[1] E. Bianconi, A. Piovesan, F. Facchin, A. Beraudi, R. Casadei, F. Frabetti, L. Vitale, M. Chiara Pelleri, S. Tassani, F. Piva, S. Perez-Amodio, P. Strippoli, and S. Canaider. An Estimation of the Number of Cells in the Human Body. *Annals of Human Biology*, 40(6):463–71, 2014.

[2] W. M. Becker, L. J. Kleinsmith, J. Hardin, and G. P. Bertoni. *World of the Cell, The: International Edition, 7/E.* 2009.

[3] Apligraf. http://www.apligraf.com/.

[4] Robert A. Brown and James B. Phillips. Cell Responses to Biomimetic Protein Scaffolds Used in Tissue Repair and Engineering. volume 262 of *International Review of Cytology*, pages 75 – 150. Academic Press, 2007.

[5] A. Famulari, P. De Simone, R. Verzaro, G. Iaria, F. Polisetti, M. Rascente, and A. Aureli. Artificial Organs as a Bridge to Transplantation. *Artificial Cells, Blood Substitutes, and Biotechnology*, 31(2):163–168, 2003.

[6] H. Ben-Bassat. Performance and Safety of Skin Allografts. *Clinics in Dermatology*, 23(4):365–375, 2005.

[7] E. East, D. B. de Oliveira, J. P. Golding, and J. B. Phillips. Alignment of Astrocytes Increases Neuronal Growth in Three-dimensional Collagen Gels and is Maintained Following Plastic Compression to Form a Spinal Cord Repair Conduit. *Tissue Engineering Part A*, 16(10):3173–3184, 2010.

[8] A. Herman. The history of skin grafts. *Physical Review Letters*, 1(3):298–301, 2002.

[9] D. Sommerfeldt and C. Rubin. Biology of Bone and How it Orchestrates the form and Function of the Skeleton. *European Spine Journal*, 10(SUPPL. 2):86–95, 2001.

[10] A. J. Salgado, O. P. Coutinho, and R. L. Reis. Bone Tissue Engineering: State of the Art and Future Trends. *Macromolecular Bioscience*, 4(8):743–765, 2004.

[11] U. S. Schwarz and S. A Safran. Physics of Adherent Cells. *Reviews of Modern Physics*, 85(3):1327, 2013.

[12] R. V. Stirling J. G. Pernavelas, C. D. Stern. *The Making of Nervous System*. Oxford University Press, New York, 1988.

[13] G. H. Altman, F. Diaz, C. Jakuba, T. Calabro, R. L. Horan, J. Chen, H. Lu, J. Richmond, D. L. Kaplan. Silk-based Biomaterials. *Biomaterials*, 24(3):401–416, 2003.

[14] J. M. Gosline, P. A. Guerette, C. S. Ortlepp, and K. N. Savage. The Mechanical Design of Spider Silks: from Fibroin Sequence to Mechanical Function. *The Journal of Experimental Biology*, 202(Pt 23):3295–3303, 1999.

[15] H. Shin, S. Jo, and A. G. Mikos. Biomimetic Materials for Tissue Engineering. *Biomaterials*, 24(2):4353–4364, 2003.

[16] T. C. Holmes, S. de Lacalle, X. Su, G. Liu, A. Rich, S. Zhang. Extensive Neurite Outgrowth and Active Synapse Formation on Self-assembling Peptide Scaffolds. *Proceedings of the National Academy of Sciences of the United States of America*, 97(12):6728–6733, 2000.

[17] J. Kisiday, M. Jin, B. Kurz, H. Hung, C. Semino, S. Zhang, and J. Grodzinsky. Self-assembling Peptide Hydrogel Fosters Chondrocyte Extracellular Matrix Production and Cell Division: Implications for Cartilage Tissue Repair. *Proceedings*

of the National Academy of Sciences of the United States of America, 99(15):9996–10001, 2002.

[18] L. G. Griffith and M. A. Swartz. Capturing Complex 3D Tissue Physiology in Vitro. *Nature Reviews. Molecular Cell Biology*, 7(3):211–224, 2006.

[19] J. J. Tomasek, G. Gabbiani, B. Hinz, Ch. Chaponnier, and R. A. Brown. Myofibroblasts and Mechano-regulation of Connective Tissue Remodelling. *Nature Reviews. Molecular Cell Biology*, 3(5):349–363, 2002.

[20] J. A. T. Dow, P. Clark, P. Connolly, A. S. G. Curtis, and C. D. W. Wilkinson. Novel Methods for the Guidance and Monitoring of Single Cells and Simple Networks in Culture. *Journal of Cell Science. Supplement*, 8:55–79, 1987.

[21] I.B. Bischofs. *Elastic Interactions of Cellular Force Patterns*. PhD thesis, University of Postdam, 2004.

[22] B. Cortese, G. Gigli, and M. Riehle. Mechanical Gradient Cues for Guided Cell Motility and Control of Cell Behavior on Uniform Substrates. *Advanced Functional Materials*, 19(18):2961–2968, 2009.

[23] A. Sørensen, T. Alekseeva, K. Katechia, M. Robertson, M. O. Riehle, and S. C. Barnett. Long-term Neurite Orientation on Astrocyte Monolayers Aligned by Microtopography. *Biomaterials*, 28(36):5498–5508, 2007.

[24] I. B. Bischofs, S. A. Safran, and U. S. Schwarz. Elastic Interactions of Active Cells With Soft Materials. *Physical Review E*, 69:021911, 2004.

[25] R. A. Brown, K. D. Smith, and D. Angus McGrouther. Strategies for Cell Engineering in Tissue Repair. *Wound repair and regeneration: official publication of the Wound Healing Society [and] the European Tissue Repair Society*, 5(3):212–221, 1997.

[26] Lin, F. and Baldessari, F. and Gyenge, Ch. C. and Sato, T. and Chambers, R. D. and Santiago, J. G. and Butcher, E. C. Lymphocyte Electrotaxis In Vitro and In Vivo. *The Journal of Immunology*, 181(4):2465–2471, 2008.

[27] B. Cortese, I. E. Palama, S. D'Amone, and G. Gigli. Influence of electrotaxis on cell behaviour. *Integr. Biol.*, 6:817–830, 2014.

[28] N. Dubey, P. C. Letourneau, and R. T. Tranquillo. Guided Neurite Elongation and Schwann Cell Invasion into Magnetically Aligned Collagen in Simulated Peripheral Nerve Regeneration. *Experimental Neurology*, 158(2):338–350, 1999.

[29] D.B. Dusenbery. *Living at Micro Scale: The Unexpected Physics of Being Small*. Harvard University Press, 2009.

[30] J. B. McCarthy, S. L. Palm, and L. T. Furcht. Migration by Haptotaxis of a Schwann Cell Tumor Line to the Basement Membrane Glycoprotein Laminin. *The Journal of Cell Biology*, 97(3):772–777, 1983.

[31] W. J. Kwang. *International Review Of Cytology: A Survey of Cell Biology*, volume 262. Academic Press, 2007.

[32] W. K. Purves, C. Heller, G. Orians, D. E. Sadava. *Life, the Science of Biology*. Sinauer Associates, Sunderland, 6th edition, 2001.

[33] Protein Atlas. `http://www.proteinatlas.org/humancell/intermediate+filaments`. [Online; accessed August-2015].

[34] British Society for Cell Biology. `http://bscb.org/learning-resources/softcell-e-learning/cytoskeleton-the-movers-and-shapers-in-the-cell/`. [Online; accessed August-2015].

[35] N. Orme R. Phillips, J. Kondev, J. Theriot. *Physical Biology of the Cell.* Number 3. Garland Science, 1st edition, 2008.

[36] J. Howard. *Mechanics of Motor Proteins and the Cytoskeleton.* Sinauer Associates, 2001.

[37] University Of Illinois At Urbana-Champaign. `https://news.illinois.edu/blog/view/6367/207521`. [Online; accessed August-2015].

[38] Ha. Wolfenson, Y. I. Henis, B. Geiger, and A. D. Bershadsky. The Heel and Toe of the Cell's Foot: a Multifaceted Approach for Understanding the Structure and Dynamics of Focal Adhesions. *Cell Motility and the Cytoskeleton*, 66(11):1017–1029, 2009.

[39] University Of Reading. `http://www.reading.ac.uk/nitricoxide/intro/migration/adhesion.htm`. [Online; accessed August-2015].

[40] B. Alberts, A. Johnson, J. Lewis. *Molecular Biology of the Cell. 4th edition.* New York: Garland Science, 2002.

[41] G. A. Di Lullo, S. M. Sweeney, J. Korkko, L. Ala-Kokko, and J. D. San Antonio. Mapping the Ligand-binding Sites and Disease-associated Mutations on the Most Abundant Protein in the Human, Type I Collagen. *Journal of Biological Chemistry*, 277(6):4223–4231, 2002.

[42] Sigma-Aldrich. `http://www.sigmaaldrich.com/life-science/biochemicals/biochemical-products.html?TablePage=21735546`. [Online; accessed August-2015].

[43] F. Gonçalves, R. Bentini, M. C. Burrows, A. C. O. Carreira, P. M. Kossugue, M. C. Sogayar, and L. H. Catalani. Hybrid Membranes of PLLA/Collagen for

Bone Tissue Engineering: A Comparative Study of Scaffold Production Techniques for Optimal Mechanical Properties and Osteoinduction Ability. *Materials (1996-1944)*, 8(2):408–423, 2015.

[44] A. Vernadakis S. Fedoroff. *Astrocytes. Development, Morphology and Regional Specialization of Astrocytes*, volume 1. Academic Press, inc. Harcourt Brace Jovanovich Publishers, 1986.

[45] A. Alovskaya, T. Alekseeva, J. B. Phillips, V. King, and R. Brown. Fibronectin, Collagen, Fibrin-Components of Extracellular Matrix for Nerve regeneration. *Topics in Tissue Engineering*, 3:1–27, 2007.

[46] H Gray. *Gray's Anatomy: The Anatomical Basis of Clinical Practice*. Elsevier Churchill Livingstone, 39th edition, 2005.

[47] C. A. Heath and G. E. Rutkowski. The Development of Bioartificial Nerve Grafts for Peripheral-nerve Regeneration. *Trends in Biotechnology*, 16(4):163 – 168, 1998.

[48] O'Rourke, C. and Drake, R. A. and Cameron, G. W. and Loughlin, J. A. and Phillips, J. B. Optimising Contraction and Alignment of Cellular Collagen Hydrogels to Achieve Reliable and Consistent Engineered Anisotropic Tissue. *Journal of Biomaterials Applications*, 0(0):1–9, 2015.

[49] Boal, D. H. . *Mechanics of the Cell*. Cambridge University Press, Canada, 2012.

[50] O. Lieleg, M. M. Claessens, Y. Luan, and A. R. Bausch. Transient Binding and Dissipation in Cross-Linked Actin Networks. *Physical Review Letters*, 101(10):108101, 2008.

[51] L. D. Landau, E. M. Lifshitz, J. B. Sykes, W. H. Reid, and E. H. Dill. *Theory of Elasticity: Course of Theoretical Physics*, volume 7. Pergamon Press, 1960.

[52] F. Tessier, D. H. Boal, and D. E. Discher. Networks with Fourfold Connectivity in Two Dimensions. *Phys. Rev. E*, 67:011903, Jan 2003.

[53] R. Bar-Ziv, T. Tlusty, E. Moses, S. Safran, and A. Bershadsky. Pearling in Cells: a Clue To Understanding Cell Shape. *Proceedings of the National Academy of Sciences of the United States of America*, 96(18):10140–10145, 1999.

[54] P. Guthardt Torres, I. B. Bischofs, and U. S. Schwarz. Contractile Network Models for Adherent Cells. *Phys. Rev. E*, 85:011913, Jan 2012.

[55] R. De, A. Zemel, and S. A. Safran. Dynamics of Cell Orientation. *Nature Physics*, 3(9):655–659, 2007.

[56] I. B. Bischofs and U. S. Schwarz. Effect of Poisson Ratio on Cellular Structure Formation. *Physical Review Letters*, 95:068102, 2005.

[57] J. D. Eshelby. The Determination of the Elastic Field of an Ellipsoidal Inclusion, and Related Problems. *Proceedings of the Royal Society A: Mathematical, Physical and Engineering Sciences*, 241(1226):376–396, 1957.

[58] J. D. Eshelby. The Elastic Field Outside an Ellipsoidal Inclusion. *Proceedings of the Royal Society A: Mathematical, Physical and Engineering Sciences*, 252(1271):561–569, 1959.

[59] M. Eastwood, V. C. Mudera, D. A. McGrouther, and R. A. Brown. Effect of Precise Mechanical Loading on Fibroblast Populated Collagen Lattices: Morphological Changes. *Cell Motility and the Cytoskeleton*, 40(1):13–21, 1998.

[60] A. Collinsworth, C. Torgan, S. Nagda, R. Rajalingam, W. Kraus, and G. Truskey. Orientation and Length of Mammalian Skeletal Myocytes in Response to a Unidirectional Stretch. *Cell and Tissue Research*, 302(2):243–251, 2000.

[61] S. Jungbauer, H. Gao, J. P. Spatz, and R. Kemkemer. Two Characteristic Regimes in Frequency-dependent Dynamic Reorientation of Fibroblasts on Cyclically Stretched Substrates. *Biophysical Journal*, 95(7):3470–3478, 2008.

[62] K. Kurpinski, J. Chu, C. Hashi, and S. Li. Anisotropic Mechanosensing by Mesenchymal Stem Cells. *Proceedings of the National Academy of Sciences of the United States of America*, 103(44):16095–100, 2006.

[63] U. Faust, N. Hampe, W. Rubner, N. Kirchgeßner, S. Safran, B. Hoffmann, and R. Merkel. Cyclic Stress at mHz Frequencies Aligns Fibroblasts in Direction of Zero Strain. *PLoS ONE*, 6(12):e28963, 2011.

[64] V. S. Deshpande. Analysis and Interpretation of Stress Fiber Organization in Cells Subject to Cyclic Stretch. *Journal of Biomechanical Engineering*, 130(3):031009, 2008.

[65] P. Pirentis and K. Lazopoulos. On Stress Fibre Reorientation under Plane Substrate Stretching. *Archive of Applied Mechanics*, 79(3):263–277, 2009.

[66] J. Wang, P. Goldschmidt-Clermont, J. Wille, and F. Yin. Specificity of Endothelial Cell Reorientation in Response to Cyclic Mechanical Stretching. *Journal of Biomechanics*, 34(12):1563–1572, 2001.

[67] M. Eastwood, V.C. Mudera, D.A. Mcgrouther, and R.A. Brown. Effect of Precise Mechanical Loading on Fibroblast Populated Collagen Lattices: Morphological Changes. *Cell Motility and the Cytoskeleton*, 40(1):13–21, 1998.

[68] R. De and S. A. Safran. Dynamical Theory of Active Cellular Response to External Stress. *Physical Review E - Statistical, Nonlinear, and Soft Matter Physics*, 78(3), 2008.

[69] S. Safran and R. De. Nonlinear Dynamics of Cell Orientation. *Physical Review E - Statistical, Nonlinear, and Soft Matter Physics*, 80(6):4–7, 2009.

[70] I. B. Bischofs and U. S. Schwarz. Collective Effects in Cellular Structure Formation Mediated by Compliant Environments: A Monte Carlo Study. *Acta Biomaterialia*, 2(3):253–265, 2006.

[71] U. S. Schwarz and S. A. Safran. Elastic Interactions of Cells. *Phys. Rev. Lett.*, 88:048102, 2002.

[72] I. B. Bischofs and U. S. Schwarz. Cell Organization in Soft Media due to Active Mechanosensing. *Proceedings of the National Academy of Sciences of the United States of America*, 100(16):9274–9279, 2003.

[73] A. Zemel, I. B. Bischofs, and S. A. Safran. Active Elasticity of Gels with Contractile Cells. *Physical Review Letters*, 97:128103, 2006.

[74] S. Kirkpatrick, C. D. Gelatt, M. P. Vecchi, et al. Optimization by Simulated Annealing. *Science*, 220(4598):671–680, 1983.

[75] D. Bertsimas and J. Tsitsiklis. Simulated annealing. *Statistical Science*, 8(1):10–15, 1993.

[76] W. Press, S. Teukolsky, W. Vetterling, and B. Flannery. *Numerical Recipes in C The Art of Scientific Computing*. Cambridge Press, 2nd edition, 1992.

[77] I. Beichl and F. Sullivan. The metropolis algorithm. *Computing in Science & Engineering*, 2(1):65–69, 2000.

[78] H. Szu and R. Hartley. Fast Simulated Annealing. *Physics Letters A*, 122(3-4):157–162, 1987.

[79] D. Henderson, S. H. Jacobson, and A. W. Johnson. The Theory and Practice of Simulated Annealing. *Handbook of Metaheuristics SE - 10*, 57:287–319, 2003.

[80] G. Dueck and T. Scheurer. Threshold Accepting: A General Purpose Optimization Algorithm. *Journal of Computational Physics*, 90:161–175, 1990.

[81] P. Moscato and J. F. Fontanari. Convergence and Finite-time Behavior of Simulated Annealing. *Advances in Applied Probability*, 18:747–771, 1990.

[82] T. Hu, A. Kahng, and C. Tsao. Old Bachelor Acceptance: A New Class of Non-Monotone Treshold Accepting Methods. *Journal on Computing*, 7, 1995.

[83] I. Althöfer and K. Koschnick. On the Convergence of "Threshold Accepting". *Applied Mathematics and Optimization*, 24:183–195, 1991.

[84] D. E. Goldberg. *Genetic Algorithms in Search, Optimization and Machine Learning*. Addison-Wesley Longman Publishing, Boston, 1st edition, 1989.

[85] V.B. Nascimento, V.E. de Carvalho, C.M.C. de Castilho, B.V. Costa, and E.A. Soares. The Fast Simulated Annealing Algorithm Applied to the Search Problem in LEED. *Surface Science*, 487(1-3):15–27, 2001.